2006-10-16

Fabrication of Hollow Optical Waveguides on Planar Substrates

John P. Barber
Brigham Young University - Provo

BYU ScholarsArchive Citation

Barber, John P., "Fabrication of Hollow Optical Waveguides on Planar Substrates" (2006). *Theses and Dissertations*. 799.
https://scholarsarchive.byu.edu/etd/799

FABRICATION OF HOLLOW OPTICAL WAVEGUIDES ON PLANAR SUBSTRATES

by

John P. Barber

A dissertation submitted to the faculty of

Brigham Young University

in partial fulfillment of the requirements for the degree of

Doctor of Philosophy

Department of Electrical and Computer Engineering

Brigham Young University

December 2006

BRIGHAM YOUNG UNIVERSITY

GRADUATE COMMITTEE APPROVAL

of a dissertation submitted by

John P. Barber

This dissertation has been read by each member of the following graduate committee and by majority vote has been found to be satisfactory.

Date	Aaron R. Hawkins, Chair
Date	Milton L. Lee
Date	Gregory P. Nordin
Date	Stephen M. Schultz
Date	Richard. H. Selfridge

BRIGHAM YOUNG UNIVERSITY

As chair of the candidate's graduate committee, I have read the dissertation of John P. Barber in its final form and have found that (1) its format, citations, and bibliographical style are consistent and acceptable and fulfill university and department style requirements; (2) its illustrative materials including figures, tables, and charts are in place; and (3) the final manuscript is satisfactory to the graduate committee and is ready for submission to the university library.

Date	Aaron R. Hawkins Chair, Graduate Committee

Accepted for the Department

Michael J. Wirthlin
Graduate Coordinator

Accepted for the College

Alan R. Parkinson
Dean, Ira A. Fulton College of Engineering and Technology

ABSTRACT

FABRICATION OF HOLLOW OPTICAL WAVEGUIDES ON PLANAR SUBSTRATES

John P. Barber
Department of Electrical and Computer Engineering
Doctor of Philosophy

This dissertation presents the fabrication of hollow optical waveguides integrated on planar substrates. Similar in principle to Bragg waveguides and other photonic crystal waveguides, the antiresonant reflecting optical waveguide (ARROW) is used to guide light in hollow cores filled with liquids or gases. Waveguides with liquid or gas cores are an important new building block for integrated optical sensors.

The fabrication method developed for hollow ARROW waveguides makes use of standard microfabrication processes and materials. Dielectric layers are deposited on a silicon wafer using plasma-enhanced chemical vapor deposition (PECVD) to form the bottom layers of the ARROW waveguide. A sacrificial core material is then deposited and patterned. Core materials used include aluminum, SU-8 and reflowed photoresist,

each resulting in a different core geometry. Additional dielectric layers are then deposited, forming the top and sides of the waveguide. The sacrificial core is then removed in an acid solution, resulting in a hollow ARROW waveguide.

Experiments investigating the mechanical strength of the hollow waveguides and the etching characteristics of the sacrificial core suggest design rules for the different core types. Integration of solid-core waveguides is accomplished by etching a ridge into the top dielectric layer of the ARROW structure. Improved optical performance can be obtained by forming the waveguides on top of a raised pedestal on the silicon substrate.

Loss measurements on hollow ARROW waveguides fabricated in this manner gave loss coefficients of 0.26 cm^{-1} for liquid-core waveguides and 2.6 cm^{-1} for air-core waveguides. Fluorescence measurements in liquid-core ARROW waveguides have achieved single-molecule detection sensitivity. Integrated optical filters based on ARROW waveguides were fabricated, and preliminary results of a capillary electrophoresis separation device using a hollow ARROW indicate the feasibility of such devices for future investigation.

ACKNOWLEDGMENTS

This dissertation and the research behind it would not be possible without the support of many people. My adviser, Dr. Aaron Hawkins, has provided needed guidance throughout the duration of my research. The collaboration with Dongliang Yin and Dr. Holger Schmidt at UCSC has been very beneficial due to their hard work on this project. Additional support and funding was provided by Dr. David Deamer at UCSC and Dr. Milton Lee at BYU. Dr. Richard Selfridge provided my first research opportunity, and the experience I gained during that time has been invaluable to my later work.

Many fellow students have made invaluable contributions to the research presented here. Don Conkey, Evan Lunt, Matt Smith, J. Ryan Lee, Ghassan Sanber, Tao Sheng, Matt Holmes, Bridget Peeni, John Edwards, Neal Hubbard and Craig Christianson all have helped in many ways, and I am indebted to them for their efforts. Elizabeth Despain, Zack George and Jeffrey Maas provided excellent SEM imagery, as can be seen throughout this dissertation.

TABLE OF CONTENTS

LIST OF TABLES

LIST OF FIGURES

1 Introduction

1.1 Integrated Optical Sensors

Much attention has been focused on the field of integrated optics in recent years. Integrated optics is the combination of multiple optical components on a common substrate in miniaturized form. Common applications of integrated optics include optical communications systems [1], optical integrated circuits for optical computing [2], and optical sensors. Integration of both functional elements, such as lasers, photodetectors and modulators, and interconnections between elements in the form of waveguides, is critical to the success of integrated optics as a whole.

Optical sensing is a broad field encompassing many applications. In biology, chemistry, and medicine, optical sensors are used to examine processes at very small scales, down to the molecular level. Common optical sensing mechanisms include fluorescence detection and Raman spectroscopy [3]. Fluorescence sensing is the most sensitive method for detecting the presence of small quantities of biological molecules, and is capable of single molecule detection sensitivity [4]. This method has been used for the study of such phenomena as DNA interactions [5], [6], protein dynamics [7]-[9], and ribozyme kinetics [10]. At present, such studies are performed with diffraction-limited optics in bulky setups, using techniques such as epifluorescence [11], confocal microscopy [11] and evanescent field sensors [12]. A typical experimental setup for such measurements is shown in Figure 1.1. Such setups are large and cannot be scaled to arrays of sensors as the measurement location is limited to a single focal point.

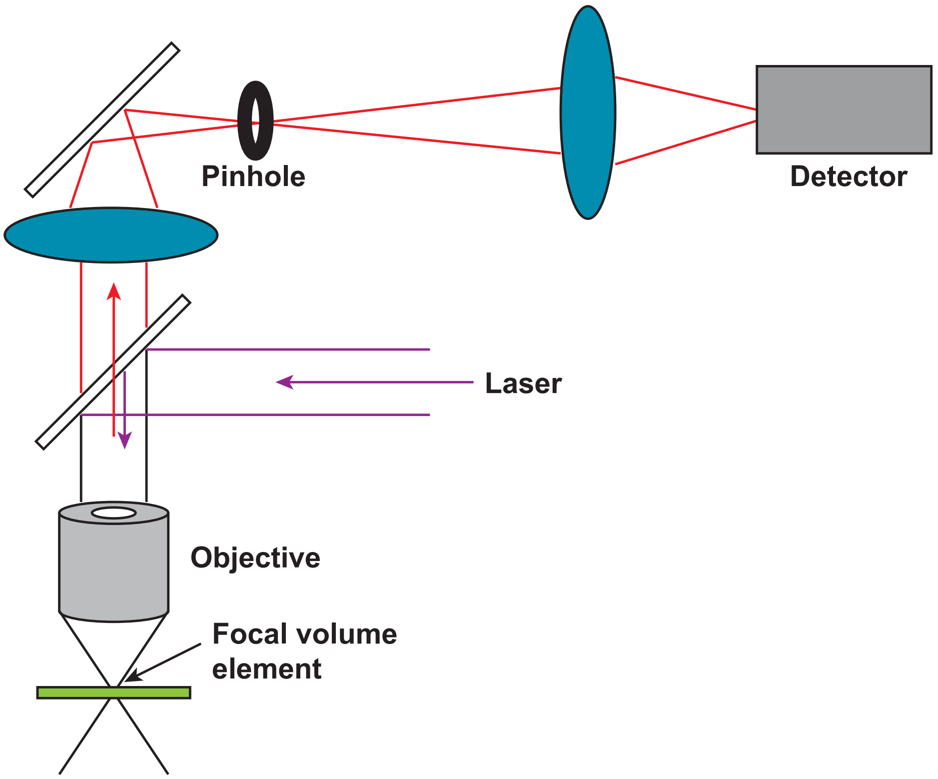

Figure 1.1 – Diagram of a typical conventional fluorescence sensing platform.

By making use of an integrated optical platform, the bulky setup shown above could be eliminated. Such a device would be small and readily scalable to perform multiple measurements using arrays of sensors. Additionally, an integrated device fabricated using conventional silicon microfabrication technology would have low cost and a straightforward fabrication process.

Unfortunately, conventional integrated optical components cannot provide waveguiding in the low-index materials used in such sensing applications. Integrated devices have been developed which combine microfluidic systems with optical sensing [13]-[16]. However, these devices do not guide light in the liquid channels. A waveguiding technology for non-solid cores would create much flexibility in the application of optical sensing to the types of measurements described above. Additional applications of such waveguides include integrated dye lasers [17] and quantum optics such as electromagnetically-induced transparency [18].

1.2 Integrated Optical Waveguides with Hollow Cores

We have developed a robust method for fabrication of hollow optical waveguides suitable for integrated optical sensing. These devices are known as antiresonant reflecting optical waveguides (ARROW), and are capable of guiding light in low-index materials such as gases and liquids. With the ability to guide light in such materials, new integrated sensing devices can be developed. Figure 1.2 shows a possible sensor platform utilizing a hollow waveguide for fluid flow and optical collection of fluorescence from within the fluid. This represents one possible application of the waveguides we have developed, while many other potential applications have yet to be explored

This dissertation describes the fabrication of hollow ARROW waveguides. Chapter 2 presents the theory of the ARROW waveguide, including a comparison to other waveguiding methods. Numerical simulations of 1-d (slab) ARROW waveguides are presented. Chapter 3 gives a general overview of the hollow ARROW fabrication process including descriptions of the sub-processes involved. As will be discussed, our method utilizes standard silicon microfabrication procedures and materials, which is a key advantage over other fabrication methods.

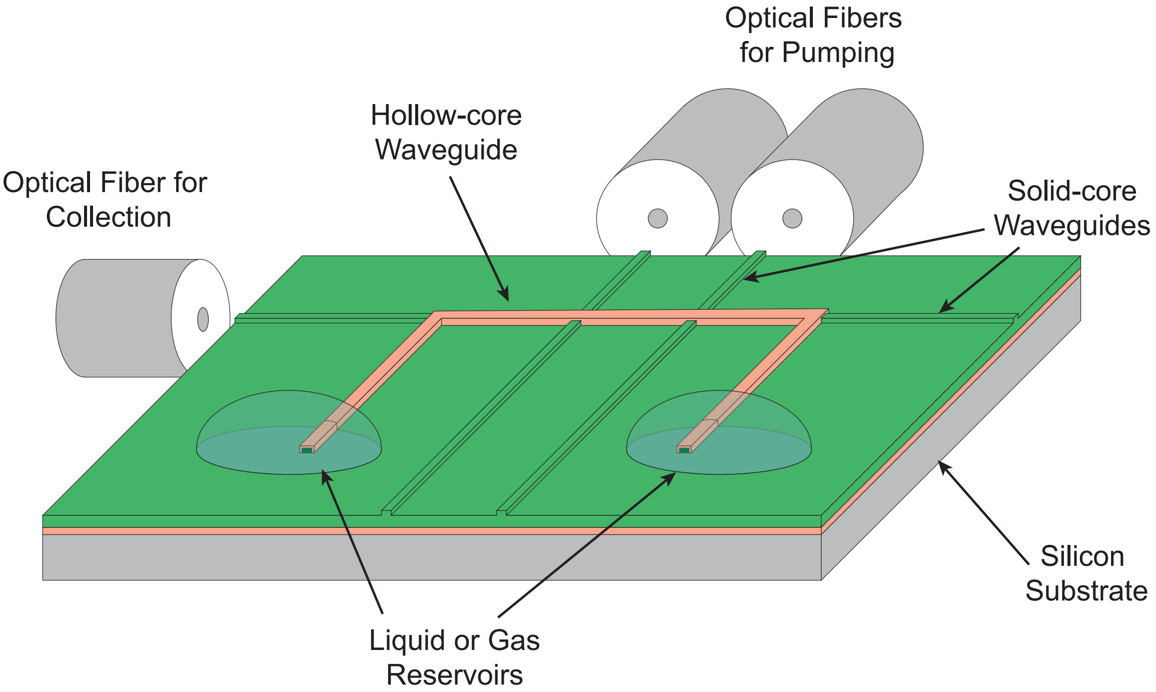

Figure 1.2 - Integrated optical sensing platform based on a hollow ARROW waveguide.

Chapters 4 through 7 discuss the various types of waveguides that can be fabricated using our method. Experiments performed to determine the mechanical properties of the waveguides are described and optical measurements given. As shown in Chapter 7, advanced structures such as solid-core waveguides for optical interfacing can easily be integrated with the hollow-core devices. Some applications of integrated hollow ARROW waveguides including are discussed in Chapter 8, including fluorescence sensors, optical filters and a capillary electrophoresis device.

1.3 Contributions

The research discussed in this dissertation is the product of collaboration with researchers at the University of California at Santa Cruz (UCSC). Development of the fabrication process for hollow ARROW waveguides was performed by me in the BYU Integrated Microfabrication Laboratory (IML), as was the production of the waveguides used in our research. The optical design and testing of the device was performed at UCSC. This dissertation focuses on the fabrication process, but includes significant results regarding the design and performance of the waveguides.

The research presented here represents a significant contribution to the field of integrated optics. The low cost and relative simplicity of the fabrication process will enable many applications of hollow ARROW waveguides. Some of these, such as fluorescence studies of small numbers of molecules, have already been investigated. To date, parts of our research have been published in 13 peer-reviewed journal articles [18]-[30] and 16 conference presentations [31]-[46]. This is an important addition to the general body of knowledge, and the potential of the hollow ARROW waveguide has yet to be fully explored.

2 Optical Waveguiding in Low-Index Materials

2.1 Introduction

This chapter describes the theory of the antiresonant reflecting optical waveguide (ARROW). First, an overview of conventional waveguides is given, along with descriptions of materials suitable for guiding in materials with low refractive indices, such as gases and liquids. Alternative methods of waveguiding based on photonic crystals have recently garnered much interest. Different types of photonic crystals including holey fibers and Bragg waveguides are discussed. The ARROW waveguide is very similar to Bragg waveguides, and is the type of waveguide used in the research presented here. The theory of the ARROW waveguide is described, and results of numerical simulations of ARROW waveguides are given.

2.2 Index Guiding

Conventional waveguides utilize a high-index core surrounded by a lower index cladding, as illustrated in Figure 2.1. The most common example of conventional waveguides is the optical fiber, used extensively in the telecommunications field. Geometric optics can be used to explain the operation of a conventional waveguide by the phenomenon of total internal reflection.

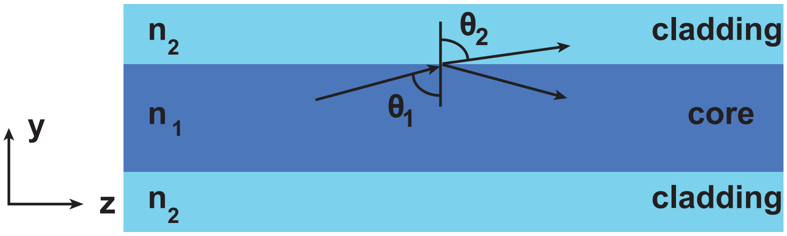

Figure 2.1 - Index guiding in a slab waveguide, with propagation in the +z direction. For optical confinement in the waveguide core, $n_1 > n_2$.

A light ray in the core of the waveguide propagating in the +*z* direction is used to illustrate index guiding. Upon reaching the interface between the core and cladding, the ray will be partially reflected and partially transmitted. Snell's law of refraction describes the relationship between the incident and transmitted wave:

$$n_1 \sin\theta_1 = n_2 \sin\theta_2 , \tag{2.1}$$

where n_1 and n_2 are the refractive indices of the materials, and θ_1 and θ_2 are the angles with respect to the normal to the interface. Total internal reflection takes place when the incident angle θ_1 exceeds a value known as the critical angle, θ_c. This angle is given by:

$$\theta_1 > \sin^{-1}\left(\frac{n_2}{n_1}\right) = \theta_c . \tag{2.2}$$

Above the critical angle, sin θ_2 becomes imaginary, so the ray is completely reflected at the interface and will propagate in the core without loss.

Waveguiding by total internal reflection requires that $n_1 > n_2$. If the cladding index were greater than the core, total internal reflection would not occur, and the light would quickly leak into the cladding and dissipate. This requirement is a serious limitation for the construction of waveguides designed for use with low-index materials such as water (n = 1.33) or other liquids. Additionally, index guiding is impossible in air (n = 1) because no materials exist with a refractive index less than 1. Thus, other solutions must be found to achieve waveguiding in air or other gases.

A few materials suitable for index guiding with water cores exist. One, an amorphous fluorinated polymer known by the brand name Teflon AF®, has an index of >1.29 [47]. This material has been used to fabricate hollow capillary tubes with core diameters on the order of 100 μm, capable of guiding light in aqueous solutions. These devices have been used for a variety of liquid-based optical sensing applications including fluorescence [48], Raman spectroscopy [49], adsorption detection [50], and chemiluminescence [51].

Integration of Teflon AF® onto planar silicon substrates was reported in [52], but remains challenging due to poor adhesion and the necessity of spin-coating and wafer bonding to form hollow waveguides. The waveguide dimensions reported were on the order of 100 μm square, so applications requiring very small sample sizes cannot be realized. Additionally, many biosensing applications require functionalization of the core-cladding interface, which is difficult due to the extreme inertness of Teflon-based materials.

In addition to Teflon AF®, nanoporous dielectric-based materials can have a refractive index less than 1.33 due to the incorporation of large amounts of air into the material. A slab waveguide using such a material was reported in [53], with a core width of 50 µm. Fabrication of a 2-d waveguide using the reported method would be difficult, and the behavior of the cladding material in contact with water was difficult to control. Clearly, significant challenges exist for fabrication of planar hollow waveguides using either Teflon AF® or nanoporous dielectrics.

2.3 Photonic Crystals

2.3.1 Introduction

An alternative method to index guiding known as the photonic crystal has garnered much interest in recent years. A photonic crystal is a periodic lattice of dielectric materials. If the lattice satisfies certain conditions, a photonic band gap will occur, meaning that light within a range of frequencies cannot propagate in the crystal [54]. This is analogous to the propagation of electrons in a semiconductor, where the electrons are restricted to certain energy bands, and forbidden from existing in others. Because of the photonic band gap, photonic crystals can be used to guide light in low-index materials, even when surrounded by higher-index claddings.

In general, photonic crystals can be one-, two-, or three-dimensional. A 1-d photonic crystal consists of alternating layers of dielectric materials, with periodicity in a single direction. Two- and 3-d photonic crystals have periodicity in multiple dimensions. The optical properties of such a structure depend on the refractive indices of the dielectric materials as well as the period of the crystal.

2.3.2 Bragg Waveguides

A one-dimensional photonic crystal consists of a periodic stack of dielectric films. Such an arrangement is known as a Bragg reflector. The reflectance is a function of the layer thicknesses, the refractive index of the materials, and the angle of incidence. High reflectance occurs with a large contrast in the refractive index of the layers. Additional layer pairs increase the reflectance, as does increasing the angle of incidence.

Light guiding in a low-index material using Bragg reflectors to contain the fields was first proposed in [55] and [56], and fabrication of such waveguides reported in [57]. In a Bragg waveguide, the fields are not completely contained by a finite layer stack, so guided modes are said to be leaky. The loss of a particular Bragg waveguide will depend on the reflectivity of the cladding layers. The largest reflection occurs for a given wavelength when the reflected light from each layer is in phase. This occurs when the layer thicknesses meet the following criteria:

$$d_h = \frac{(2m+1)\lambda_0}{4n_h}\left(1-\frac{n_l^2}{n_h^2}\cos^2\theta\right)^{-1/2} \text{ and} \tag{2.3}$$

$$d_l = \frac{(2m+1)\lambda_0}{4n_l}\frac{1}{\sin\theta}, \tag{2.4}$$

where m is an integer, θ is the grazing angle of the light, and n_l and n_h are the indices of refraction of the low- and high-index materials, respectively [58].

With careful design and a high refractive index contrast between layers, Bragg reflectors can be designed to have total reflection at all angles and polarizations for a band of wavelengths [59]. Hollow fiber waveguides with these characteristics known as omniguides have been demonstrated using alternating layers of polystyrene and tellurium to achieve a high index contrast [60]. Integration of these materials with standard silicon microfabrication processes would be difficult, however.

2.3.3 Two-dimensional Photonic Crystals

Two-dimensional photonic crystals are formed by creating a lattice of dielectric materials with periodicity in two directions. Two common forms of 2-d photonic crystals are planar waveguides fabricated by etching holes or posts into a dielectric material and holey fibers [61]. These types of waveguide are illustrated in Figure 2.2. Two-dimensional photonic crystal waveguides are capable of guiding light in low index materials, and have the ability to form low-loss bends with extremely small radii [62], [63]. Holey fibers have recently been used to demonstrate slow light and electromagnetically-induced transparency in acetylene gas [64].

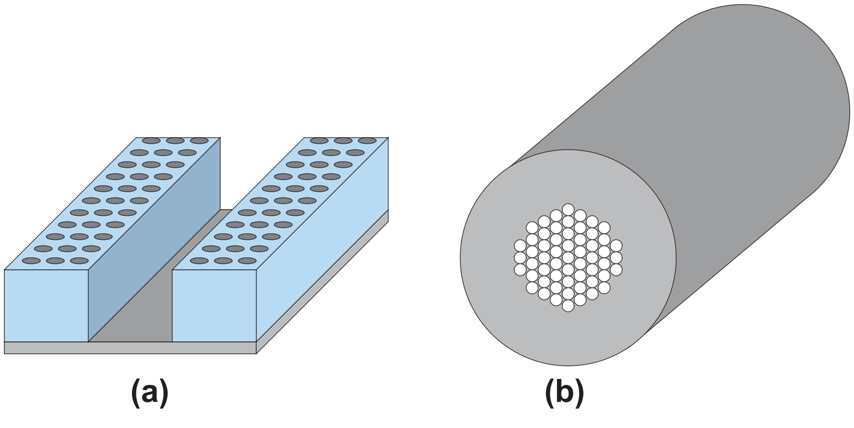

Figure 2.2 - Photonic crystal waveguides. (a) Two-dimensional planar photonic crystal waveguide consisting of periodic holes in a dielectric cladding material. (b) Holey fiber cross-section.

2.4 ARROW Waveguides

2.4.1 Introduction

The antiresonant reflecting optical waveguide (ARROW) was first proposed in [65]. The original ARROW design consisted of a silicon dioxide core with a layer of polycrystalline silicon and a layer of silicon dioxide as cladding materials. Confinement on top of the ARROW was due to index guiding at the oxide/air interface. However, the ARROW concept is easily extended to multiple dielectric layers for improved loss characteristics [66]. The dielectric layers act as Fabry-Perot cavities which exhibit very high reflectivity when operating at antiresonance. ARROW waveguides with solid cores have been used in lasers [67], [68] and integrated optics [69], [70]. Hollow ARROW waveguides were first proposed in [71] and fabrication of waveguides with a core size of 150 μm × 150 μm was reported in [72]. The object of the research described here was to create integrated hollow ARROW waveguides on planar substrates with core geometries on the order of 10 μm.

An illustration of an ARROW waveguide is shown in Figure 2.3. It consists of a core with thickness d_c and refractive index n_c, surrounded by j dielectric layers with thicknesses d_j and refractive indices n_j. Using the assumption that the glancing angle of the propagating mode is:

$$\sin\theta = \lambda / 2 n_c d_c \, , \tag{2.5}$$

the thickness of the j^{th} layer is found to be:

$$t_j = \frac{\lambda}{4n_j}(2M+1)\left(1-\frac{n_c^2}{n_j^2}+\frac{\lambda^2}{4n_j^2 d_c^2}\right)^{-1/2} \tag{2.6}$$

where M is an integer. For cases where the difference between core and cladding index is relatively large, (2.6) simplifies to

$$t_j \approx \frac{\lambda}{4}(2M+1)\left(n_j^2 - n_c^2\right)^{-1/2}. \tag{2.7}$$

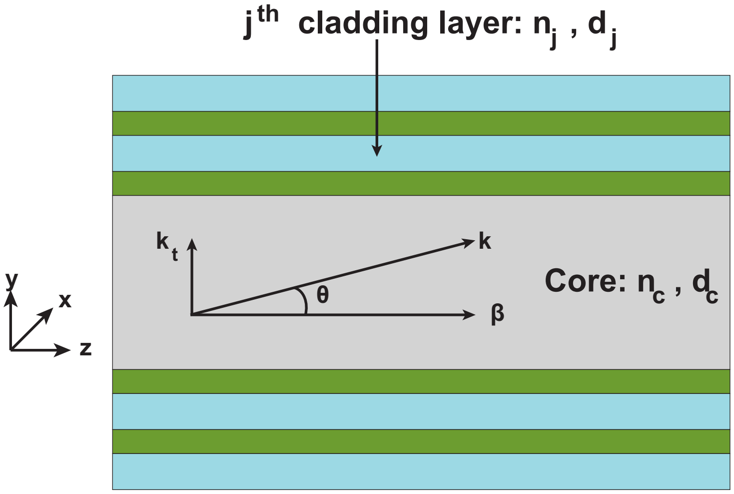

Figure 2.3 - Illustration of an ARROW waveguide.

A comparison with the Bragg waveguide design equations (2.3) and (2.4) shows that (2.6) is identical to the Bragg waveguide thickness in (2.3). However, in an ARROW waveguide, (2.6) holds for any layer, regardless of the refractive index. This implies that high reflectivity and hence low waveguide loss can be obtained without relying on the periodicity of the structure. Any layer satisfying (2.6) will reduce loss because it acts as an antiresonant Fabry-Perot cavity [73]. Unlike a Bragg waveguide, the

ARROW cladding can be made of a variety of materials with varying thicknesses. This allows for significant design flexibility compared to standard photonic crystals which require periodicity in the layer structure.

2.4.2 Optical Characteristics of ARROW Waveguides

As with Bragg waveguides and other photonic crystals, ARROWs are leaky waveguides. Loss is due to partial reflection by the cladding layers, and can be reduced by increasing the number of layers. To investigate the loss characteristics of ARROW waveguides, numerical simulations were performed in Matlab using a 1-dimensional slab structure like that in Figure 2.3. The method used for these simulations is known as the field-transfer matrix method [74]. Using this method, the reflection coefficient for the layer stack is calculated and then used to solve for the modes of the waveguide, yielding the effective index and hence the mode loss. The structure used for these simulations had a water core (n=1.33) and cladding layers of silicon dioxide and silicon nitride, terminated on top with air and on bottom with silicon (n=3.85). The layer thicknesses shown in Table 2.1 were calculated using (2.6) at a design wavelength of 785 nm and core width of 3.5 μm.

Table 2.1 – Calculated layer thicknesses for a water-core ARROW waveguide optimized for propagation at 785 nm.

Cladding material	Thickness (nm)
SiN (n=2.10)	120
SiO_2 (n=1.46)	320

The waveguide loss characteristics described in this dissertation are reported in terms of the exponential loss coefficient, α. The light intensity at a given point in the waveguide is given by:

$$I(z) = I_0 e^{-\alpha z} \tag{2.8}$$

where I_0 is the initial intensity and z is the distance traveled. Values of α, given in units of cm^{-1}, can be converted to units of dB/cm by multiplying by 4.34 [75].

Figure 2.4 shows the loss dependence of an ARROW waveguide on the core width and number of layer pairs. The loss decreases with increasing core width and with increasing numbers of layers. For each additional pair of layers, the loss decreases by ~3*x*. This suggests a design tradeoff between waveguide loss and fabrication complexity. The waveguides discussed in this dissertation use three layer pairs.

Also evident from the figure is the fact that ARROW waveguides are polarization dependent. A wave propagating with the electric field oriented in the **x** direction as shown in Figure 2.3 (transverse electric, TE) experiences lower loss than a wave with the magnetic field along **x** (transverse magnetic, TM) due to the lower reflection coefficient for a TM wave [76]. As a result, a waveguide with two-dimensional confinement should be oriented so the light is polarized along the larger core dimension in order to minimize loss.

Due to the dependence on the broad transmission minimum of a Fabry-Perot resonator, ARROW waveguides exhibit good performance over a range of wavelengths. Figure 2.5 shows the wavelength dependence of the ARROW structure described above.

The simulations give a 3-dB bandwidth of 235 nm, centered at the design wavelength of 785 nm. Additional curves are shown for nitride refractive indices of 1.9 and 2.4, showing that loss decreases and bandwidth increases with a higher refractive index. This effect is also observed in Bragg reflectors [55] and omniguides [60].

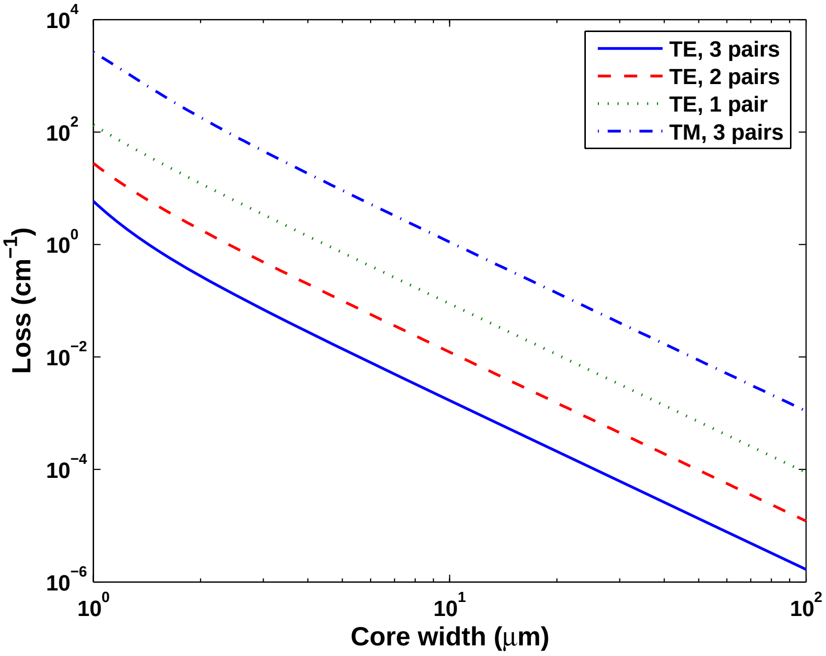

Figure 2.4 - ARROW loss vs. core width. TE loss is shown for 1, 2 and 3 pairs of cladding layers. TM loss is shown for 3 pairs of layers.

Another useful result of the Fabry-Perot characteristics of the ARROW waveguide is insensitivity to variations in fabrication. This is particularly important with our fabrication process, as some variations in film thickness are inevitable with the equipment used. Figure 2.6 shows the normalized waveguide loss as a function of normalized thickness variation for single layers and for all layers combined. From these simulations, a 5% deviation in thickness in a single layer will increase the loss by ~1%.

The sensitivity of loss to thickness variation decreases slightly for the outermost layers, as the field strength is lower further from the core. A 5% variation on all layers increased the loss by 8%. As will be discussed in Chapter 3, the tolerances of our fabrication process are well within 5% of the nominal values.

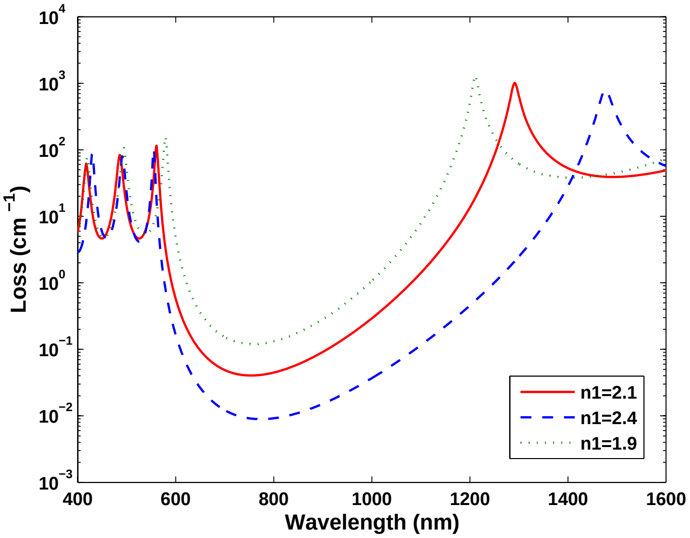

Figure 2.5 - Wavelength dependence of waveguide loss in a water-core ARROW waveguide designed for propagation at 785 nm. The 3-dB bandwidth is 235 nm for n=2.1.

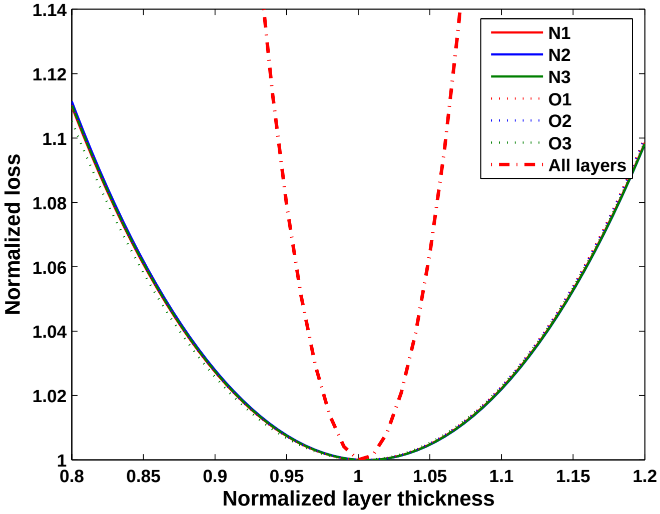

Figure 2.6 - Sensitivity of ARROW loss to variations in layer thickness. Both loss and thickness are shown normalized to their nominal values.

2.4.3 ARROW-based Optical Filters

One useful component for integrated optics is a wavelength-selective filter. ARROW-based filters proposed previously use resonant coupling between waveguides to achieve wavelength selectivity [77], [78]. We have developed an alternative filter structure based on the inherent wavelength selectivity of Bragg reflectors [25]. By adjusting the refractive index or thickness of the filters, the peak reflectance value can be tuned. Our method adjusts the layer thickness, as this is easier to change than the refractive index of a given film. Additionally, not every layer needs to be changed for efficient filtering.

For normal operation, the dielectric layers in the ARROW cladding operate as antiresonant Fabry-Perot cavities, as discussed above. This results in high reflectivity and low waveguide loss. If a layer is in resonance for a given wavelength, however, it will experience low reflectivity and high loss. A wavelength λ_1 at resonance in the jth layer experiences a round-trip phase shift which is an even multiple of π, which can be expressed as follows:

$$\Phi_2 - \Phi_1 = 2M\pi \approx 2\sqrt{n_i^2 - n_c^2}\,(k_2 - k_1)t_j\,. \tag{2.9}$$

For low-loss propagation at λ_2, the thickness t_j must meet the following condition with p odd:

$$t_j = \frac{p\lambda_2}{4\sqrt{n_i^2 - n_c^2}}\,. \tag{2.10}$$

Inserting the value for t_j from (2.10) into (2.9) leads to the following condition for M:

$$M = \frac{\lambda_2 - \lambda_1}{\lambda_1} p . \tag{2.11}$$

In general, (2.11) cannot be solved for integer M and p for any given λ_1 and λ_2. However, due to the thickness tolerance of the ARROW waveguide, values of (M,p) can be found that are close to the required conditions. Additionally, not all of the ARROW layers need be modified to achieve good wavelength selectivity. A filter design for transmission in a water core at $\lambda_2 = 690$ nm and attenuation at $\lambda_1 = 633$ nm gives $M = 1$ and $p = 11.1053$. Setting $p = 11$ for the bottom nitride layers gives the following layer structure:

Table 2.2 - Layer thicknesses for integrated water-core ARROW filter designed for transmission at 690 nm and attenuation at 633 nm. The bottom nitride layers are 11x the nominal thickness.

Layer	Thickness (nm)
Oxide 6	283
Nitride 6	106
Oxide 5	283
Nitride 5	106
Oxide 4	283
Nitride 4	106
Core	3.5 μm
Nitride 3	1166
Oxide 3	283
Nitride 2	1166
Oxide 2	283
Nitride 1	1166
Oxide 1	283
Substrate	-

Figure 2.7 shows the simulated loss characteristics for this structure. It is evident that increasing the order *p* of the nitride layers has a significant effect on the wavelength selectivity of the waveguide. For $p = 1$ (dotted line), the waveguide exhibits a broad passband which is characteristic of ARROW waveguides. The filter design discussed above, with $p = 11$ for the nitride layers on the bottom of the core, is shown as a solid line. The wavelength discrimination is excellent for this design, on the order of 10^4. As will be discussed in Chapter 8, integrated optical filters are extremely useful for fluorescence sensing platforms.

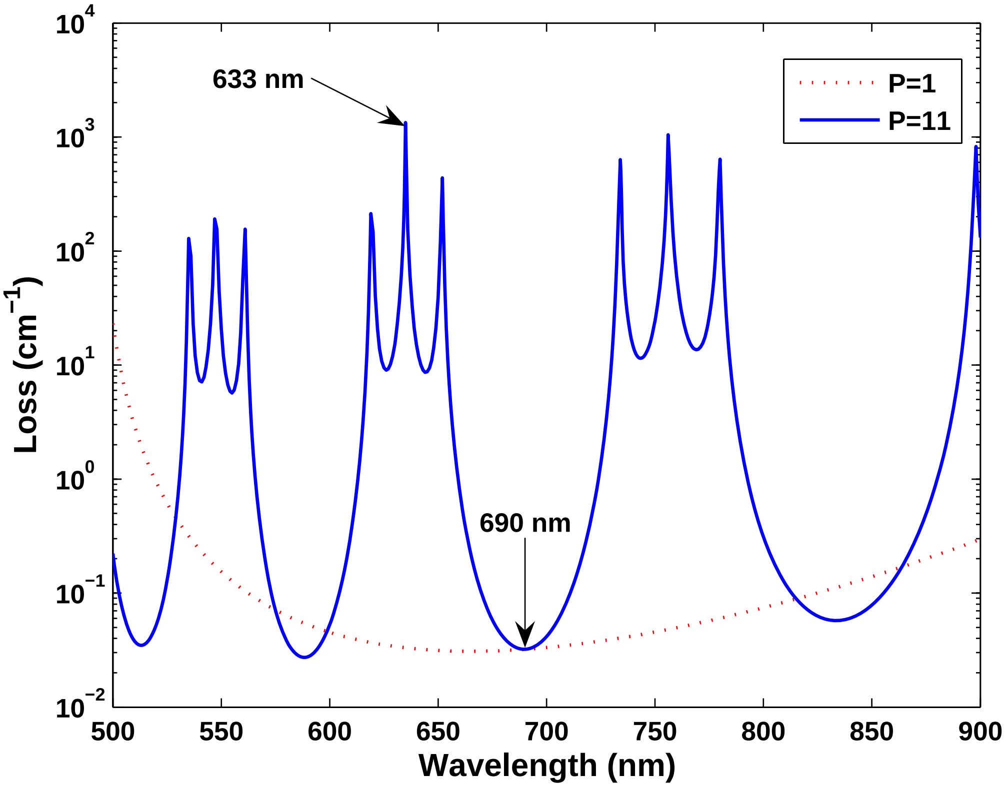

Figure 2.7 - Simulated loss vs. wavelength of integrated ARROW filter. The filter (solid line) is designed for transmission at 690 nm and attenuation at 633 nm. A standard ARROW (dotted line) is shown for comparison.

2.5 Conclusions

This chapter has presented an overview of optical waveguiding in low-index materials such as gases and liquids. Conventional index guiding is not feasible for gases, and is difficult for liquids due to the requirement of a low-index cladding. The available low-index cladding materials such as Teflon AF® and nanoporous silica are difficult to integrate into a planar device. The alternative to index guiding is to use photonic crystals, which consist of periodic arrays of dielectric materials. Bragg waveguides and holey fibers are two major classes of photonic crystals, and have been shown to guide light in low-index cores including gases and liquids.

The ARROW waveguide is similar to a Bragg waveguide. Cladding layers of an ARROW waveguide function as antiresonant Fabry-Perot cavities with high reflectance. Unlike Bragg waveguides, the cladding layers in an ARROW waveguide do not require periodicity, which gives additional design flexibility. This flexibility will be discussed in subsequent chapters when it is used to adjust the mechanical and optical properties of the hollow ARROW waveguides we have fabricated.

3 Hollow Waveguide Fabrication Process

3.1 Introduction

The object of the research described in this paper was to develop a robust method to fabricate hollow ARROW waveguides on planar substrates. The fabrication process was designed to utilize standard semiconductor processes and equipment available in the BYU Integrated Microfabrication Laboratory (IML). As discussed in Chapter 1, the optical design of the ARROW waveguides was performed at UC Santa Cruz, while the fabrication process, the topic of this research, took place at BYU.

The hollow waveguides built using this process must meet several important criteria. First, reasonable lengths - on the order of 1 cm - must be achievable to enable integration into optical sensing platforms. The inner surface of the waveguide must be smooth in order to minimize light scattering and turbulent fluid flow. Additionally, the dielectric layer structure of the waveguide must be uniform and controlled in order to achieve low-loss waveguiding, and also provide sufficient mechanical strength to prevent waveguide breakage during processing and subsequent usage.

Three general methods exist for fabricating hollow structures on planar structures. Wafer bonding can be used to form hollow channels by forming a trench on the substrate, then covering it with a material which is thermally bonded to the substrate, forming a sealed channel [79]. Wafer bonding has been proposed for the fabrication of hollow ARROW waveguides [71]. Fabrication of such devices with core dimensions on the order of 100 μm is reported in [72]. Hollow omniguide-type devices made by wafer bonding are detailed in [80]. Wafer bonding requires a very high degree of flatness to ensure good bonding, meaning structures with large topography cannot be incorporated. This limits the range of microfluidic and microelectronic devices that can be integrated with waveguides formed using this technique. A second fabrication method for hollow Bragg waveguides using self-sealing channels was mentioned in [81], although little detail of the fabrication process was given.

The third method is to use a sacrificial core around which the structure is grown [82]. The core is then removed, leaving a hollow channel. This method, known as surface micromachining, is extensively used in the fabrication of microelectromechanical systems (MEMS) [83]. Surface micromachining takes advantage of the well-developed base of silicon manufacturing processes and equipment. Fabrication of waveguides using this process allows easy integration with microfluidic and microelectronic devices.

This dissertation describes the development of a robust fabrication process for hollow optical waveguides using surface micromachining. This chapter will provide an overview of the fabrication process and give detailed information about parts of the process not related to the sacrificial core. The application of the sacrificial core process to ARROW waveguide formation is the key innovation of this research, and will be described in detail in subsequent chapters.

3.2 Process Overview

The method we have developed to fabricate hollow ARROW waveguides takes advantage of existing silicon microfabrication technology and equipment available in the IML. An illustration of the basic process is shown in Figure 3.1. The waveguides are made using 100 mm diameter silicon wafers as a substrate material. Wafers with a crystal orientation of <100> are used to facilitate cleaving the waveguides after fabrication. Alternating layers of silicon dioxide and silicon nitride are deposited on the wafer using a plasma-enhanced chemical vapor deposition (PECVD) reactor. These layers form the bottom of the ARROW waveguide.

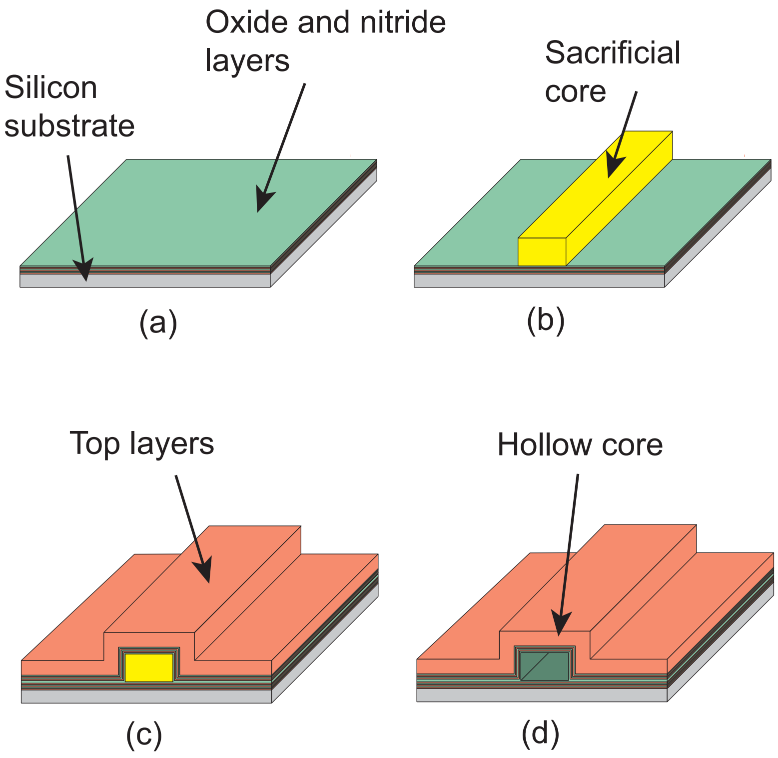

Figure 3.1 - Basic hollow ARROW fabrication steps. (a) Bottom dielectric layer deposition by PECVD. (b) Sacrificial core deposition and patterning. (c) Deposition of upper layers by PECVD. (d) Removal of sacrificial core, leaving a hollow waveguide.

A sacrificial core is used to support the upper dielectric layers during fabrication, giving shape to the waveguide. The core should be easy to pattern yet be able to withstand the elevated temperature and reactive environment of the PECVD process. The core material must also be able to be removed after fabrication without damage to the waveguide. We have fabricated waveguides using three different core materials, including aluminum, SU-8 and AZ 3330 photoresist. The choice of core material determines the core shape and strength, as well as the etchant used to remove it. The three types of cores will be discussed individually in subsequent chapters.

After core deposition and patterning, the wafer is returned to the PECVD to form the upper waveguide structure. Like the bottom layer stack, alternating oxide and nitride layers are deposited to form an ARROW structure. The final layer of oxide is much thicker than the other layers to provide mechanical strength to the finished waveguide, typically near 2 μm. Like the rest of the layers, the thickness of this layer is chosen to form an antiresonant Fabry-Perot cavity, as discussed in Chapter 2.

At this point, the ARROW waveguide structure is complete. Ridge waveguides can be patterned in the top oxide layer and will be detailed in Chapter 7. Openings are then made to the ends of the waveguide, either by cleaving the wafer or reactive ion etching (RIE) through the top layers. The device is then immersed in an acid solution to remove the sacrificial core.

The sacrificial core must be removed from the waveguide without affecting the shape or quality of the dielectric cladding layers. This requires the use of an etchant with extremely high selectivity in order to remove the core material without etching the cladding layers. To etch the core materials used in our fabrication process, we use acid solutions which have no significant etch rate of either silicon dioxide or silicon nitride, leaving the cladding layers intact. Aluminum cores are removed with a solution of *aqua regia*, a 3:1 mixture of nitric and hydrochloric acids. The SU-8 and photoresist cores are removed in Nano-Strip™, a stabilized solution of sulfuric acid and hydrogen peroxide. The details of the core removal etch are described along with the core materials in subsequent chapters

3.3 Microfabrication Processes

3.3.1 PECVD

3.3.1.1 Overview

Plasma-enhanced chemical vapor deposition (PECVD) is a common technique used in semiconductor fabrication to deposit dielectrics such as silicon dioxide and silicon nitride, as well as polycrystalline silicon. A diagram of a basic PECVD reactor is shown in Figure 3.2. Reactant gases are introduced at controlled rates into the chamber. Typical reactant gases include silane (SiH_4), nitrous oxide (N_2O) and ammonia (NH_3). The chamber is operated at a low pressure, usually 300 to 900 mTorr, controlled by means of a mechanical vacuum pump and vacuum throttle valve. Substrate material is placed on a platter which is heated to between 250 and 350°C. Due to the relatively low temperature of the process chamber, the gases do not react in their normal state. A source of RF energy is used to ionize the gas mixture, creating a plasma. In the plasma state, the gases can react to form the desired film on the heated substrate. The chemical processes in PECVD are complex and not fully understood, and involve many intermediate chemical species. However, a typical reaction can be described as follows, ignoring the intermediate steps:

$$SiH_4 + 2N_2O \xrightarrow{RF+heat} SiO_2 + 2H_2 + 2N_2. \qquad (3.1)$$

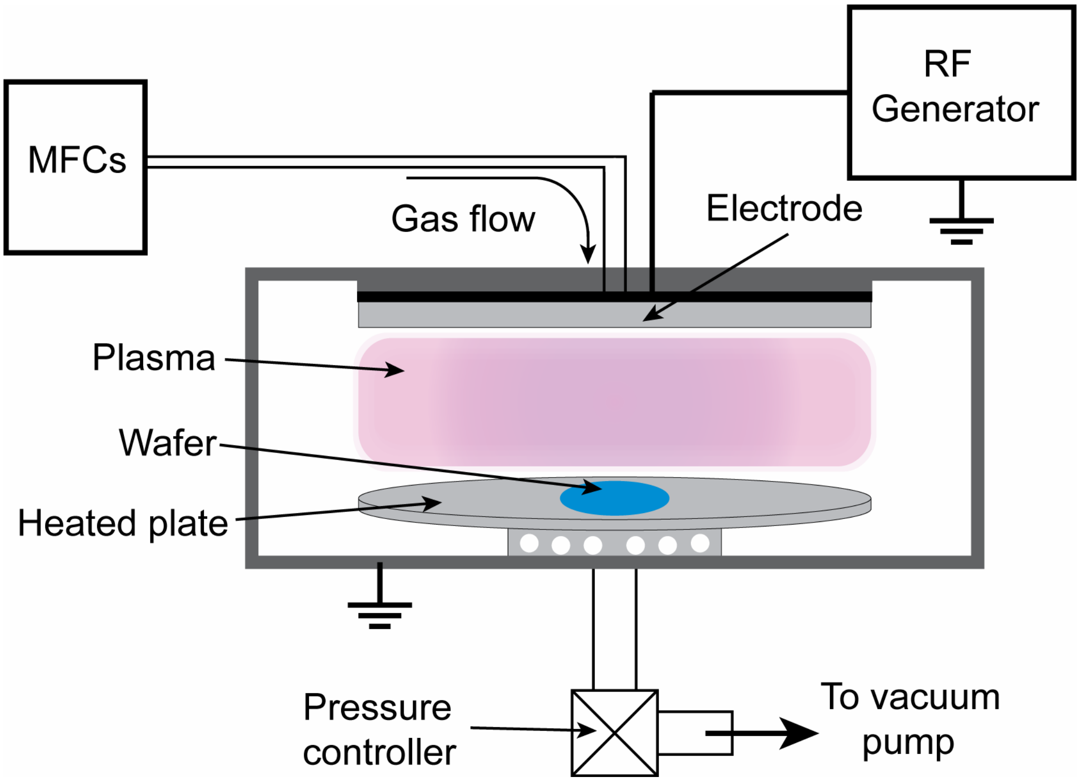

Figure 3.2 - Diagram of a typical PECVD reactor.

The PECVD reactor used for this research is a custom-built system based on a PE-II parallel-plate plasma etcher, identified in the IML as PECVD 1. It utilizes a total of four gases, controlled by mass flow controllers and a 500 W RF power supply with an automatic tuner operating at 13.56 MHz. The pressure in the chamber is controlled by a vacuum throttle valve and has a range of 100 to 1000 mTorr. The reactor is typically operated in manual mode, meaning the user directly sets the gas flows, pressure, temperature and RF power level and time. The process gases used are listed in Table 3.1.

Table 3.1- Process gases used in PECVD deposition.

Gas Name	Gas	Purpose
Gas 1	NH_3	Nitrogen source for SiN_x deposition
Gas 2	SiH_4 (5%) / He (95%)	Silicon source for all film depositions
Gas 3	N_2O	Oxygen source for SiO_2 deposition
Gas 4	CF_4 (92%) / O_2 (8%)	Chamber cleans

The waveguides described in this paper use alternating layers of silicon dioxide (SiO_2, also referred to as oxide), and silicon nitride (SiN_x, nitride). Both films can be grown in PECVD 1 using the recipes described in Table 3.2. All depositions take place at 250°C and 900 mTorr. Due to the complexity of the PECVD process, recipe development is difficult, generally involving much trial and error. The recipes shown here represent the current best-known values, and much potential for improvement remains.

3.3.1.2 Film Conformality

The PECVD deposition process is not isotropic, as shown in Figure 3.3. Because film growth is the result of adsorption of reactant molecules from the plasma located above the wafer surface, film growth is faster on horizontal surfaces than on vertical surfaces such as the side of a rectangular core. This effect is dependent on chamber pressure and substrate geometry. Higher chamber pressure results in more collision scattering of the reactant molecules and hence a more isotropic deposition. The height of the vertical surface also affects the deposition rate on the surface, with greater height leading to lower deposition rates on the vertical walls. Typically, the ratio of the horizontal growth rate to the vertical growth rate is between 1.2 and 1.5. In order to achieve low optical loss, this effect must be accounted for in the design of the ARROW layer structure [23], and will be discussed in Chapter 5. It is suggested in [84] that proper PECVD recipe optimization can produce highly conformal films, but this has not been attempted with our equipment.

Table 3.2 - PECVD deposition recipes used for hollow waveguide fabrication. Recipes shown are for (a) oxide deposition and (b) nitride deposition. All depositions take place at 250°C and 900 mTorr.

(a)

Parameter	Value	Units
Gas 2 Flow (SiH_4/He)	104	sccm
Gas 3 Flow (N_2O)	17.8	sccm
RF Power	50	W
Growth Rate	22	nm/m

(b)

Parameter	Value	Units
Gas 1 Flow (NH_3)	6	sccm
Gas 2 Flow (SiH_4/He)	104	sccm
RF Power	100	W
Growth Rate	7	nm/m

3.3.1.3 Particle Formation and Chamber Conditioning

PECVD film deposition is a relatively dirty process. Dielectric films build up in the chamber, especially on the chamber top and sidewalls. These films then flake off during processing, resulting in small particles on the surface of the wafer. The particles contribute to waveguide loss, and cause lithography defects when patterning the core and ridge etch layers, resulting in cracked and incomplete waveguides. To reduce particle related defects, particle deposition on the wafer must be controlled and the particles that do get on the wafer must be removed.

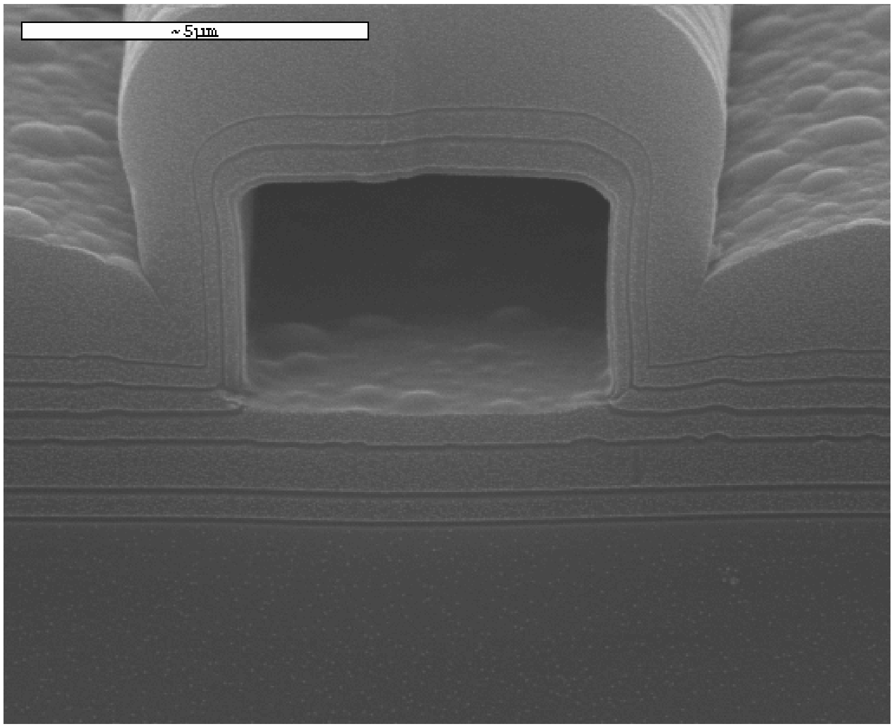

Figure 3.3 - SEM image of a hollow ARROW waveguide showing difference in layer thicknesses on the sides and top of the waveguide core due to the PECVD deposition process

To reduce particle formation in the chamber, the machine must be thoroughly cleaned before use. The chamber clean process uses CF_4 gas to remove buildup on the chamber walls, and should be performed before each layer deposition for optimal results. For oxide deposition, a chamber clean followed by a 5 minute deposition with an empty chamber results in good particle control. The chamber should be cleaned after every 30 minutes of deposition, corresponding to about 700 nm of deposited oxide. For thicker film layers such as the final oxide layer on an ARROW waveguide, the deposition should be broken into several steps of 30 minutes length, with a chamber clean between each step.

Nitride deposition is a more complex process due to the non-stoichiometeric film composition and thermodynamic favorability of oxide growth over nitride. Thus, careful control of chamber conditions is necessary to produce a film with the desired optical properties. We have found that a thorough chamber clean followed by 2 hours of deposition in an empty chamber is required to obtain acceptable control of the film's refractive index. The drawback is that a thick coating of particles is produced on the top of the PECVD chamber. If undisturbed, nitride particles have a very low tendency to flake off compared to oxide particles, but care must be taken to not disturb the coating during wafer loading and unloading.

3.3.1.4 Film Characterization

The ARROW waveguide designs discussed here require film thicknesses on the order of 100 nm. To minimize waveguide loss, it is desirable to fabricate devices with layer thicknesses as close as possible to the design values, as well as control the refractive index of the films. An ellipsometer is used to measure the thicknesses and refractive indices of films deposited on silicon test wafers, and these values are used to determine the growth rate of the process chamber and hence the length of the deposition run.

One area for concern in the PECVD process is the uniformity of the deposited film. Due to chamber geometry, gas and RF power density are not uniform in the PECVD, resulting in variations in film thickness across the wafer. Additionally, the deposited film thickness will vary from run to run due to slight differences in chamber conditions. Although the ARROW waveguide has a high tolerance for film thickness variations, it is desirable to minimize these variations for best optical performance. A thorough characterization of film growth in the PECVD was performed to analyze the ability to produce uniform films with the desired optical characteristics.

It should be noted here that nitride deposition is a much more challenging process than is oxide deposition. This is due to two factors. First, the nitride films grown in the PECVD are not stoichiometric, meaning that the ratio of silicon to nitrogen atoms varies from the ideal Si_3N_4 chemistry that can be achieved through other processes. For this reason, PECVD nitride films are usually designated as SiN_x to indicate that the silicon-nitrogen ratio is variable. Changes in the Si:N ratio are manifest as variations in the refractive index of the nitride film [85].

Many factors affect this ratio, including power, pressure, temperature and especially gas flows in the PECVD. In order to achieve the desired refractive index, the flow of ammonia (NH_3) is varied, based on ellipsometric measurements of test wafers. For our devices, the desired refractive index is generally 2.05, and the measured index of the test wafers ranges from 2.0 to 2.15. A lower ammonia flow will yield a higher refractive index (silicon-rich film) [86].

The other factor affecting nitride deposition is its thermodynamic unfavorability relative to oxide formation [85]. This means that any oxygen in the PECVD chamber, either from chamber leaks or adsorbed onto the chamber surface, will be incorporated into the deposited film in the form of silicon oxynitride [87]. This results in the film having a low refractive index. In practice, we have found that the condition of the surface of the PECVD chamber strongly affects the refractive index of the nitride film.

In order to reduce the amount of oxygen adsorbed onto the surface, a thorough chamber clean must be performed before nitride deposition. This is followed by a long nitride growth with an empty chamber. A nitride film is thus deposited on the chamber surface which acts as a barrier to oxygen diffusion. Typically, a 2 hour seasoning is performed in this manner, and gives acceptable control of the index of refraction of the nitride film.

3.3.1.5 Film Uniformity

To characterize the uniformity of deposited films, a series of wafers were run through the PECVD and then measured on the ellipsometer to determine the run-to-run variability of the films. Additionally, measurements were taken at several locations on each wafer to determine the variability across the wafer surface. The measurement locations are shown in Figure 3.4. Repeated measurements of the same location on a wafer give the same result, implying that the repeatability of the ellipsometer is equal to or better than its resolution.

Before depositing the nitride films, a three hour chamber seasoning was performed as discussed above, while the oxide wafers were preceded by a 10 minute seasoning run. A total of 6 nitride wafers were deposited for 10 minutes each, giving a nominal film thickness of 75 nm, and 5 oxide wafers each received a 6 minute deposition for a nominal thickness of 138 nm. The depositions took place consecutively to minimize any changes in the equipment or environment. The nominal film thicknesses chosen give a high measurement sensitivity in the ellipsometer, and are the test wafer thicknesses used to determine growth rates during the hollow ARROW fabrication process.

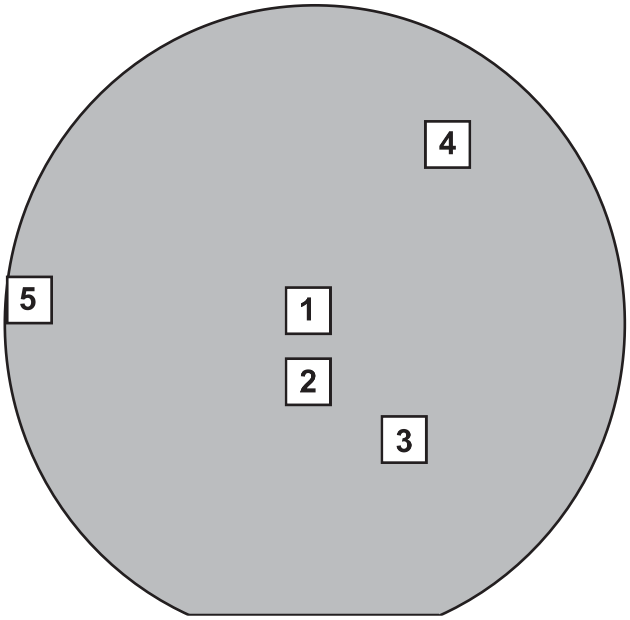

Figure 3.4 - Measurement locations for PECVD test wafers.

The results for nitride growth are shown in Figures 3.5 through 3.8. To examine run-to-run variation, the data are shown grouped by wafer. As can be seen in Figure 3.5, the nitride growth rate decreases with each run. Taken together with the increasing refractive index trend shown in Figure 3.6, it is evident that after three hours of deposition, the chamber is still not completely seasoned. The last three wafers, however, have very similar films, suggesting that 3.5 hours of nitride deposition is sufficient to season the chamber. In spite of this trend, the thickness variation from run to run is small compared to the tolerances for ARROW fabrication discussed in Chapter 2, indicating that the procedure used for hollow ARROW fabrication, consisting of depositing a test film and using the measured value to set the deposition time for the product wafer, will produce acceptable results.

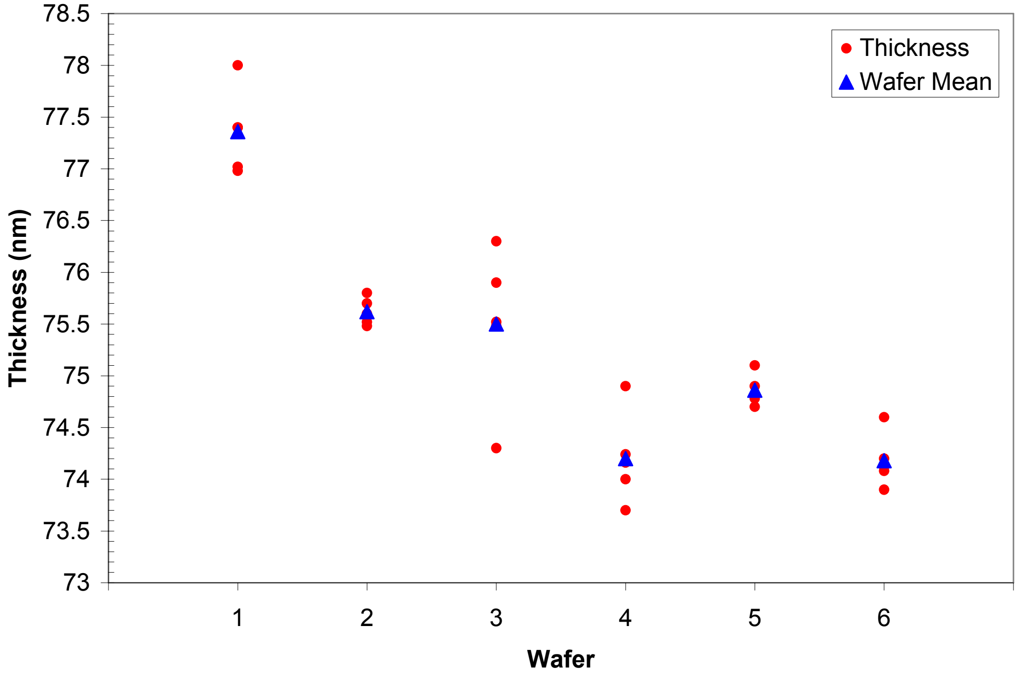

Figure 3.5 – Nitride thickness grouped by wafer. Small dots are individual measurements on each wafer. Large triangles represent the wafer mean thickness.

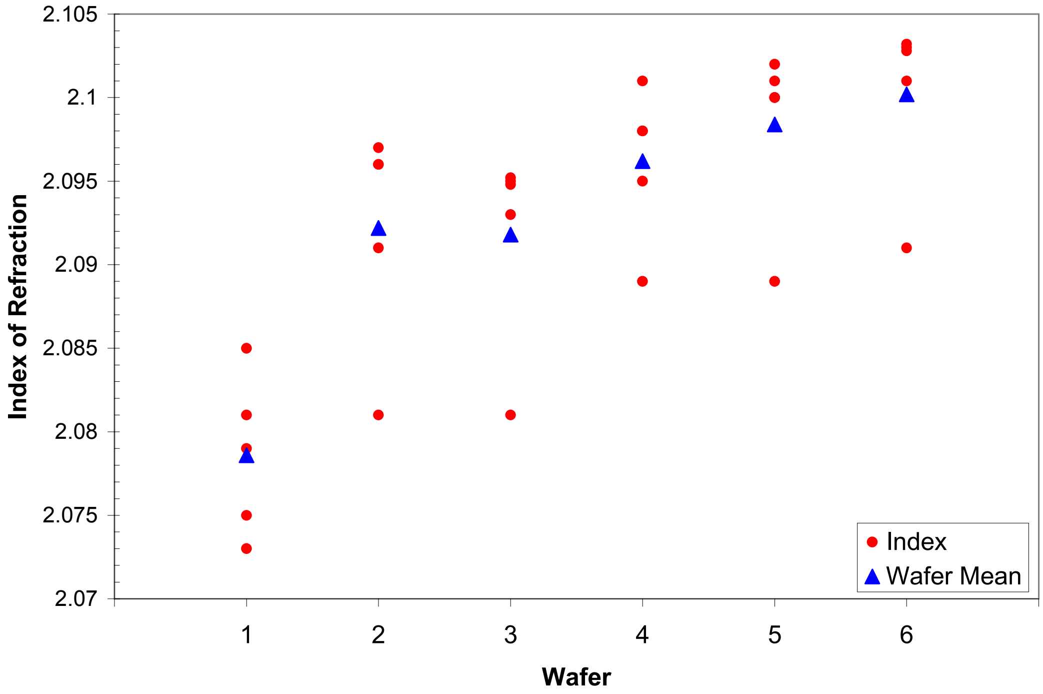

Figure 3.6 - Nitride refractive index, grouped by wafer. The small dots represent individual measurements, while the triangles represent the mean refractive index for the wafer.

Variability of the nitride films across the wafer is very good. The same data plotted above are shown in Figures 3.7 and 3.8, grouped by measurement location. Lines connect the set of measurements taken from a given wafer. As shown in Figure 3.4 above, the distance from the center of the wafer increases with sample location starting from location 1 in the center to location 5 approximately 3 mm from the edge of the wafer. The thickness values vary by less than 2% across a wafer, while the refractive index varies approximately 1% across the wafer. These results indicate that nitride uniformity across a wafer is well within acceptable limits based on the tolerance of ARROW waveguides to thickness variations discussed in Chapter 2.

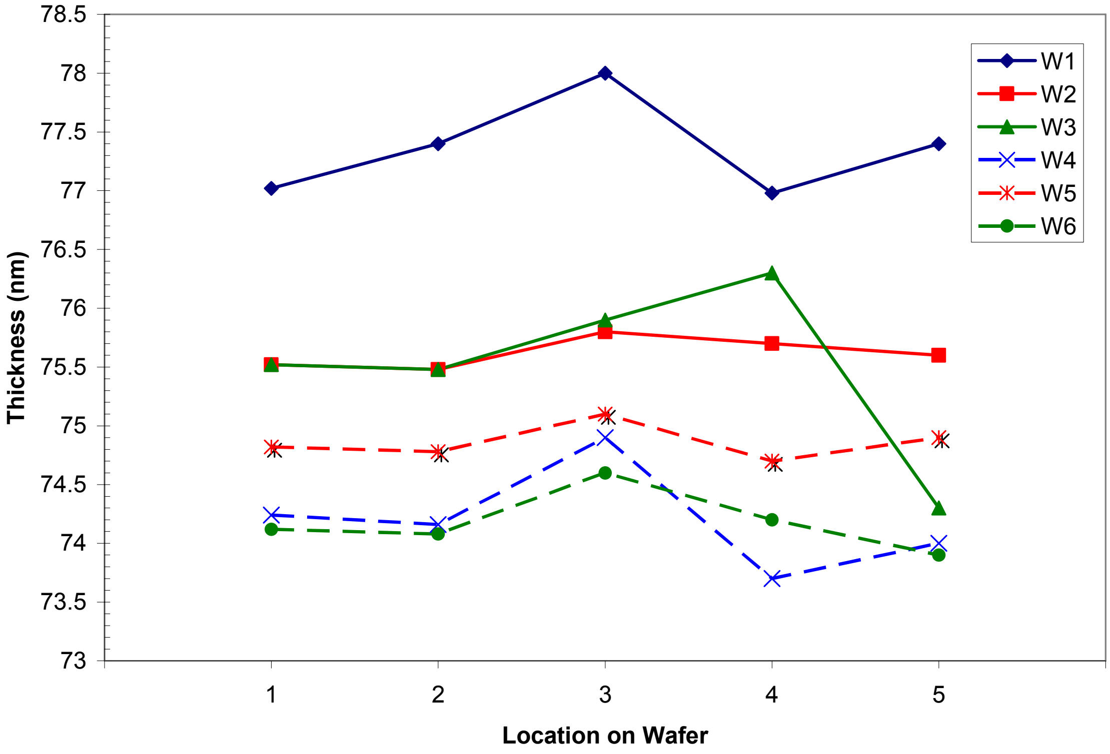

Figure 3.7 - Nitride thickness grouped by measurement location. Lines connect measurements within a wafer.

The results of the oxide wafer test runs are shown in Figure 3.9. The thickness of the deposited oxide film increases with each wafer. This effect is most marked between the first and second wafers. Although a 10 minute deposition was performed to season the chamber before the first wafer was run, from this graph it can be concluded that a longer deposition would improve control over the film deposition rate. However, it should be noted that the variation in film thickness due to this effect is less than 2%, so waveguide performance should not be strongly affected.

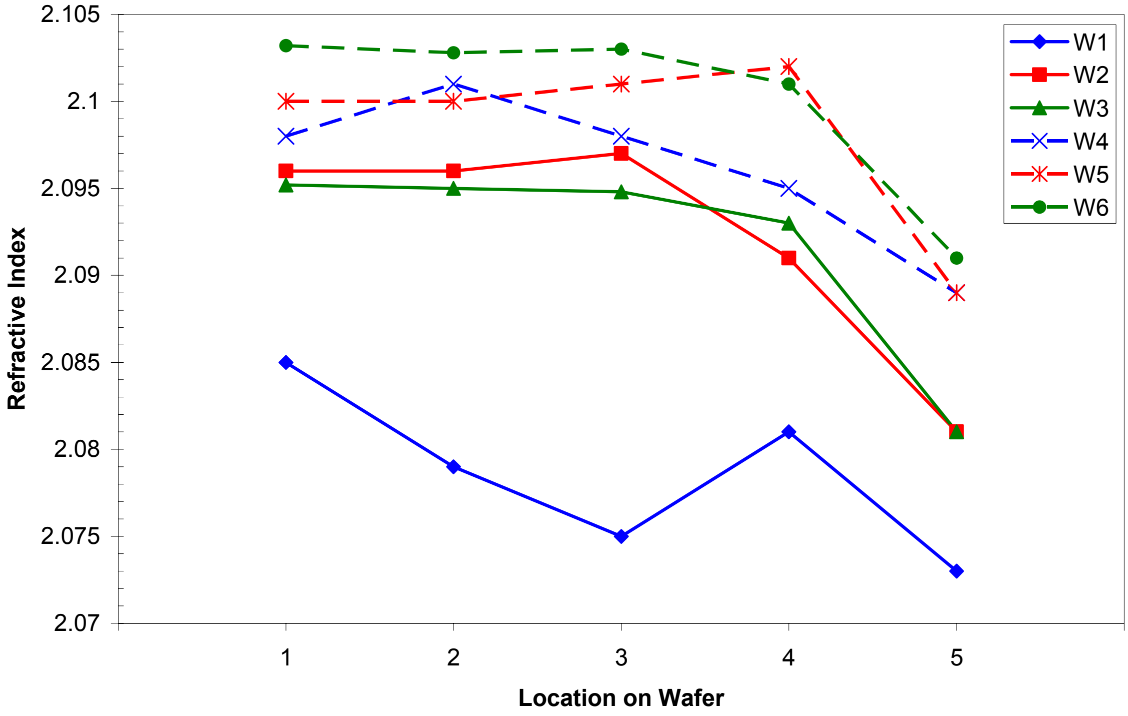

Figure 3.8 - Nitride refractive index grouped by measurement location. Lines connect measurements from the same wafer.

Figure 3.10 shows the oxide data plotted by sample location on the wafer. Lines connect samples from the same run to show the variation across the wafer. No major trend is observed here, with a maximum variation of 2% on wafer 1. Although not plotted here, the variation in refractive index of the oxide films was extremely small, less than 0.1%.

Early in the characterization of PECVD 1 for hollow ARROW fabrication, it was noted that film uniformity across the surface of the wafer was poor. Typically, the film thickness was approximately 25% thinner near the edge of the wafer compared to the center. It was found that placing spacer wafers around the wafer in the center of the plate reduced this thickness variation to less than 5%. The mechanism for this is not understood, but all current PECVD deposition at BYU requiring uniform films, especially ARROW waveguide fabrication, makes use of this technique.

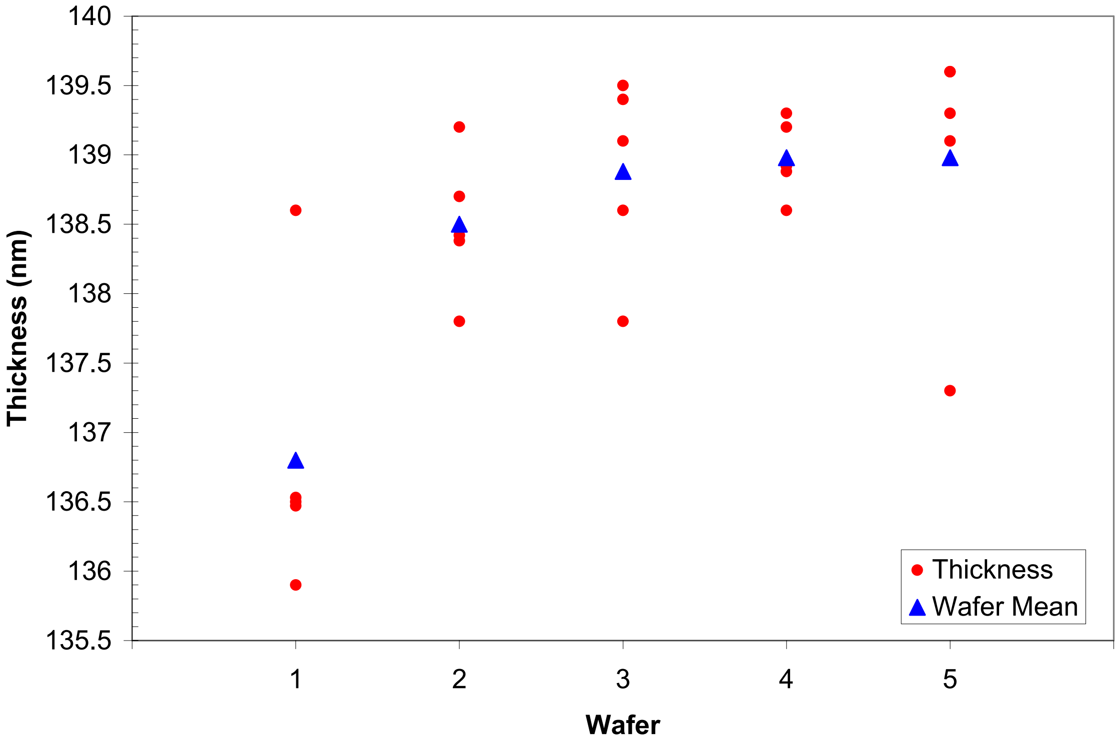

Figure 3.9 - Oxide thickness grouped by wafer. Small dots represent individual measurements. Large triangles represent the wafer mean thickness.

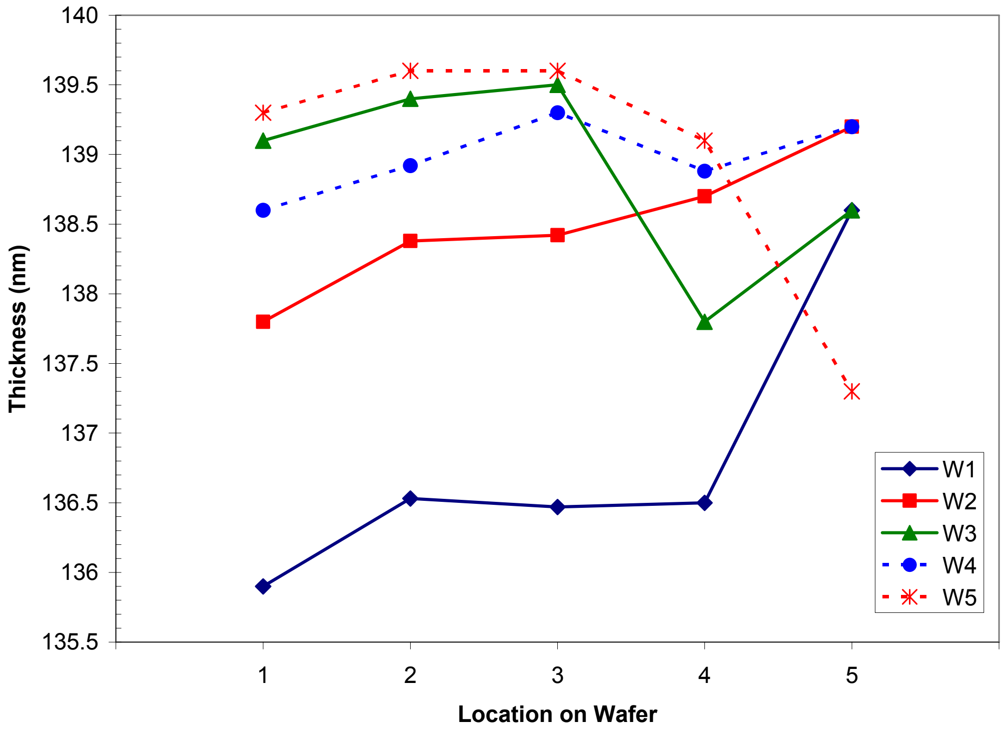

Figure 3.10 - Oxide thickness grouped by measurement location. Lines connect measurements from the same wafer.

3.3.1.6 PECVD Film Stress, Density and Annealing

PECVD films have intrinsic stress when deposited. This stress is a result of several factors including incorporation of impurities in the film, grain boundary movement and microscopic voids in the film [87]. In the hollow ARROW fabrication process, film stress can cause delamination between layers and cracking of the upper waveguide structure. So far, little work has been done to characterize this aspect of the PECVD processes used in the BYU IML. It is known that film stress is affected by the applied RF power, gas composition, temperature and pressure [88], [89]. However, the interactions between these variables are complex and not fully understood. For nitride deposition, it is reported that the addition of nitrogen gas into the process chamber can modulate film stress [90]. Another method is to use a dual-frequency RF power supply which can control the degree of ion bombardment and film sputtering during the deposition process [91].

Another issue inherent to PECVD film deposition is film density. Films grown by PECVD typically have a porous structure caused by the condensation-nucleation based nature of the growth process and the low temperature at which the reaction takes place [92]. Additionally, it is reported that PECVD nitride films can contain up to 30% (atomic) hydrogen [93]. Increased temperature will decrease the amount of hydrogen, resulting in a denser film. However, the temperature range of the PECVD reactor and limitations of the materials placed in the reactor restrict the ultimate temperature range of the deposition.

It is expected that less dense films produced in the PECVD will experience higher optical loss due to scattering and roughness of the film. Measurements of optical loss could thus be a useful metric of film quality. To date, no such characterization has been carried out, but should be relatively straightforward given the new equipment in the IML. It should be noted that the original ARROW design used polycrystalline silicon as a reflective layer and still achieved low loss [65]. Thus, the optical losses of the oxide and nitride layers are not critical to the performance of hollow ARROW waveguides.

One possible method to densify the PECVD films is to anneal them after deposition. Typical annealing temperatures range from 400 to 800°C for tens of minutes [85],[94]. This process drives off hydrogen gas incorporated in the film and allows the grain boundaries to coalesce. This will result in a denser film and hence lower optical loss, as well as possibly reduced stress. Lack of equipment to characterize stress and optical loss has previously prevented the investigation of these effects of annealing.

However, in an experiment performed here, annealing oxide and nitride films at 600°C for 10 minutes has produced ~1% changes in the thickness and refractive index of the films as measured by the ellipsometer.

Unfortunately, attempts to anneal hollow ARROW waveguides have resulted in excessive breakage of the upper waveguide structure and have not been repeated. This is likely due to the film stress issues discussed above. Future studies of the annealing process combined with film stress characterization could yield further process improvements.

3.3.2 Wafer Cleans

To remove particles from the wafer surface, a solution known as standard clean 1 (SC-1) is used. SC-1 is a mixture of ammonium hydroxide (NH_4OH, 30% w/v), hydrogen peroxide (H_2O_2, 30% v/v) and DI water in a ratio of 1:1:10. This solution has been shown to be very effective in removing small particles from silicon wafers [95], [96]. It is suggested in [97] that reducing the ammonium hydroxide concentration to 0.1:1:5 enhances particle removal and reduces surface pitting. To perform an SC-1 clean, the wafer is immersed in the SC-1 solution and agitated for 10 to 30 seconds, then rinsed with DI water and dried with pressurized nitrogen. Under optical inspection, this method removes most visible particles from a wafer after PECVD deposition.

The SC-1 clean is used on unpatterned wafers between each film growth. After the sacrificial core is deposited, care must be taken to avoid damaging the core or the upper dielectric films. Early photolithography processes in the IML resulted in films with poor adhesion to the substrate. Thus, it was feared that the agitation and reactivity of the SC-1 clean would cause adhesion failure of the core material. Another risk is the cracking or removal of the upper dielectric films from around the core. This is due to their low thickness and currently unknown adhesion strength with the core material, exacerbated by the thermal cycling from the PECVD process. Thus, historically the SC-1 clean has only been performed on the wafer between layer growths before core deposition. The wafer is simply blown off with nitrogen after each upper layer deposition. This method removes fewer particles than an SC-1 clean, but is thought to have less risk of damaging the upper layer structure of the waveguide. One area of possible improvement in the fabrication process would be to investigate the effects of SC-1 cleaning on waveguide structures.

3.3.3 Photolithography

Photolithography is a method used to transfer patterns to a wafer surface, and is one of the fundamental techniques used in planar microfabrication. All photolithography uses a light-sensitive material applied on the substrate. This material, known as photoresist, is typically applied as a liquid to the wafer which is then spun for a short time. The photoresist thus forms a film whose thickness depends on the spin speed and time. After spinning, heat is applied to the wafer in a process known as a soft bake. The soft bake drives off solvent, leaving a solid layer of photosensitive material.

As shown in Figure 3.11, the wafer is then exposed to ultraviolet light through a glass and chrome mask. The UV light induces a chemical reaction in the photoresist, altering its solubility to a developer solution. Photoresists can be generally classified into positive and negative tones. A positive photoresist becomes more soluble after UV exposure, while a negative photoresist becomes less soluble due to chemical cross-linking. For negative resists, a post-exposure bake is usually performed to speed up the cross-linking process. The wafer is then immersed in a developer bath until the unwanted resist is removed, leaving a pattern which can be transferred to the substrate through etching.

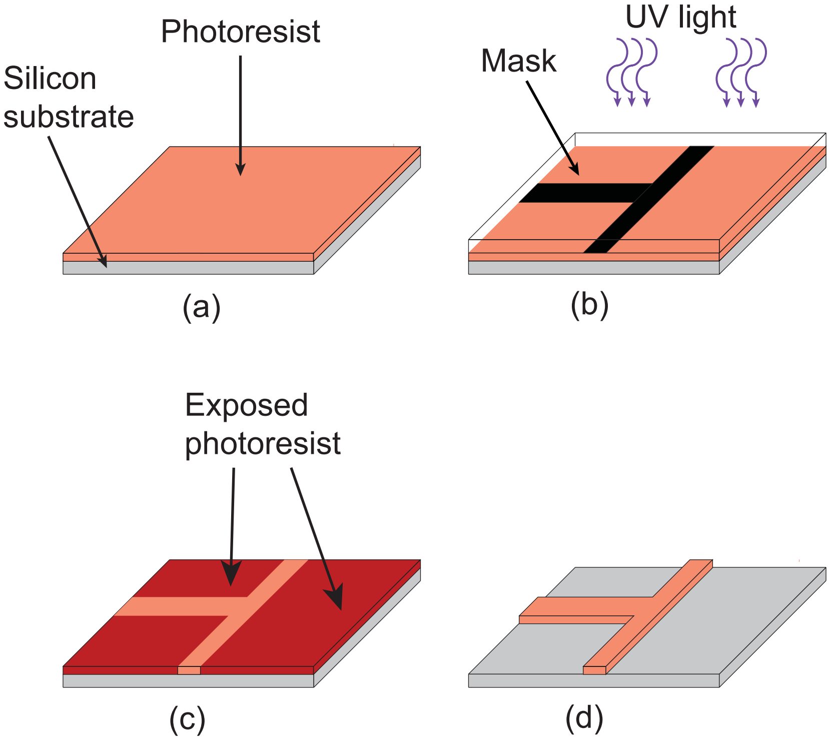

Figure 3.11 - Basic photolithography process. (a) Substrate coated with photoresist. (b) Substrate exposed with UV light through mask. (c) Photochemical reaction changes solubility of exposed photoresist. (d) Exposed photoresist removed in developer solution.

Photolithography is used in the hollow waveguide fabrication process to form the sacrificial core and to pattern structures on top of the hollow ARROW waveguides. For positive resist based photolithography, AZ 3330 photoresist is used, and SU-8 photosensitive epoxy is used for negative-tone processes. The specific processes and materials are discussed in subsequent chapters.

3.3.4 Etching

Etching is the process of removing material from the substrate. It can be generally classified into dry and wet etching. When discussing etching processes, several figures of merit commonly used include etch rate, which is the rate of removal of the desired material. Selectivity is the ratio of the etch rate of the material to be removed to the etch rate of surrounding materials, with a high selectivity meaning the surrounding materials are only weakly affected by the etchant. Finally, an etch is considered to be isotropic if the etch rate is the same in all directions, and anisotropic or directional if the etch proceeds in one direction preferentially.

Etching can be generally divided into wet etching and dry etching. Wet etching involves immersing the material in an etchant, typically an acid solution. This type of etch is generally isotropic. The etch rate and selectivity are determined by the choice of etchant, and are typically higher than for dry etching. Temperature and solution agitation also affect the etch rate. In this research, wet etching is used to remove the sacrificial core and to pattern aluminum films used to create the sacrificial core.

Dry etching takes place in a reactor using a mixture of gases which are ionized using RF energy. The ions then adsorb onto the wafer surface and react with the substrate materials, forming reaction products which diffuse away in the gas mixture. The etching is typically a combination of chemical reaction and physical sputtering of the material by the energetic ions. Controlling the ion energy can affect the degree of anisotropy of the etch. For example, reactive ion etching (RIE) involves the application of a large DC bias which accelerates the ions into the substrate, resulting in a very anisotropic etch. Plasma etching utilizes little to no DC bias and is thus more isotropic due to scattering of the ions due to molecular motion. Selectivity is determined by the gas mixture used, but is typically lower than wet etching due to the degree of physical etching by the ions. RIE etching is used to form patterns in the upper dielectric layers of the ARROW waveguides, as well as to form pedestal structures in the silicon substrate. These processes are detailed in subsequent chapters.

3.4 Waveguide Evaluation

It is desirable to evaluate the performance of the fabrication process to facilitate improvements in said process. This section will discuss the general goals of the hollow waveguide fabrication process and three areas of evaluation relating to these goals. In the subsequent chapters, the results of actual waveguide fabrication are presented along with the specific processes used to create the waveguides.

3.4.1 Fabrication Complexity

The fabrication process detailed in this dissertation is complex, involving multiple film depositions, wafer cleans and patterning steps. Significant time and effort is required to complete these steps. Therefore, it is desirable to minimize the complexity of the fabrication process while still meeting optical performance criteria. One important tradeoff is the number of ARROW cladding layers. As discussed in Chapter 2, additional cladding layers reduce the optical loss of the waveguide. However, each layer requires significant fabrication time due to the processing requirements of the PECVD. The waveguides discussed here have three pairs of layers surrounding the waveguide, representing a compromise between fabrication complexity and optical loss.

The core removal process is very time-consuming, with 2 cm long waveguides often needing 3-4 weeks to complete the etch. This introduces a lag time between design and testing of the waveguides, delaying characterization of both the design and the fabrication process. Therefore, any steps that can be taken to minimize the core removal etch time are valuable. The next three chapters discuss in detail the core removal process for each type of sacrificial core and efforts undertaken to optimize the etch process.

3.4.2 Mechanical Strength

Due to the low thickness of the upper dielectric layers of waveguides fabricated using our process, they are vulnerable to breakage. The breakage can be generally classified into three categories. First is breakage during the fabrication process. During the core removal process, gas is generated inside the partially etched core, causing a buildup of pressure. This pressure can crack the waveguide or completely break off sections of the upper layer structure, as shown in Figure 3.12. In order to characterize this failure mode, mechanical studies of the strength of the waveguides have been performed. Results of these studies were used to formulate design rules for the physical dimensions of the waveguides. These data are discussed in detail in the next three chapters. Additionally, we have observed variation in the mechanical quality of PECVD-grown films, especially oxide. Problems of this nature include films with a cloudy appearance under optical inspection and simple excessive breakage of the etched waveguides. The source of these variations is unknown, therefore careful monitoring of the film quality is essential to the success of the fabrication process.

Another source of waveguide failure occurs when the devices are cleaved. Because multiple devices are fabricated on a single wafer, the wafer must be cleaved in order to access the individual devices. The cleaving process can damage the end facets of the waveguides, as shown in Figure 3.13. To minimize this damage, the wafers are thinned before cleaving. Thinning takes place on a mechanical polishing tool, and the samples are thinned from their original thickness of 525 µm to approximately 300 µm before cleaving. Future improvements to this process might be obtained by polishing the facets, but will require thorough characterization to avoid damaging the fragile upper waveguide structure.

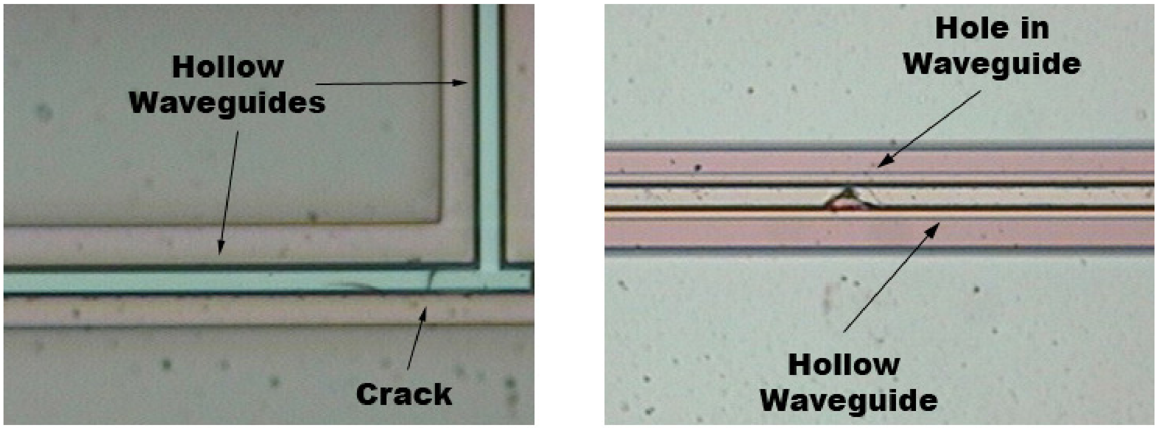

(a) (b)

Figure 3.12 - (a) Optical microscope image of a crack in upper dielectric layers of a hollow ARROW waveguide. (b) Hole in upper layers of a hollow ARROW waveguide. Magnification 200x.

Finally, breakage can occur during handling of the completed waveguides. Rubbing or scratching the top of the device will cause severe breakage. However, the waveguides have been observed to have sufficient strength to withstand normal conditions including handling and use in microfluidic systems, with both positive and negative pressure differentials.

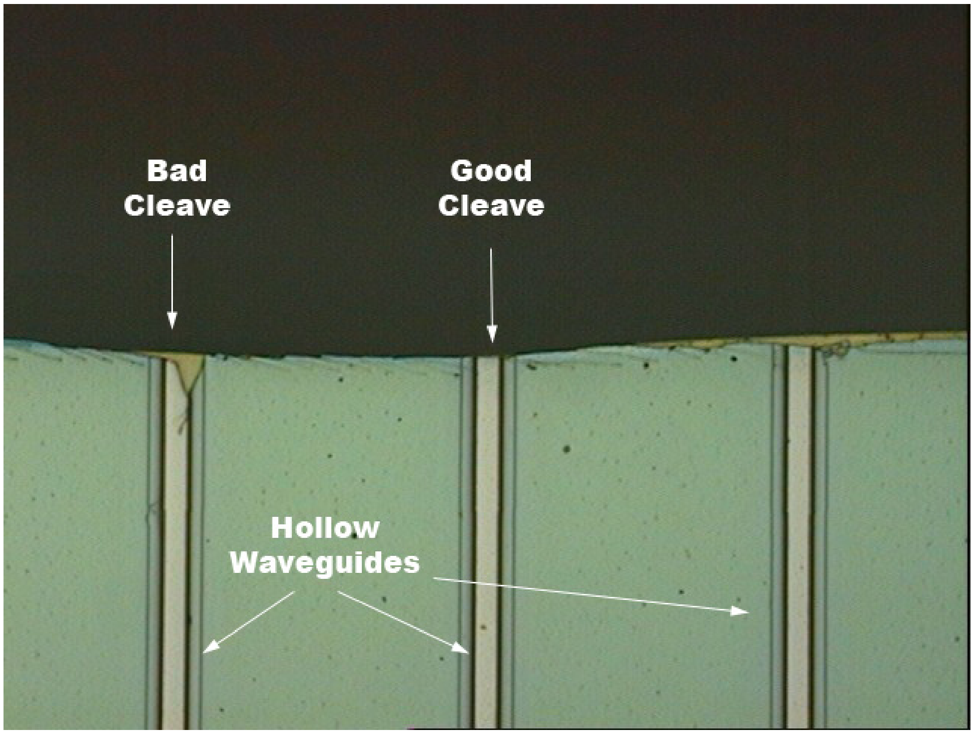

Figure 3.13 - Optical microscope image of the cleaved facet of a group of hollow ARROW waveguides, showing good and bad cleaves. Magnification 200x.

3.4.3 Optical Performance

The ultimate metric of the success of the fabrication process described here is the optical performance of the completed waveguides. Optical evaluation criteria include optical loss and spectral performance. Additionally, verification of the design process includes measurements of the modal characteristics of the waveguides and comparison to simulation results. As mentioned previously, design and testing of the waveguides took place at UC Santa Cruz. Optical results are included here for completeness, and are described in the following chapters, along with test methods.

4 Aluminum Sacrificial Core

4.1 Introduction

As discussed in Chapter 3, the key aspect of the fabrication process that is the subject of this research is the use of a sacrificial core around which the waveguide is formed. The choice of sacrificial core material determines both the shape and the mechanical strength of the hollow waveguide. Ideally, the material should be inexpensive and easily deposited and patterned using established planar microfabrication techniques. In addition, it must be capable of withstanding the high temperature and reactive environment of the PECVD process without damage.

The original concept for our method was to use PECVD silicon dioxide as the sacrificial core, which would then be removed in a buffered solution of hydrofluoric acid (BOE). The intended result was that the BOE etch would be capable of removing the oxide core while leaving the surrounding nitride layer intact. However, initial studies of the etch rates of PECVD oxide and nitride grown at BYU showed a selectivity of approximately 20:1. This is much too low to be suitable for the fabrication of long waveguides, as the nitride cladding layers would be etched along with the sacrificial core.

The next material considered for the sacrificial core was aluminum. Aluminum was chosen based on its ease of deposition and the availability of etchants with extremely high selectivity to the dielectric cladding layers. This chapter details the aluminum-based process and describes experiments performed to characterize the mechanical strength and core removal rate of waveguides fabricated using this process.

4.2 Fabrication Process

4.2.1 Aluminum Deposition and Patterning

4.2.1.1 Evaporation

Aluminum is extensively used in microfabrication due to its low cost and ease of deposition and patterning. For the process described here, aluminum was deposited via thermal or e-beam evaporation, depending on equipment availability. Metal evaporation is used to deposit thin metallic films by melting the metal in a vacuum chamber at very low pressure, typically in the range of 1×10^{-6} Torr. The metal evaporates and is deposited on the substrate material. This method can easily produce films with thicknesses on the order of 1 μm. Aluminum is easily evaporated compared to other metals due to its relatively low melting point and high vapor pressure.

4.2.1.2 Lift-off

To form optical waveguides with low loss using the method outlined in this paper, the sacrificial core must be patterned into the desired waveguide shape with low roughness. For patterning aluminum, two general methods are used. The first is a standard wet etch, where a photoresist pattern is created on top of the aluminum film. The film is then etched in an acid solution, typically a mixture of phosphoric, nitric and acetic acids, transferring the photoresist pattern to the aluminum film. As discussed in Chapter 3, the wet etching process is isotropic, so the photoresist will be undercut. This makes control of the dimensions of the sacrificial core difficult. In addition, wet etching of aluminum in the IML has been observed to produce uneven or jagged lines. This phenomenon renders wet-etched aluminum unsuitable for hollow waveguide formation.

The second technique to pattern aluminum is known as the lift-off method, and is the method used here to produce aluminum sacrificial cores. In the lift-off process, illustrated in Figure 4.1, a photoresist pattern is first created on the substrate, with voids where aluminum is desired. Aluminum is then deposited via evaporation. The photoresist is then removed in a solvent solution, leaving a bare substrate with patterned aluminum.

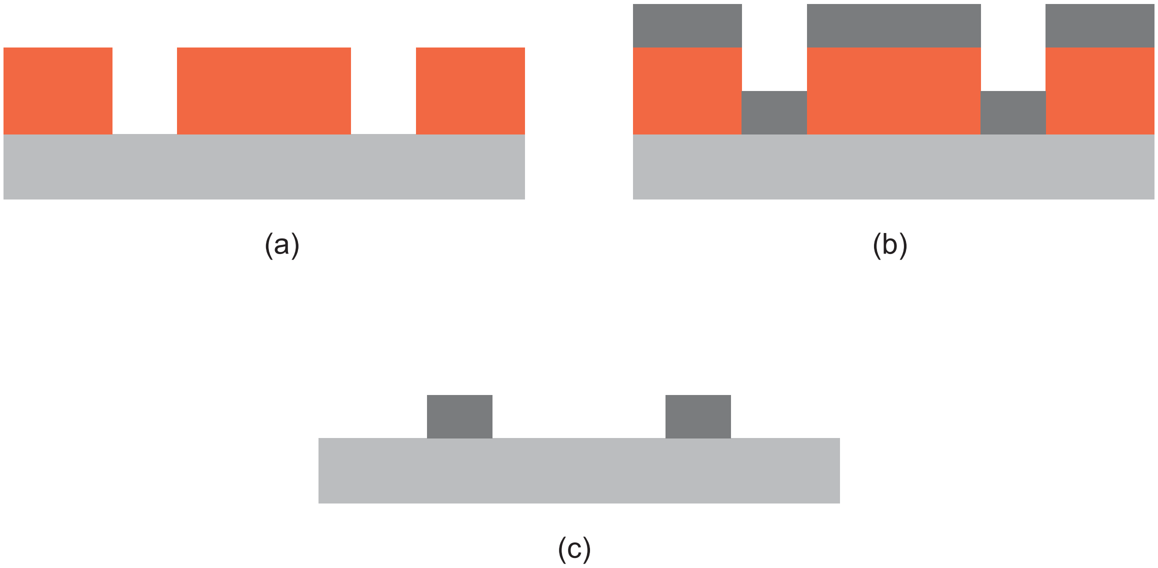

Figure 4.1 - Illustration of the lift-off patterning process. (a) A photoresist pattern is created on the substrate. (b) Aluminum is deposited via evaporation. (c) The photoresist is removed, leaving a pattern of aluminum on the wafer.

For lift-off patterning, a photoresist with a square or undercut profile is desirable to facilitate removal of the metal film. Typically, negative-tone photoresists such as SU-8 have the desired profile, while positive photoresist does not. It is clear from the above illustration of the lift-off process that the deposited film must be thinner than the photoresist layer to ensure discontinuity of the film at the pattern edges and hence reliable lift-off of the unwanted film. Our experiments with this process indicate that the thickness of the deposited film should be no higher than approximately 0.5x the resist height to ensure reliable lift-off.

The lift-off process produces a trapezoidal-shaped aluminum line. This is due to shadowing of the deposited line by the photoresist mask from the aluminum evaporation source. The trapezoidal shape results in good mechanical properties for the hollow waveguide, as discussed below. An SEM image of an aluminum-based device is shown in Figure 4.2, clearly illustrating the trapezoidal cross-section.

4.2.1.3 Cleans

An important aspect of the aluminum core process is obtaining a clean surface after patterning the core. During the initial development of the aluminum core process, significant debris was observed on the sides of the aluminum lines. In addition to the debris, adhesion problems between the top dielectric layers and the bottom layer stack were frequently observed after the core removal etch. This adhesion failure is believed to be due to residue from the lift-off process. A wafer cleaning process utilizing a 60 second oxygen plasma descum followed by a 3 second dip in 1:3 HCl/H_2O and deionized (DI) water rinse proved to be effective in eliminating the adhesion problems.

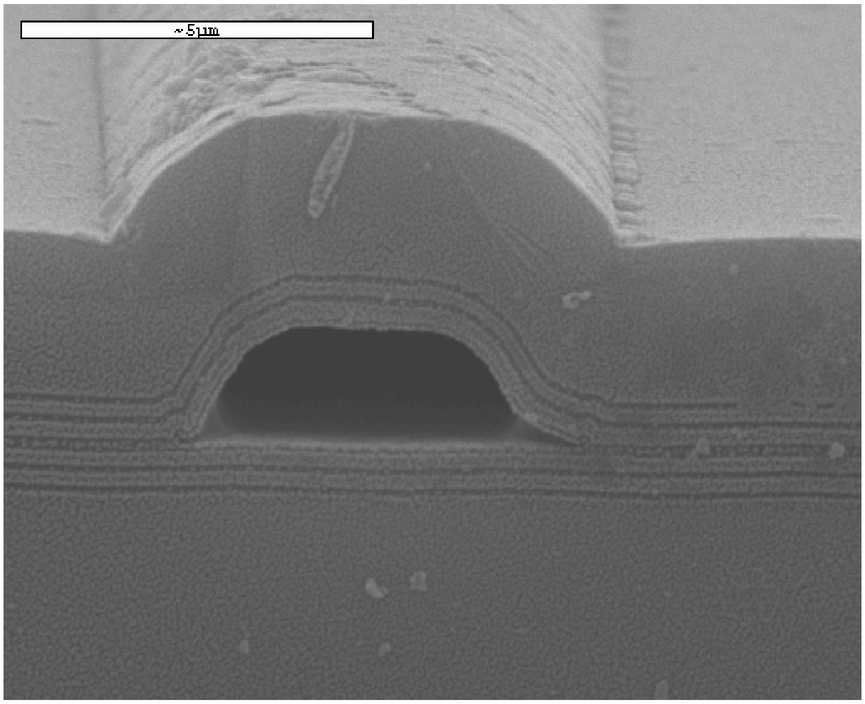

Figure 4.2 - SEM image of a hollow waveguide fabricated using aluminum as the sacrificial core. The alternating oxide and nitride layers are visible surrounding the hollow core. Waveguide dimensions are approximately 5 µm by 2.5 µm.

4.2.1.4 Other Issues

One significant drawback of the aluminum-based process is the roughness of the sacrificial core. This is due to a combination of roughness of the deposited aluminum due to grain structure, interactions of the aluminum lines and the PECVD process, and alloying of the aluminum to the dielectric waveguide structure [98]. Due to the conformal nature of PECVD film deposition, any small feature on the aluminum core is transferred to the upper dielectric layers. This roughness leads to increased optical loss due to scattering, and thus should be minimized. Although this is a significant problem with the aluminum-based process, the issue has not been pursued further due to the development of fabrication processes based on materials other than aluminum.

Another drawback to the use of aluminum as the sacrificial core material is the limitation on core height due to the deposition process. Due to limitations of the evaporation equipment used in the IML, it is difficult to achieve aluminum thicknesses greater than 3 μm. Although greater thicknesses (up to 5 μm) have been obtained, they are usually achieved at the expense of film quality due to the incorporation of graphite from the evaporation crucible into the film. Another approach to achieve thicker films is to perform multiple evaporation steps, but this requires exposing the wafer to the ambient environment between steps, resulting in adhesion problems between the layers of aluminum. Thus, a practical limit exists on the thickness of the aluminum core, which in turn limits the minimum optical loss achievable with waveguides built in this manner.

4.2.2 Core Removal

4.2.2.1 Etchant

Aluminum metal is readily etched by a variety of acids and bases. For efficient fabrication of long hollow waveguides, it is desirable to use an etchant with a high etch rate. An acid solution known as *aqua regia* was chosen as an ideal candidate. *Aqua regia* is a mixture of hydrochloric (HCl) and nitric (HNO_3) acids, typically in a ratio of 3:1 [99]. The resulting solution aggressively etches virtually all metals and has a low viscosity suitable for etching small channels. Both component acids are readily available. The *aqua regia* solutions described here use acid concentrations of 30% HCl and 68% HNO_3 in ratios of 3:1 to 2:1.

4.2.2.2 Etch Rates

Because of the small cross section of the core, the acid solution does not easily circulate, limiting the etch rate. The etching mechanism can be modeled as a diffusion-limited process, described by Deal and Grove's theory of silicon oxidation [100]. The channel length etched as a function of time has a square-root time dependency, given by

$$l(t) \approx \sqrt{2k_n D c_0 t} \tag{4.1}$$

where k_n is a constant relating to channel geometry, D is the diffusion coefficient of the etchant in the channel and c_0 relates to the active etchant concentration.

To form long waveguides on the order of 1 cm, significant etch time is required, generally more than a week. To minimize fabrication time, the etch rate must be as high as possible. To investigate the etch process, test structures were fabricated using the sacrificial core technique described above. These structures consisted of aluminum cores with a height of 700 nm and widths ranging from 6 to 300 μm. A single 3.0 μm layer of PECVD oxide was then deposited over the core. The structures were cleaved and then etched in *aqua regia* for varying times and temperatures.

Figure 4.3 shows a graph of the amount of aluminum etched as a function of etch time. Results are shown for structures with widths of 10 and 100 μm, and etches performed with a solution temperature of 55°C and 70°C. The length etched is the total length of aluminum removed from both ends of the hollow structure. The curves fit to the data points have a square root time dependence, indicating the diffusion-limited nature of the etch process described above. From the graph, the etch rate clearly increases with temperature, indicating an increase in the diffusion constant, and with increased cross-sectional area of the channel. The fastest conditions shown in Figure 4.3 indicate that a length of 4.5 mm can be etched in 24 hours. Although not shown in the graph, an *aqua regia* solution with a 2:1 HCl/HNO_3 ratio at 85°C can etch a 10 mm channel in approximately 24 hours.

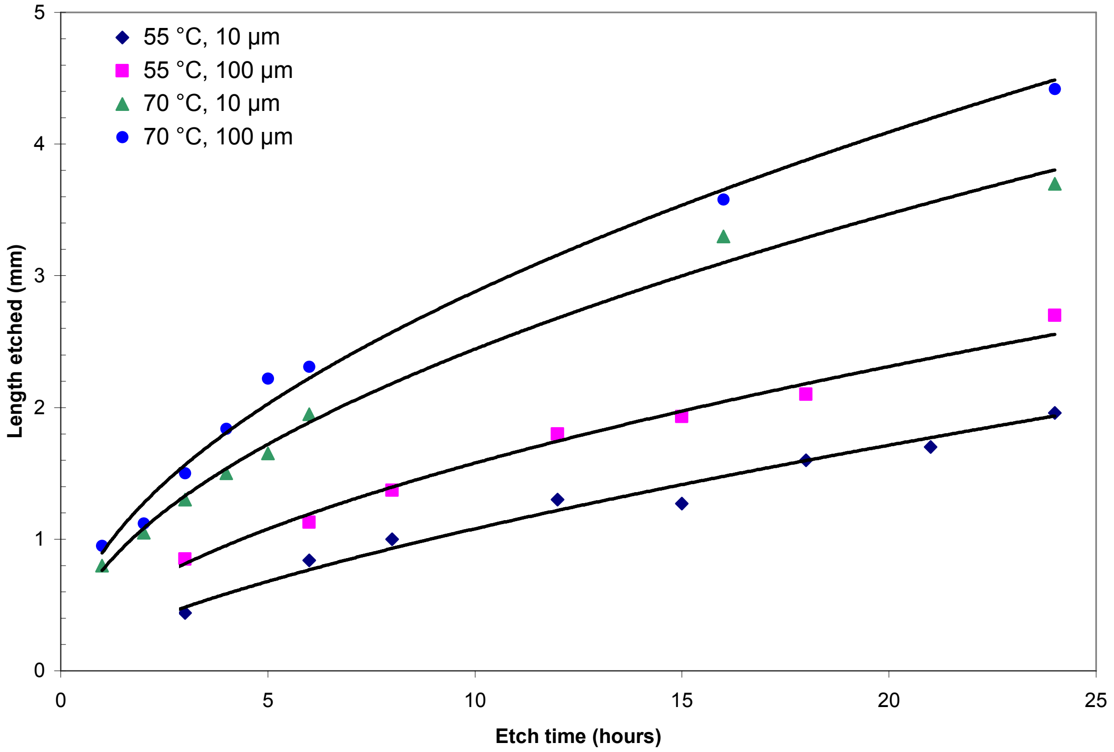

Figure 4.3 – Amount of aluminum etched in *aqua regia* at 55°C and 70°C for channels 10 µm and 100 µm wide. Fitted lines have a square-root time dependency.

Unfortunately, the etch rate cannot be arbitrarily increased by increasing the solution temperature. Gas formation during the etch process creates pressure which can lead to cracking and failure of the waveguide. In order to achieve reasonable yields from the production process, the solution temperature is limited to approximately 85°C.

4.3 Mechanical Strength

As discussed in Chapter 3, mechanical integrity is one of the key evaluation criteria for the fabrication process. Intact structures are essential for microfluidic applications to avoid fluid leakage and contamination. Gas sensing applications similarly require waveguides without cracks or breaks. Additionally, the optical performance of the waveguides is compromised by any defects in the structure.

In order to characterize the ability of the fabrication process discussed above to repeatably produce high quality waveguides, the mechanical structure was examined in depth. First, a mechanical analysis was performed using analytical techniques and modeling software. This study indicates that the most likely failure mode of the waveguides is internal pressure generated during the core-removal etch. Other failure modes such as vibration and thermal expansion are not significant for devices built with the dimensions used for our waveguides.

Using the reported values for SiO_2 for the elastic modulus (73 GPa) [101] and tensile strength (600 MPa) [102], structural failure points were computed based on internal pressure and device geometry. Figure 4.4 shows the predicted failure pressure of waveguide structures based on width and coating thickness. This graph indicates that devices fabricated in the range of our designs (10 μm core with 3 μm top layer thickness) can sustain high pressure before failure. The analysis suggests a design rule that the ratio of the device width to the upper layer thickness should be no greater than 35 to withstand a pressure of 1 MPa [26]. Therefore, a waveguide with a 1 μm thick upper dielectric structure should be no greater than 35 μm wide to ensure reliable fabrication.

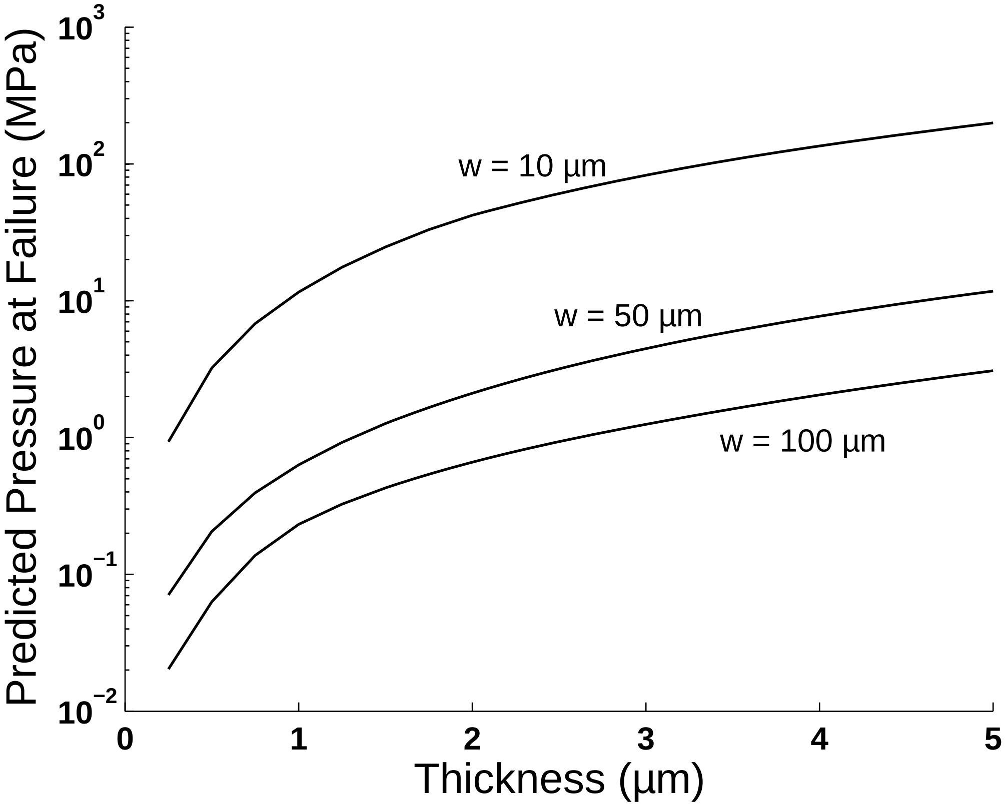

Figure 4.4 - Failure pressure of hollow waveguides predicted using finite element model. Critical pressure is plotted as a function of top layer thickness for three channel widths.

To verify the results of this study, test structures were grown on silicon wafers using aluminum cores of varying width and a single top layer of oxide ranging from 250 to 2000 nm thick. The samples were then etched in *aqua regia* at 55°C and inspected with an optical microscope to determine the integrity of the hollow channel. The results for four different top layer thicknesses are shown in Figure 4.5, indicating the amount of intact channel after etching for the different coating thicknesses and core widths. From this graph, it is clear that for a given coating thickness, there is a critical width below which the channel will be intact. Above the critical width, the failure rate increases dramatically. Using the 50% failure rates from this graph to estimate the ratio of device width to coating thickness gives a value of about 40, which is in good agreement with the design rule derived from the mechanical modeling.

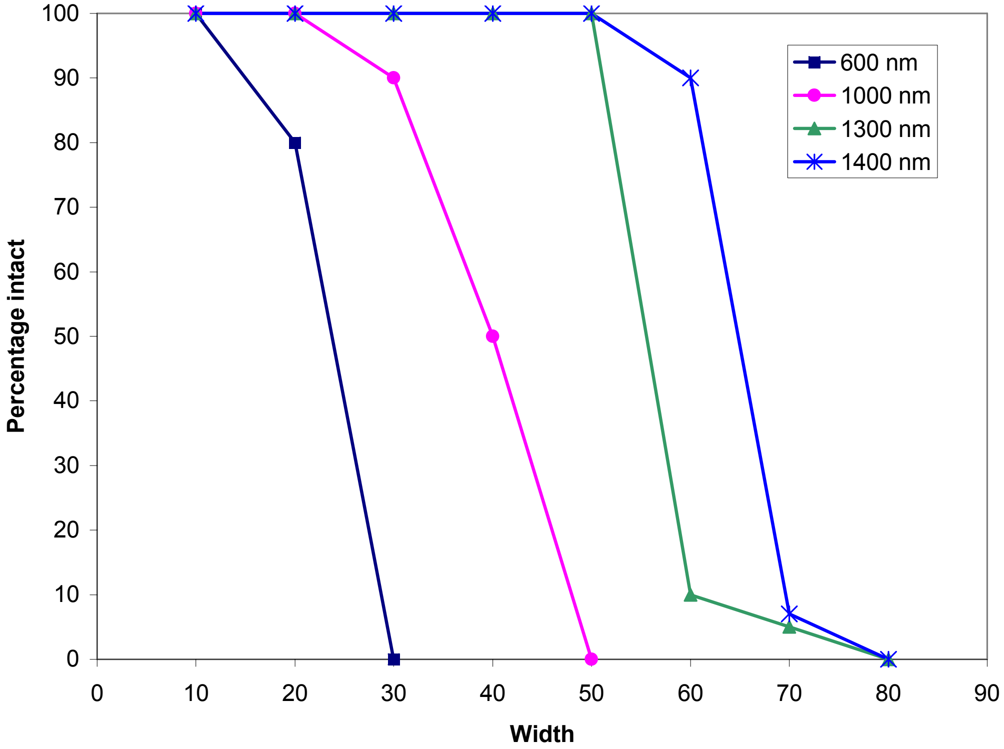

Figure 4.5 - Percentage intact of hollow channels after etching as a function of channel width for four top layer thicknesses.

4.4 Conclusions

Optical tests on waveguides fabricated with aluminum sacrificial cores were unsuccessful. This was due to the limited number of samples produced, the observed roughness of the waveguides and the limited maximum core height (~3 μm) which made optical coupling difficult and resulted in high optical loss. In testing, no light was observed to pass through any of the waveguides. However, the devices produced using this process served as a validation of the sacrificial core process. Samples were produced with lengths greater than 1 cm and widths ranging from 6-30 μm. Additionally, the strength and etch rate studies performed on aluminum-core samples provided understanding of the capability of the fabrication process, and illuminated many areas for improvement which will be discussed in subsequent chapters.

5 SU-8 Sacrificial Core

5.1 Introduction

Due to the roughness and limited core height of the aluminum-core waveguides, it was desirable to use a different material to form the sacrificial core. Ideally, the core material could easily be deposited with a wide range of thicknesses and be easily patterned with little roughness. The material must withstand the 250 °C vacuum environment of the PECVD chamber without damage. Finally, there must exist a suitable etch solution to remove the core in a reasonable amount of time and without damaging the dielectric layers of the waveguide. SU-8 photoresist, manufactured by MicroChem Corporation, was chosen as an ideal candidate. SU-8 is a negative-tone photosensitive epoxy material that can be processed using standard photolithographic techniques and has excellent mechanical properties due to the cross-linked nature of the epoxy.

5.2 Deposition and Patterning

SU-8 deposition is done following standard photoresist application methods. This is one of the key advantages of using SU-8 as the core material, as it is directly patterned by the photolithography process. No further etching or patterning steps are required, eliminating the possibility of roughness like what is seen with aluminum cores. The SU-

8 cores presented here use the SU-8 5 formulation, with a viscosity designed for film thicknesses from 2 to 5 μm [103].

After a 10 minute dehydration bake at 200°C, the wafer is placed on a spinner and approximately 10 ml of SU-8 is applied. The wafer is then spun at a fixed speed to provide the desired thickness. A plot of thickness is shown in Figure 5.1, demonstrating the inverse-square-root dependence of resist thickness on spin speed [104]. The waveguides discussed here have core thicknesses ranging from 3.5 to 5.8 μm.

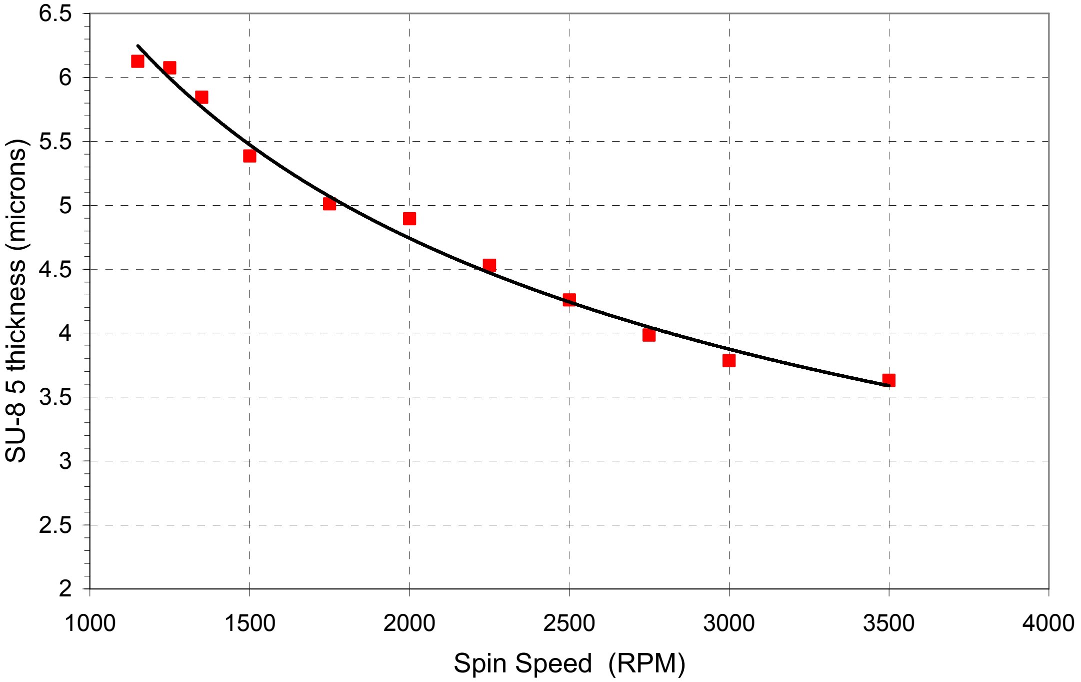

Figure 5.1 - SU-8 5 thickness vs. spin speed. The fitted curve has a square-root dependence on spin speed, characteristic of photoresist spin coating.

After spinning the wafer for 60 seconds, it is removed and placed on a hotplate at 65°C for 3 minutes. The hotplate temperature is then ramped to 95°C and held for an additional 3 minutes. This softbake step removes solvent from the SU-8 film, improving adhesion and resolution. The temperature ramp results in a slower solvent evaporation rate, improving adhesion and film surface quality [103]. The wafer is then exposed to UV light in a Karl Suss MA-150 aligner using the appropriate mask. The exposure time used ranges from 17 to 21 seconds at 10 mW/cm^2 intensity.

After the UV exposure, the SU-8 must be cross-linked. This takes place on a hotplate at 65°C for 3 minutes, ramped to 95°C and held for 3 minutes. The temperature ramp reduces stress and cracking in the cross-linked film [103]. The wafer is then immersed in SU-8 developer (PGMEA solvent from MicroChem Corporation) and agitated for 60 seconds. Upon removal from the developer, the wafer must be immediately rinsed in isopropanol (IPA) to remove all traces of the developer. The wafer is then dried with a nitrogen gun.

As seen in Figure 5.2, patterned SU-8 has a rectangular cross-section and very little surface roughness. These are ideal characteristics for waveguide formation. Additionally, due to its highly cross-linked nature, SU-8 is chemically resistant and can withstand the 250°C environment of the PECVD without damage or change of shape, meaning the shape of the SU-8 as patterned will be transferred directly to the final shape of the waveguide.

Adhesion problems of the SU-8 on nitride films have been observed. Therefore, the current process uses an adhesion promoter known as OmniCoat, also from MicroChem Corporation. OmniCoat is spun on at 3000 rpm after the dehydration bake and then cured on a hotplate at 200°C for 60 seconds. The use of OmniCoat provides excellent SU-8 adhesion to most substrates. After patterning the SU-8 normally, the OmniCoat must be stripped from the wafer surface. This is done in an oxygen plasma for

60 to 90 seconds. OmniCoat is rapidly etched by both hydrofluoric acid and ammonia, so the wafer cannot be cleaned by solutions containing these chemicals if OmniCoat has been used.

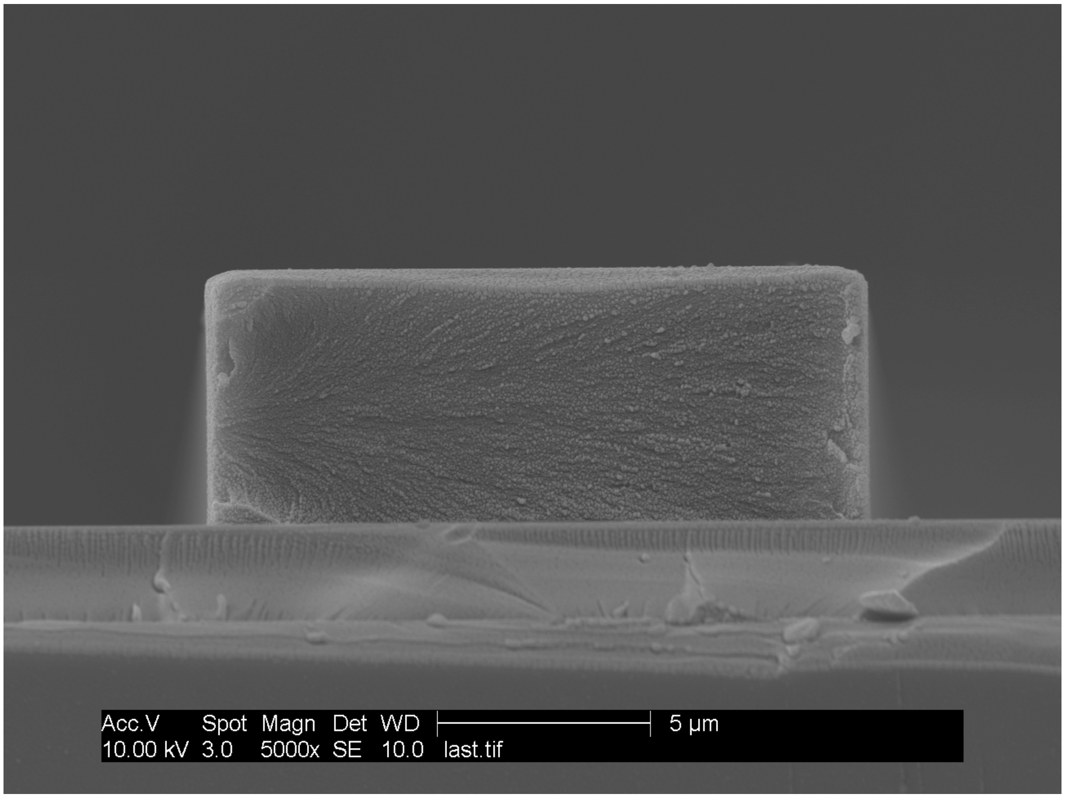

Figure 5.2 - SEM image of patterned SU-8 showing excellent smoothness and rectangular cross-section.

5.3 Core Removal

Due to the highly cross-linked nature of patterned SU-8, it is resistant to most chemicals [103]. This limits the options available for core removal. A solution of sulfuric acid and hydrogen peroxide, commonly known as piranha etch, was found to be the most practical way to remove cross-linked SU-8 from the waveguide structure, although another method discussed in [105] has not been explored. Piranha etch is commonly prepared as a 3:1 solution of concentrated sulfuric acid (H_2SO_4) and 30% hydrogen peroxide (H_2O_2). Upon mixing, the solution self-heats to approximately 100°C and begins to bubble due to evolution of oxygen gas. Piranha is highly effective in removing organic materials due to the dehydrating effect of concentrated sulfuric acid, followed by oxidation of carbon residue by atomic oxygen from the hydrogen peroxide.

The main drawback of piranha etch is that the hydrogen peroxide breaks down rapidly into water and oxygen gas. Under typical process conditions, the effectiveness of the solution begins to degrade in approximately 30 minutes. Unfortunately, the solution cannot simply be recharged by the addition of more hydrogen peroxide because the water formed from its decomposition will dilute the sulfuric acid, significantly reducing its effectiveness. Thus, to minimize the long etch time of the waveguides, the solution must be changed very frequently, resulting in high chemical usage and an unreasonable amount of labor.

One proposed method to eliminate the need to change the piranha etch solution is to use ammonium persulfate, $(NH_4)_2S_2O_8$, as the oxidizer in place of hydrogen peroxide [106]. Ammonium persulfate breaks down in the piranha solution to form sulfuric acid. Therefore, excess oxidizer can be added without diluting the solution. In practice, the ammonium persulfate-based piranha etch was found to have a slower etch rate than standard piranha etch, rendering it unsuitable for hollow waveguide fabrication which requires several weeks of etching.

A commercially available piranha etch solution known as Nano-Strip, produced by Cyantek Corporation, is sold as a pre-mixed, stabilized solution of sulfuric acid and hydrogen peroxide. This solution retains its reactivity significantly longer than standard piranha etch [107]. For example, at 60°C, Nano-Strip will maintain 85% of its etching effectiveness for 24 hours. Thus, the solution does not need to be changed as often as piranha etch, significantly reducing chemical usage and labor.

To characterize the etch process for the SU-8 core, we fabricated test structures using SU-8 cores and PECVD oxide coatings. These structures were then cleaved and placed in Nano-Strip for varying times at 50 and 60°C. The amount of SU-8 etched was then measured with an optical microscope. The results of this experiment are shown in Figure 5.3.

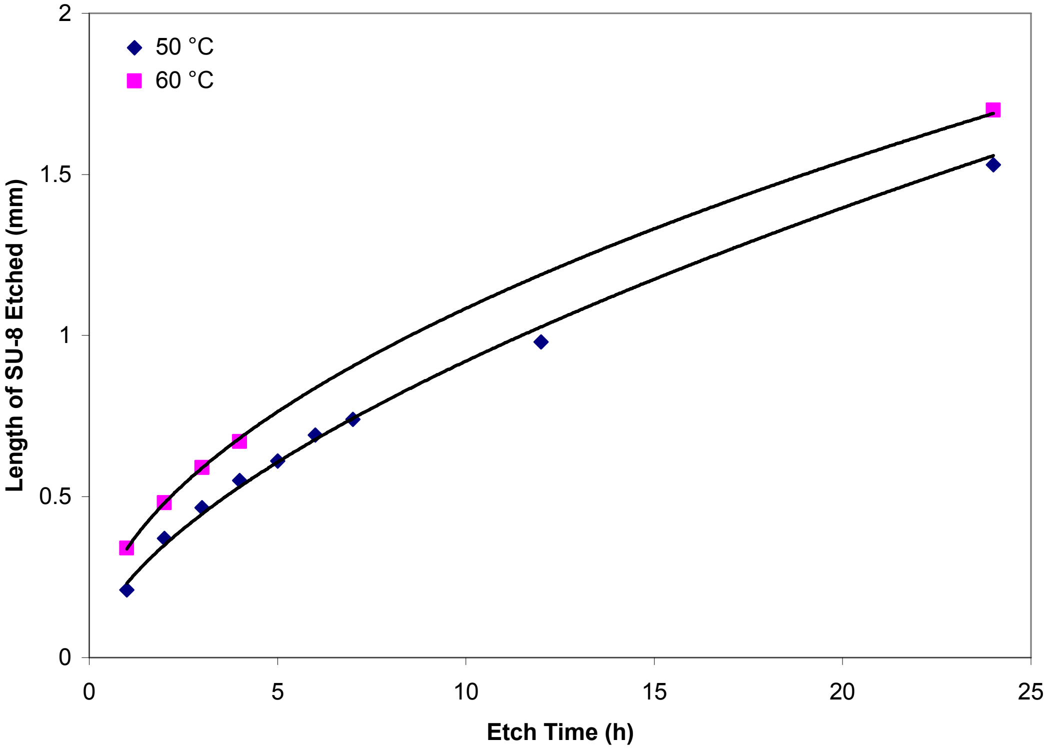

Figure 5.3 - Length of SU-8 etched from hollow channels as a function of time. Fitted curves have a square-root time dependency.

Like the aluminum etching described in Chapter 4, the process is seen to be diffusion-limited. Curves were fit to the data with a square-root time dependency. The etch rate for SU-8 is lower than the aluminum etch rate, showing a maximum of 1.7 mm etched in the first 24 hours. This is likely due to the high viscosity of the Nano-Strip solution, meaning a small diffusion constant for the etch and hence slow etch times. As with the aluminum etching process, raising the temperature of the etch solution will increase the etch rate, but we have found that waveguide breakage is excessive above 70°C. In practice, the SU-8 etch takes place at a solution temperature of 55°C.

Figure 5.4 shows an SEM image of a completed hollow waveguide fabricated using SU-8 as the sacrificial core. The rectangular cross-section is characteristic of this core material. Unlike the aluminum-based process, the completed waveguide shows no roughness. The alternating oxide and nitride layers are visible as light and dark bands surrounding the core.

5.4 Mechanical Strength

In order to characterize the mechanical strength of waveguides fabricated using SU-8, we fabricated test structures using a single top oxide layer with varying thickness over SU-8 cores with a height of 3.5 μm. These structures were then etched in Nano-Strip at 60°C and the integrity of the resulting hollow channels was determined by inspection with an optical microscope. The results of this experiment for four coating thicknesses are shown in Figure 5.5. This graph indicates the percentage of the channel that remained intact after the etch process. As with the aluminum-core channels, for a given top coating thickness, the channels are intact below a critical width. Above this width, the amount of breakage increases dramatically.

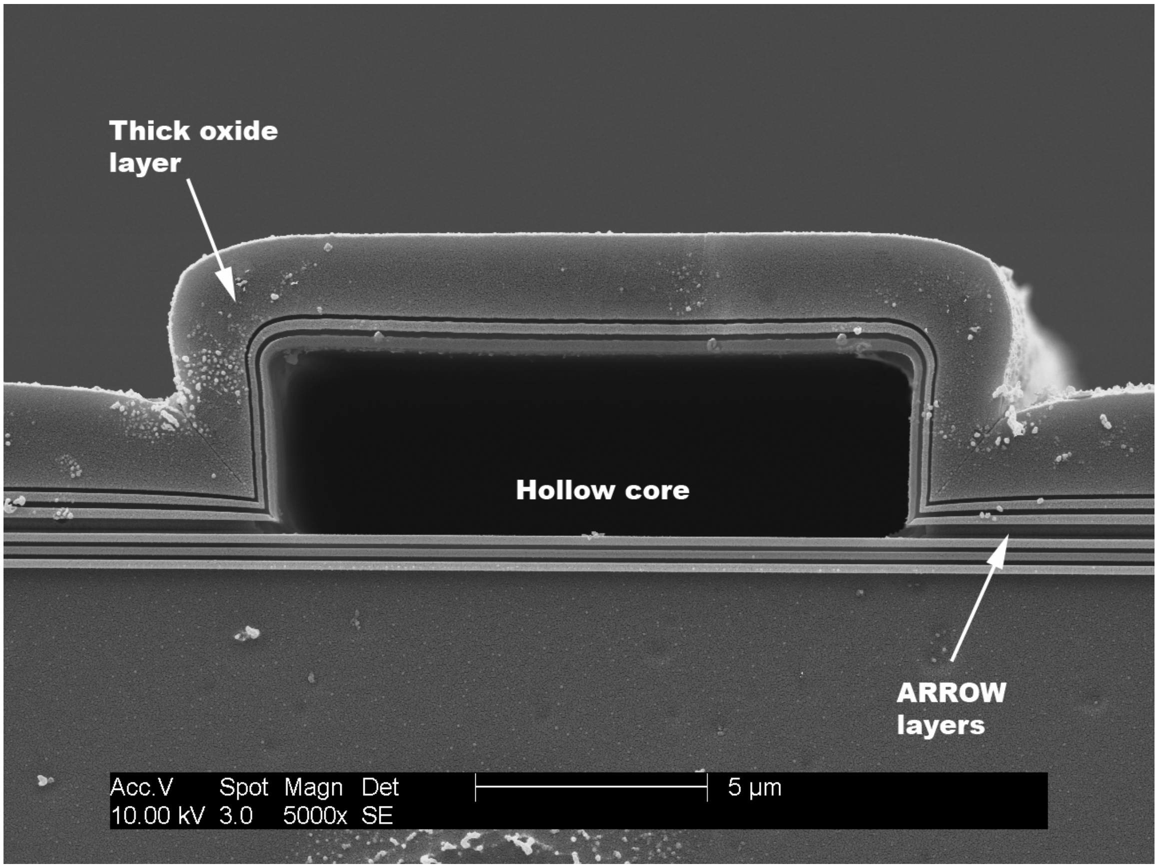

Figure 5.4 - SEM image of a hollow ARROW waveguide fabricated with an SU-8 core.

The data suggests a design rule that the waveguides be no wider than 10 times the upper layer thickness. This is substantially less than the 35:1 ratio for aluminum-core devices. The probable cause for this discrepancy is likely due to small cracks at the base of the waveguide extending out from the bottom corners. These cracks are discontinuities in the deposited film, caused by the PECVD process and the sharp angle of the core-substrate geometry. Although not present in every waveguide, the cracks substantially weaken the top of the structure, allowing it to easily separate from the rest of the wafer.

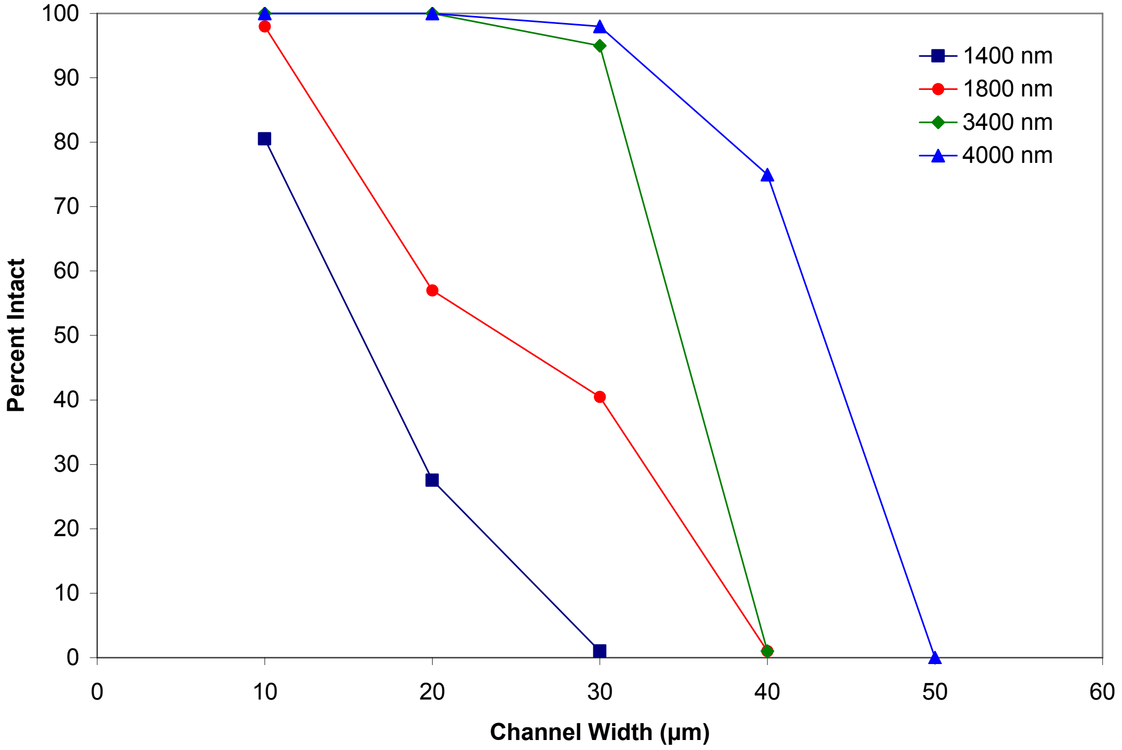

Figure 5.5 - Integrity of SU-8 based channels as a function of core width for coating thicknesses of 1400, 1800, 3400 and 4000 nm.

5.5 Optical Results

5.5.1 First Generation Waveguides

The first successful hollow ARROW waveguides were fabricated using the SU-8 process described above, with a core height of 3.5 μm. The dielectric layer thicknesses to fulfill the ARROW condition for an air-filled core at a wavelength of 785 nm are 109 nm for nitride (n=2.10) and 184 nm for oxide (n=1.46). These waveguides had three layer pairs in each direction from the core. The final oxide layer was 2.944 μm thick to provide increased mechanical strength while still acting as an antiresonant layer. An SEM image of this device is shown in Figure 5.6. This device has a core width of 12 μm and a small ridge etched into the top oxide layer to investigate the possibility of improved lateral optical confinement.

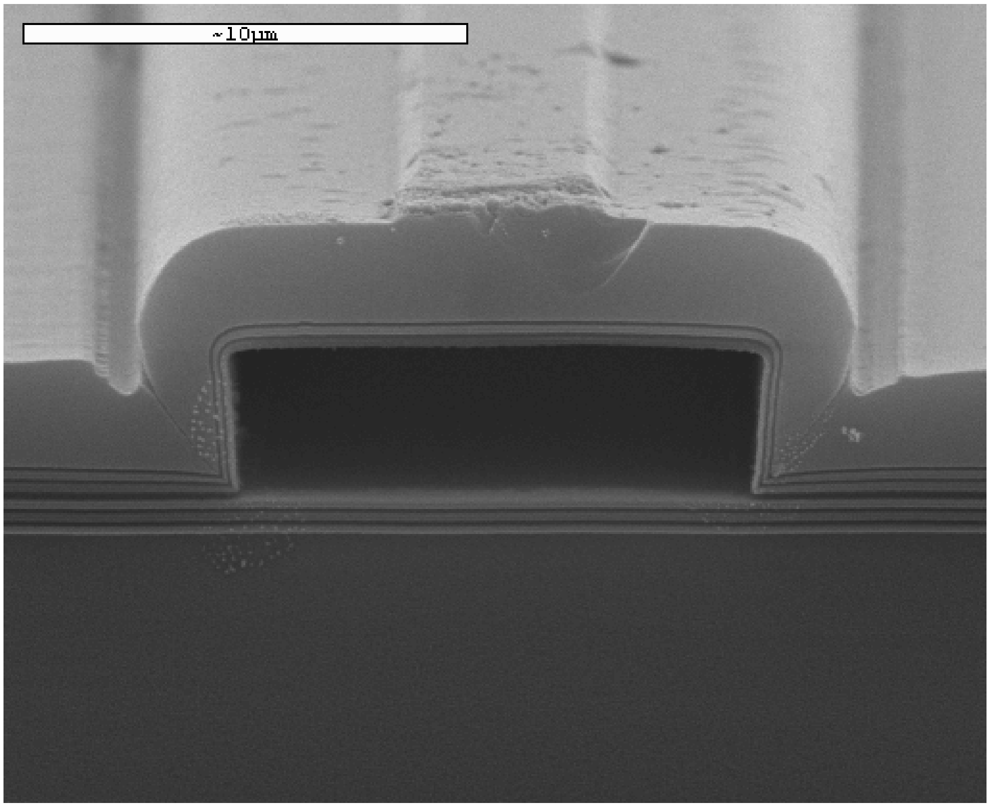

Figure 5.6 - SEM image of a hollow ARROW waveguide used for optical testing. The oxide and nitride layers are visible as light and dark bands.

A diagram of the test setup used to characterize these waveguides is shown in Figure 5.7. Light from a diode laser operating at 785 nm was coupled into the waveguide using an optical fiber. The near-field image of the mode profile at the output facet was taken using magnifying optics and a CCD camera. An image of the output facet of the ARROW waveguide is shown in Figure 5.8, with an outline of the sample added for clarity. Loss measurements were performed using the cutback method. Using this technique, the measured output power from waveguides of various lengths is plotted on a log scale as shown in Figure 5.9. A linear fit to the data gives the loss coefficient α in (2.8) The data shown are from waveguides with a width of 24 μm, and the calculated loss coefficient is 6.5 cm^{-1} [30].

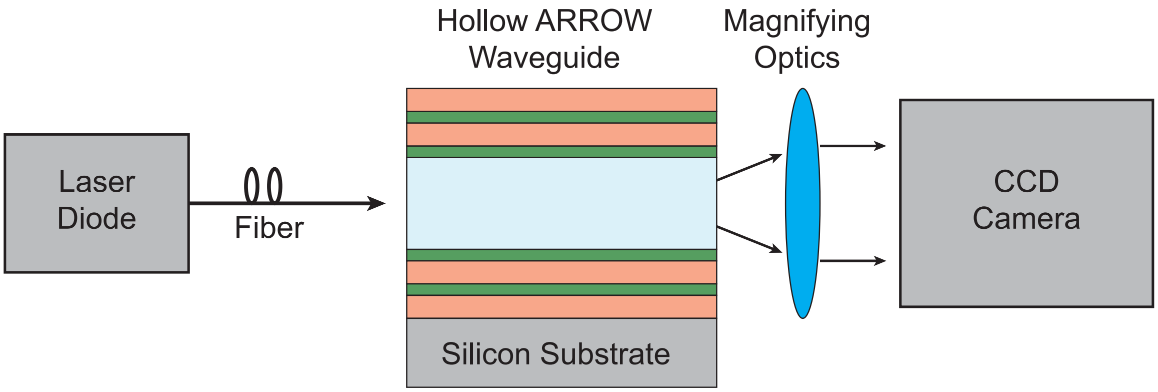

Figure 5.7 - Test setup for optical measurements of hollow ARROW waveguides.

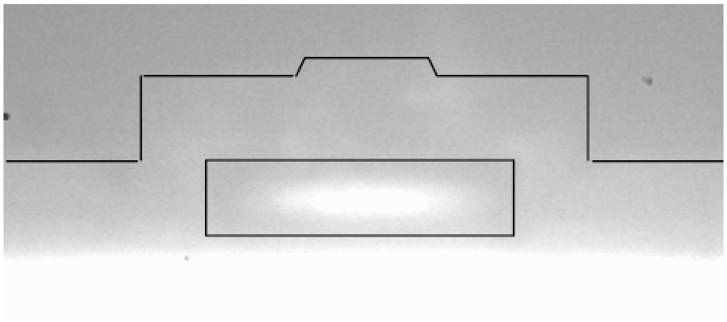

Figure 5.8 - CCD image of optical output from a hollow ARROW waveguide showing confinement in the core. An outline of the waveguide is added for clarity.

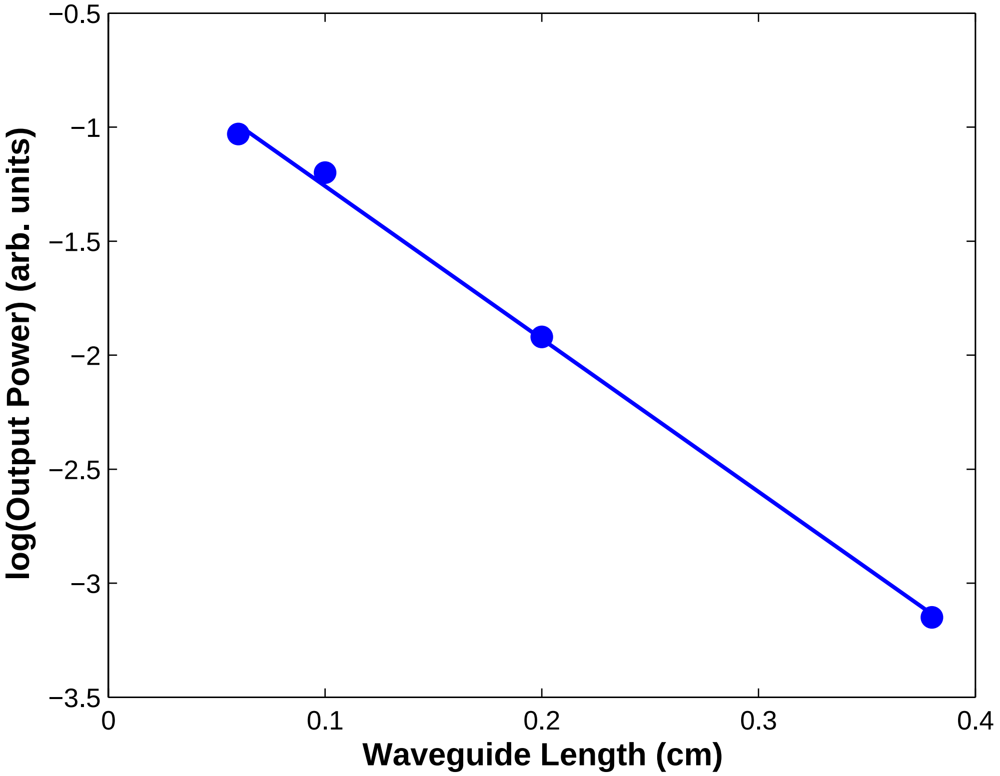

Figure 5.9 - Loss measurements for a 24 µm wide air-core ARROW waveguide. Circles are measured values; solid line is a linear fit to the data. Y-axis is the log of the measured output power.

Although designed for an air-filled core and 785 nm operating wavelength, these devices were also expected to exhibit low loss at 633 nm when filled with water (n=1.33) or ethylene glycol (n=1.43), showing the latitude of the ARROW design. Ethylene glycol was used to test the waveguides because it evaporates much more slowly than water, allowing for longer measurement times. Using the same test method as for air-core operation, a loss of 2.4 cm^{-1} was observed when operating at 633 nm, while no propagation was detected at 785 nm, implying that the loss at this wavelength was greater than 10 cm^{-1} [29].

5.5.2 Second Generation Devices

A second generation ARROW device intended for both air and liquid-core propagation was then fabricated. The design for these devices took into account the unequal growth rate of PECVD films deposited on the top and sides of the core. The bottom layer thicknesses were 126 nm (nitride, n = 2.05) and 326 nm (oxide, n = 1.46). From SEM images, we determined the ratio of the top layer thickness to the side layer thickness to be 1.26. As discussed in Chapter 2, waveguide loss for our devices is dominated by the lateral loss because the TM polarization is much lossier than the TE polarization. Therefore, the upper layers were grown 1.26x thicker than the calculated ARROW layer thickness, giving the correct thickness on the sides of the device. The layer structure of these devices is shown in Table 5.1.

Table 5.1 - Layer structure for improved liquid-core ARROW design with compensation for side thickness variation.

Specifications		Layer Structure	
		Layer	Thickness (nm)
Wavelength	633-785 nm	Oxide 6	1956
Core	Liquid	Nitride 6	159
Core Shape	Rectangle	Oxide 5	411
Nitride Index	2.05	Nitride 5	159
		Oxide 4	411
Second-generation liquid-core design with upper layer thickness compensation.		Nitride 4	159
		Core	3.5 μm
		Nitride 3	126
		Oxide 3	326
		Nitride 2	126
		Oxide 2	326
		Nitride 1	126
		Oxide 1	326
		Substrate	-

Loss measurements on these devices show a much lower loss, down to 0.33 cm^{-1} for 15 μm wide waveguides [24]. Figure 5.10 shows loss results for first and second generation ARROW waveguides with ethylene glycol cores, along with simulation results for comparison. These simulations were performed at UCSC and account for coupling into higher-order modes, which have much higher loss than the fundamental mode.

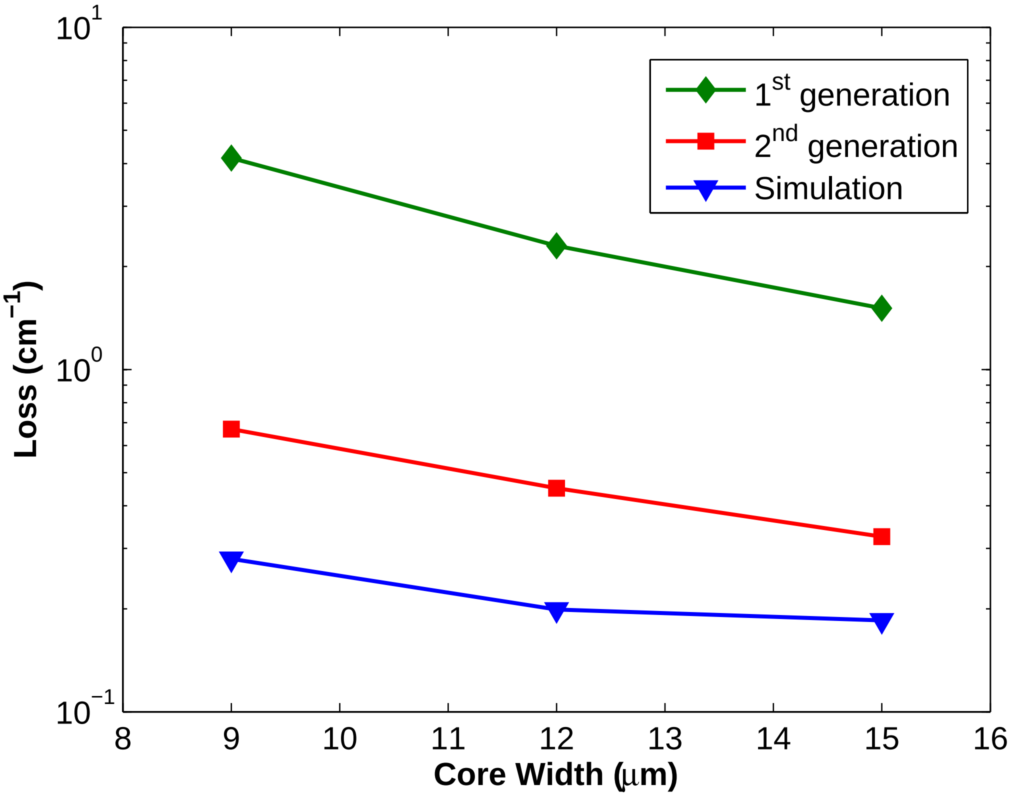

Figure 5.10 - Waveguide loss vs. core width of ethylene glycol core ARROW waveguide for first and second generation devices, compared to simulation results.

6 Photoresist Sacrificial Core

6.1 Introduction

Despite the successful fabrication of SU-8 based waveguides, a number of problems remained with the fabrication process and the resulting devices. As discussed in the previous chapter, the non-conformal PECVD deposition process results in waveguides with differing dielectric layer thicknesses on the sides and top. Although this effect can be compensated for in the design of the waveguide, ideally the film thickness would be uniform throughout the device. Additionally, the cracking seen at the base of the waveguides is a major source of structural failure. The slow etch rate of SU-8 compared to aluminum was considered to be an area where the fabrication process could be improved. The other major consideration for developing a fabrication process based on another core material was the possibility of producing waveguides with a different core geometry and better optical loss characteristics than the rectangular (SU-8) and trapezoidal (aluminum) geometries available previously.

This chapter describes the development of a positive photoresist based fabrication process. Like the previous chapters, details of the fabrication process are discussed. Studies of mechanical strength were undertaken, and are described here, as well as the core etch rates of these devices. Finally, optical measurements of waveguides fabricated using this process are given.

6.2 Fabrication Process

The photoresist-based process described here uses AZ 3330 photoresist, manufactured by AZ Electronic Materials. AZ 3330 is a broad-band general-purpose photoresist used extensively in the BYU IML. Like the SU-8 based process, the photoresist-based process has the key advantage of a directly patterned core, simplifying fabrication and giving a smooth surface suitable for optical waveguiding.

To process AZ 3330, a dehydration bake is performed by placing the wafer on a hotplate at 200°C for 10 minutes. The wafer is then placed on a spinner and an adhesion promoter, HMDS, is applied and spun on at 3000 rpm. Approximately 10 ml of photoresist is then applied and the wafer is spun for 60 seconds at 750 rpm. The wafer is then baked on a hotplate at 90°C for 60 s to evaporate excess solvent. The wafer is then exposed for 22 seconds in the MA-150 aligner using an appropriate mask. The resist is developed for 135 seconds in AZ 300 MIF developer, also from AZ Electronic Materials. The height of the patterned resist is 5.8 μm for a spin speed of 1000 rpm.

6.2.1 Photoresist Reflow

Due to the non-cross-linked chemical structure of positive photoresist, it is subject to reflow upon heating. Reflow occurs as the photoresist is heated above its melting point, upon which surface tension draws the photoresist into a rounded shape. The reflow characteristics of photoresist have been investigated and used to fabricate integrated optical elements such as microlenses [108].

To characterize the reflow process for use in the fabrication of hollow waveguides, we carried out studies of the change in shape experienced by AZ 3330 photoresist upon heating to 250°C for 10 minutes [21]. Samples were patterned and cleaved, and then SEM images were taken of the reflowed resist and compared to unheated samples. The reflowed resist was found to take on a shape dependent on its initial width, as shown in Figure 6.1. Resist lines with a width greater than the original height assumed a shape described by a portion of a cylinder, while narrower lines were shaped like a half ellipse. The cross-sectional area of these shapes is given by:

$$A_{cyl} = R^2 \sin^{-1}\left(\frac{r}{R}\right) - r(R-h), \qquad for \quad r > h, \text{ and} \tag{6.1}$$

$$A_{ellip} = \frac{\pi xy}{2}, \qquad for \quad r < h, \tag{6.2}$$

with r, R, x, and y as shown in Figure 6.1.

These equations were then used to determine the final dimensions of the photoresist lines by using SEM images to measure the change in width and cross-sectional area of the photoresist upon reflow. Figure 6.2 (a) shows a plot of the width pre- and post-reflow of photoresist lines of varying widths. The fit curve has a 45° slope, indicating that the width of the lines does not change during reflow. Figure 6.2 (b) shows the change in cross-sectional area of the photoresist lines. The fit curve indicates a final area 0.80 times the original area. The change in area is due to evaporation of solvents in the photoresist and has been reported previously [109].

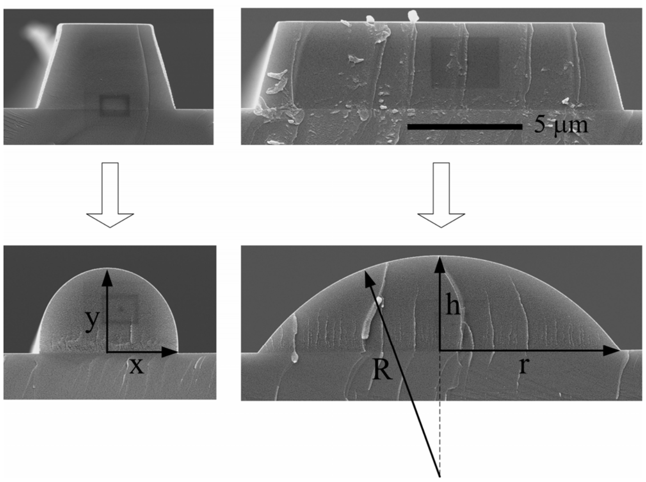

(a) **(b)**

Figure 6.1 - SEM images of photoresist lines before and after reflow, illustrating the geometry of the reflowed lines. An elliptical cross-section is obtained with narrow lines as in (a), while a cylindrical shape results from wide lines (b).

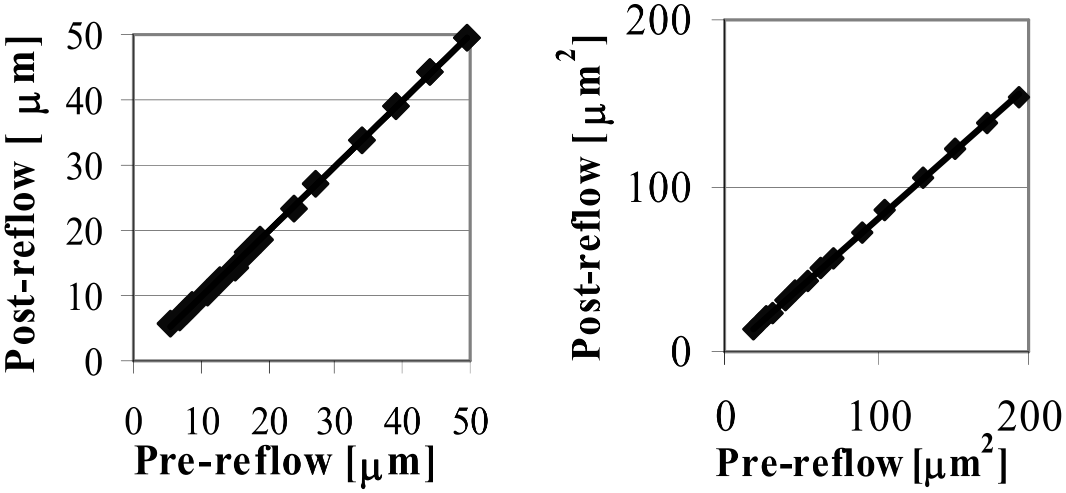

(a) **(b)**

Figure 6.2 - Comparison of cross-sectional parameters of photoresist before and after reflow. (a) Width of photoresist lines measured at the bottom of the resist. (b) Cross sectional area.

Using the constraints of no width change and area reduction by *0.80x*, (6.1) and (6.2) can be used to predict the final cross-section of the photoresist, and hence the hollow waveguide core. A plot of measured height vs. width of reflowed photoresist is shown in Figure 6.3, along with the calculated values described above. The fit is very good for lines below 25 μm wide, indicating that the predictions made using (6.1) and (6.2) are accurate. Above 25 μm, however, the resist does not reflow into a cylindrical shape, but stays flat across most of its width with rounded edges. The widths of the waveguides discussed in this dissertation range from 9 to 15 μm, well within the range covered by the predictive model. Due to the round shape of the photoresist core, PECVD films have very uniform thicknesses compared to films deposited on SU-8 cores. Therefore, the top layers do not require compensation for unequal side and top dielectric layer thicknesses, simplifying the waveguide design.

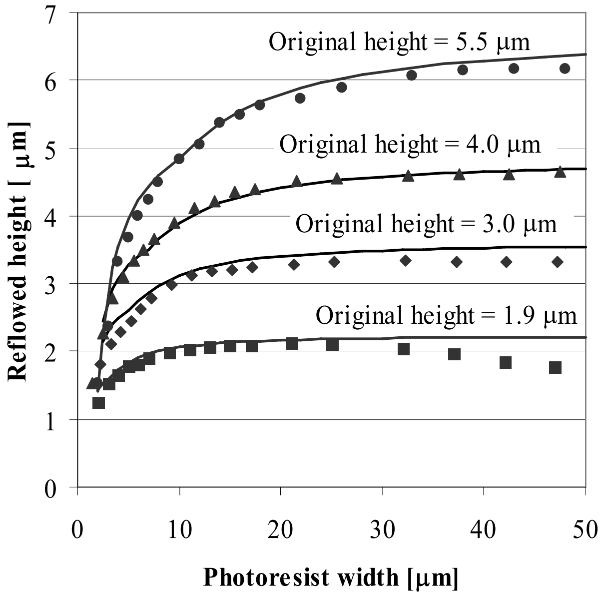

Figure 6.3 - Height of reflowed photoresist versus line width for several initial heights. Solid lines represent theoretical predictions.

6.2.2 Etching

Although positive photoresist is much less chemically resistant than SU-8 and could therefore be expected to etch more quickly, we found that the etch rate in Nano-Strip was comparable to the SU-8 etch rate. This is due to resist hardening during the reflow process and PECVD deposition. Additionally, common removal methods for photoresist such as acetone or other solvents do not remove the hardened photoresist. Therefore, although the reflowed photoresist process allows for a different core geometry, by itself it does not allow for decreased fabrication time.

6.2.3 Hybrid Core

An ideal sacrificial core would combine the fast etching time of aluminum with the smooth surface and round shape of photoresist. A hybrid core design consisting of a layer of aluminum covered by reflowed photoresist achieves this design goal. To produce a hybrid core, 200 nm of aluminum is deposited on the wafer by thermal evaporation. Photoresist is then applied and patterned using the standard process, followed by an oxygen plasma descum step to remove any residue. The aluminum is etched in a commercial etch solution, leaving metal lines underneath the photoresist. After etching the aluminum, the photoresist is reflowed at 250°C for 10 minutes, at which point the wafer is ready for the top layers to be deposited in the PECVD.

The etching process for the hybrid core design takes place in 2 steps. First, an *aqua regia* solution is used to remove the aluminum layer. Aluminum etch rates are comparable to those described in Chapter 4. After the channel has been cleared of aluminum, the devices are then placed in Nano-Strip to remove the photoresist. Because there is a hollow channel running the length of the device, the photoresist etch proceeds much faster than for a structure etched from the ends only. This is due to improved circulation of the etchant through the channel. The photoresist etch takes approximately 1 hour, so the total etch time is dominated by the aluminum etch [19].

Figure 6.4 shows a completed ARROW waveguide fabricated using this process. The rounded core is visible, demonstrating the shape and excellent smoothness attainable with photoresist cores. The upper dielectric layers of the waveguide show good thickness uniformity across the entire span.

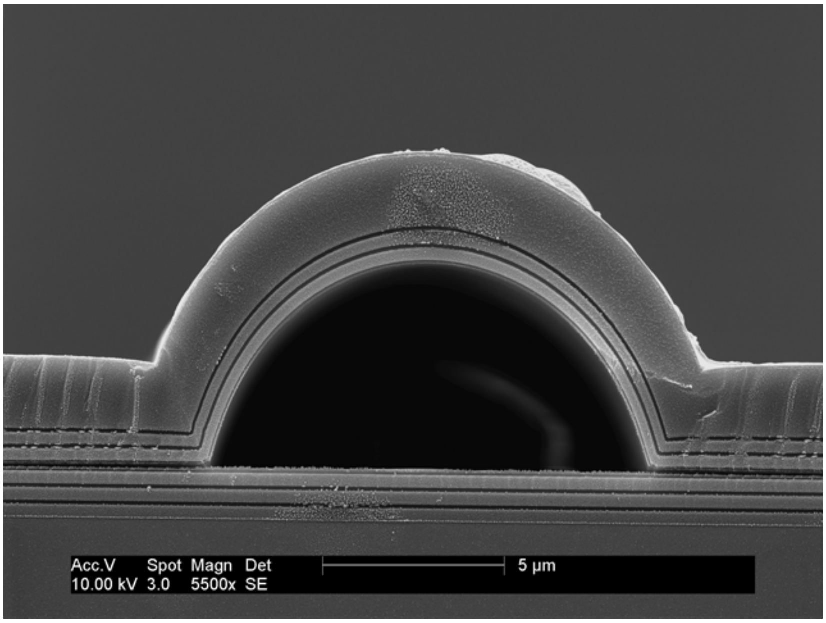

Figure 6.4 - SEM image of an ARROW waveguide fabricated with a photoresist sacrificial core. Alternating oxide and nitride layers are visible as light and dark bands.

6.3 Mechanical Strength

Due to the arched shape of the waveguides and the absence of sharp corners which lead to cracking of the SU-8 based waveguides, it was expected that the photoresist-based devices would have greatly increased mechanical strength. To verify this, an experiment similar to those described in Chapters 4 and 5 was carried out using photoresist cores. The top oxide layer ranged from 500 to 2700 nm thick. After removing the cores with an *aqua regia* solution at 60°C and then Nano-Strip at 60°C, the structures were inspected with an optical microscope for mechanical integrity. The results are plotted in Figure 6.5, showing that like the other structures, there is a critical width above which the structures will fail. The results indicate a design rule of a width to thickness ratio of 50. This compares very favorably to the values for SU-8 (10:1) and aluminum (35:1).

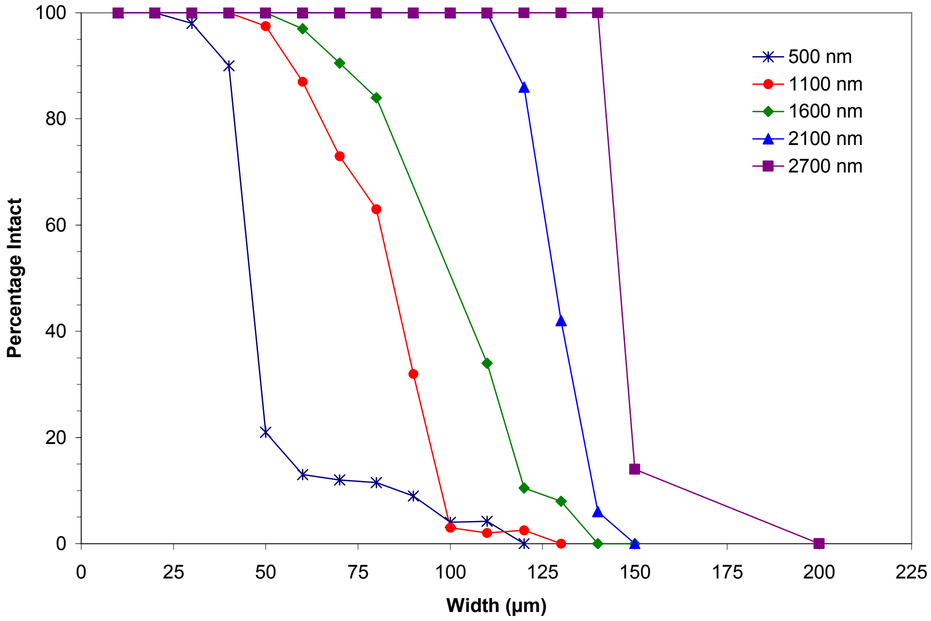

Figure 6.5 - Mechanical integrity of arch-shaped channels as a function of channel width for various coating thicknesses.

6.4 Optical Results

The waveguides fabricated using photoresist sacrificial cores were tested in the same manner as described in Chapter 5 for the SU-8 based devices. Light was coupled in from an optical fiber, and the output from the waveguide measured using imaging optics and a CCD camera. An image of the mode profile is shown in Figure 6.6. This device had a core height of 4 μm and base width of 9 μm. The observed mode is more circular than the modes observed in rectangular-core devices, as expected. Figure 6.7 shows experimental values for transmission vs. length for ARROWs with three different widths. The fitted lines give the waveguide loss, which for the 15 μm wide waveguides was 0.26 cm^{-1}, the lowest observed loss in a liquid-core ARROW to date [22].

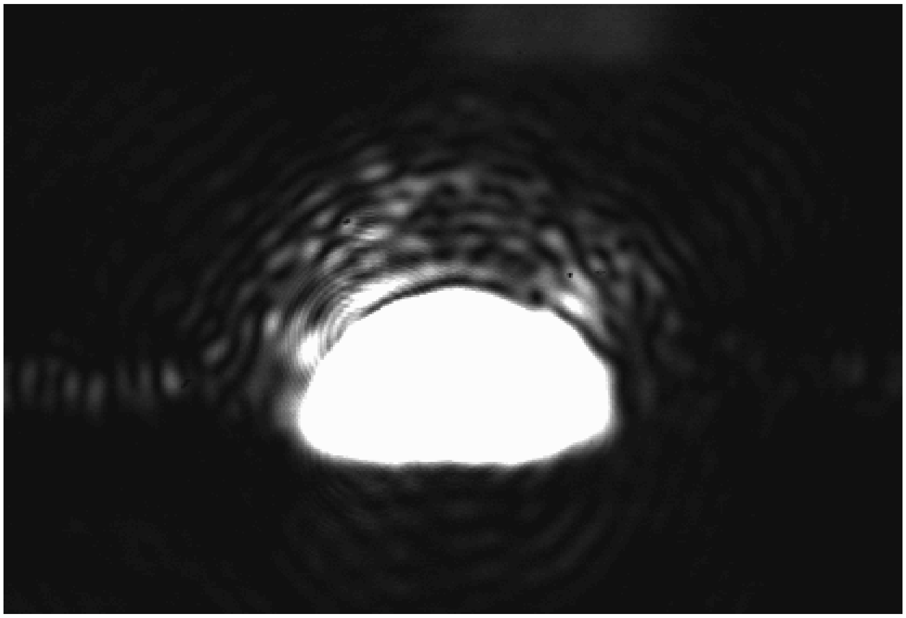

Figure 6.6 - Mode image of a photoresist-based hollow ARROW waveguide.

The optical loss performance of both rectangular and arched core ARROW waveguides is shown in Figure 6.8, plotted by mode area rather than core width. As expected, the loss increases as the mode area, determined by the core size, becomes smaller. The arch-shaped ARROWs exhibit lower loss than the rectangular waveguides, largely due to the uniform upper dielectric layers. The open shapes represent simulated loss values performed using FIMMWAVE™ software (Photon Design, Ltd.). The discrepancy between simulated and measured loss values can be attributed to waveguide roughness and non-ideal dielectric layers, and indicates that improvement is possible in the fabrication process.

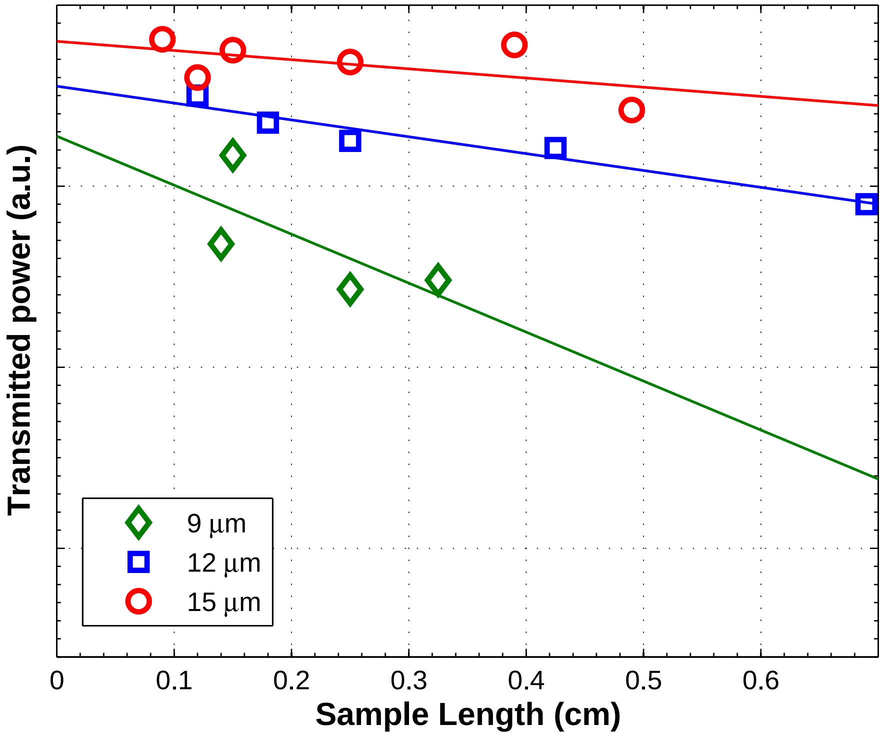

Figure 6.7 - Waveguide output power (log scale) vs. length for arched core hollow ARROW waveguides. Shapes are measured values, lines represent linear fit to data.

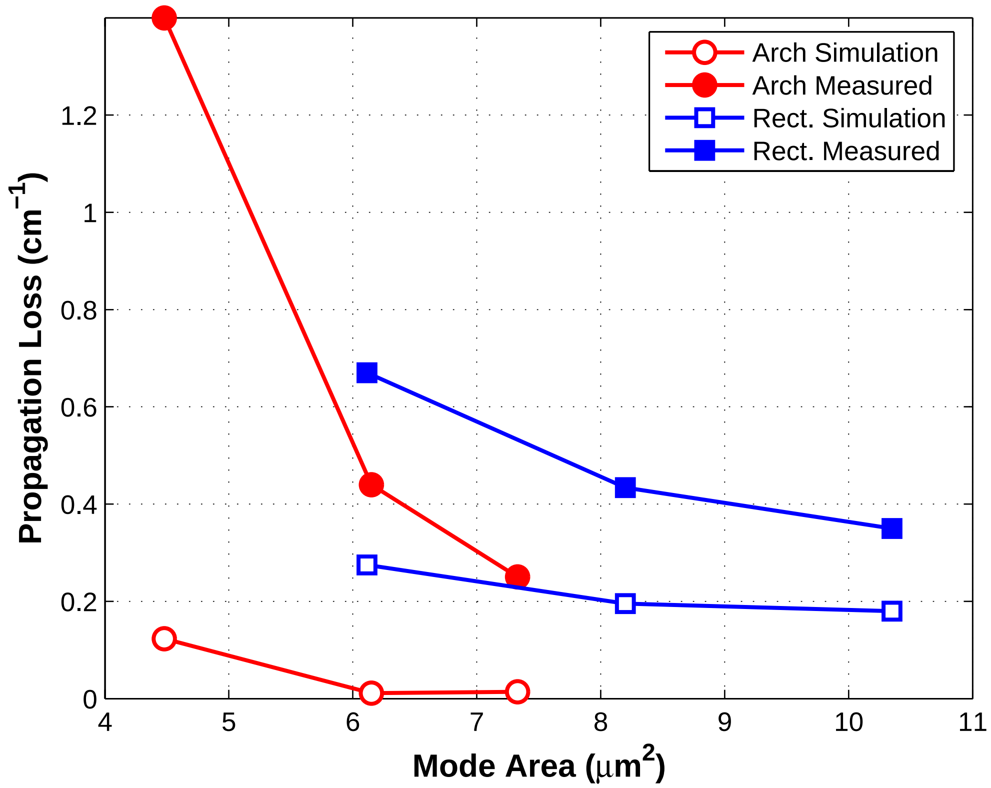

Figure 6.8 - Optical loss of rectangular and round (arch-shaped) ARROW waveguides. Solid shapes represent measured values, open shapes are theoretical values.

7 Advanced Waveguide Structures

7.1 Introduction

One of the key advantages of the hollow waveguide fabrication process described in the previous chapters is its planar nature. The waveguides are fabricated using a standard silicon wafer as a substrate. This allows for the simple fabrication of other structures along with the hollow ARROW waveguides. The integration of hollow ARROWs with solid-core waveguides and other systems is essential to the development of applications for these devices.

This chapter will discuss the fabrication of solid-core waveguides in conjunction with the hollow ARROW fabrication process described previously. Structures to facilitate integration of the hollow and solid-core waveguides such as intersections and corners are detailed. Additionally, the fabrication of hollow ARROW waveguides on top of raised silicon pedestals for improved loss characteristics is described.

7.2 Solid-core Waveguides

The hollow waveguides discussed in the previous chapters were tested by cleaving and coupling light into the core from an optical fiber. As noted earlier, liquids evaporate rapidly from the core, and filling such a device with gas or vapor would be difficult. To realize the potential of the hollow planar waveguide, a means must be devised to couple light into the waveguide while allowing the core to remain sealed off from the outside environment. Fortunately, the top oxide layer of the hollow ARROW waveguides provides a good platform for the fabrication of solid-core waveguides, which can be used for optical access to the hollow waveguides, as illustrated in Figure 1.2.

7.2.1 Fabrication Process

Solid-core waveguides fabricated in the top oxide layer of the ARROW layer stack rely on ARROW confinement on the bottom, while confinement on the top is by conventional index guiding at the oxide/air interface. A ridge etched into the oxide provides lateral confinement. The fabrication of this ridge is relatively simple and takes place after the ARROW layer deposition but before the core removal step. A photoresist pattern is created using standard photolithography processes, and the wafer is then placed in a reactive ion etcher (RIE) to create a ridge in the top oxide layer. This process is illustrated in Figure 7.1.

As described in Chapter 3, reactive ion etching is a dry etching process that uses a reactive plasma to remove material from the wafer. An anisotropic etch profile can be achieved due to the directional nature of the ion bombardment from the plasma, and the profile is dependent on the chamber pressure, RF power level, and the etch chemistry. The etch process used in the fabrication of the solid-core waveguides discussed here makes use of an Anelva DEM-451 reactive ion etcher. The etch takes place with a flow rate of 10.5 sccm of CF_4 gas at a pressure of 100 mTorr and 300 W of RF power, which etches PECVD oxide at approximately 110 nm/minute. The wafer is etched for 9 minutes 20 seconds for a target ridge height of 1 μm. Optical measurements of the loss of solid-core waveguides fabricated this way give a loss of 0.23 cm^{-1}, which is much higher than the calculated value of 10^{-4} cm^{-1} [25]. This discrepancy is largely due to sidewall roughness in the ridge structure, as seen in Figure 7.2, and could be reduced by use of an improved RIE etch process.

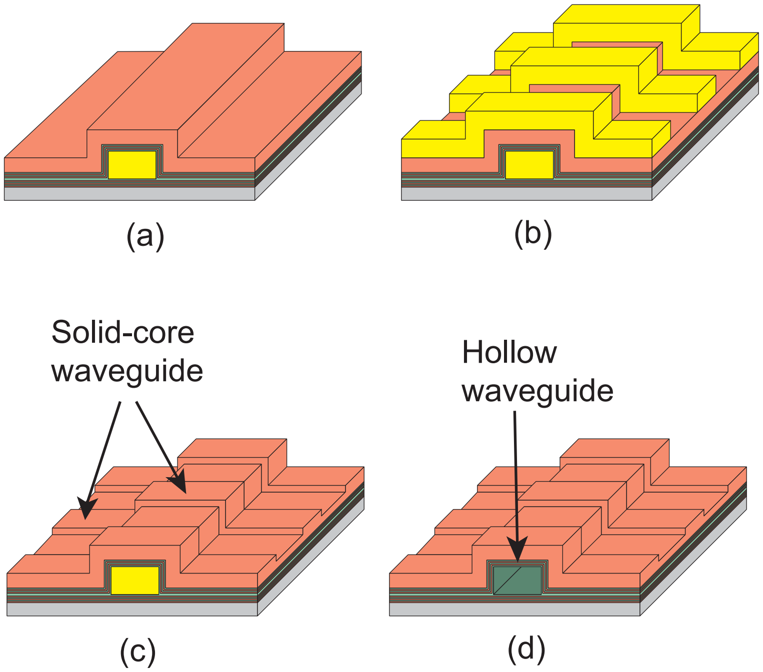

Figure 7.1 - Solid-core waveguide fabrication. (a) Standard hollow-core process with sacrificial core intact. (b) Ridge patterned and etched in top oxide layer. (c) Finished solid-core waveguide. (d) Core removed to form hollow-core waveguide.

7.2.2 Intersections and Hollow to Solid-core Transitions

The integration of hollow and solid-core waveguides requires two types of junctions: an intersection between a hollow and a solid-core waveguide and a transition between the two. Intersections allow for the optical excitation of a very small volume within the hollow ARROW, and represent one of the key advantages of the devices presented here. End transitions allow for optical access to light propagating in the hollow core, and permit the fabrication of bends or tees in the hollow waveguide to allow for interfacing the hollow channel with gas or liquid reservoirs or other systems.

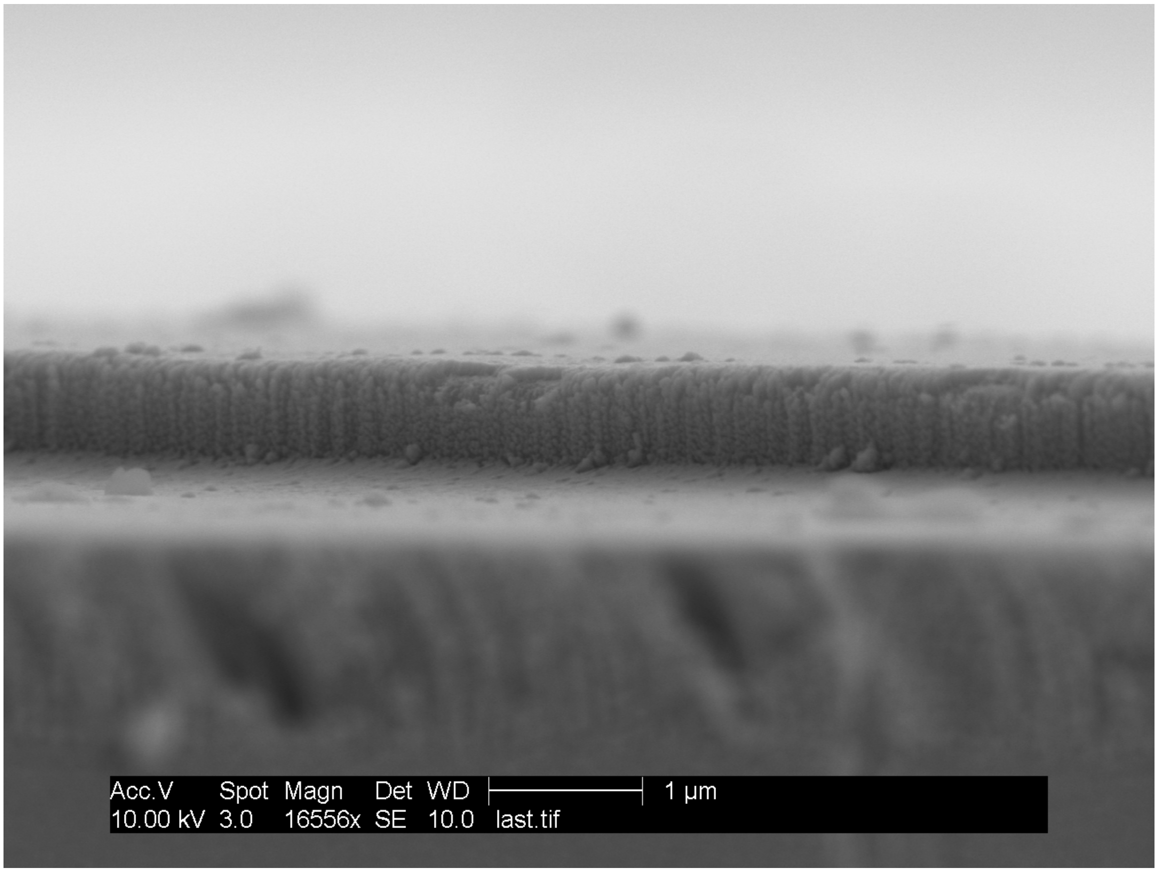

Figure 7.2 - SEM image of SiO_2 ridge, showing roughness of sidewalls.

The optical design of these junctions is involved and requires optimization of both solid and hollow-core waveguide loss as well as the optical transmission through the interface. Details of this design process are given in [25] and [42]. A basic design rule to ensure vertical alignment of the modes in the solid and hollow cores is illustrated in Figure 7.3.

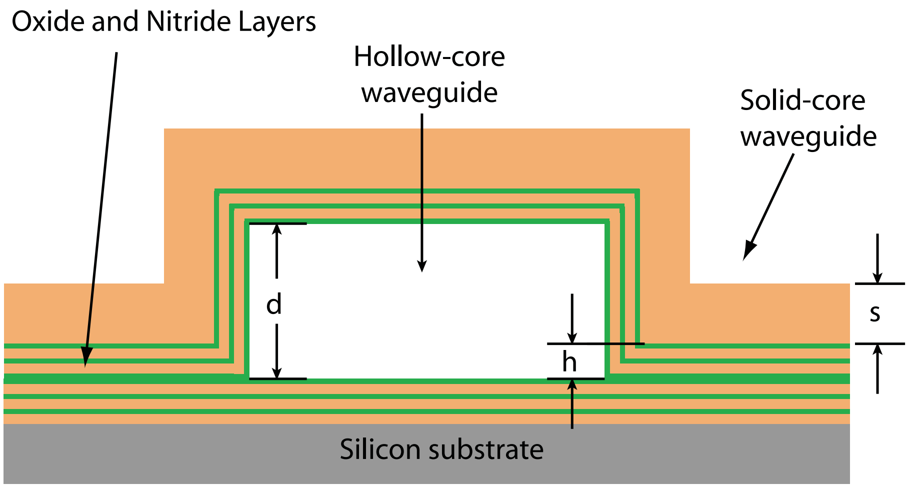

Figure 7.3 - Design of solid to hollow core junction to ensure vertical mode alignment .

In this diagram, *d* is the height of the hollow core and *s* is the thickness of the top oxide layer which forms the solid-core waveguide. The thickness of the upper dielectric layer stack (excluding the top oxide layer) is *h*. The modes will be approximately aligned in the vertical direction when:

$$s = d - 2h. \tag{7.1}$$

In practice, *s* should be chosen to satisfy (2.6) with a value approaching the condition shown in (7.1).

The fabrication of intersections and junctions requires careful mask alignment during the photolithography process to ensure accurate alignment of the waveguides. Misalignment could result in damage to the hollow-core waveguide structure due to unwanted etching of the top dielectric layers. Such etching will increase the optical loss and may result in leaks or breaks in the waveguide. Fortunately, the contact alignment process used in the BYU IML provides adequate performance if care is taken during the alignment step. Figure 7.4 shows an SEM image of an end-transition between a solid and a hollow-core waveguide, and Figure 7.5 shows an SEM image of a solid-hollow intersection fabricated as described above.

7.3 Corners and Tees

Successful application of the hollow ARROW waveguides discussed here requires interfacing to fluid reservoirs as well as solid-core waveguides. This interfacing makes use of corners and tees in the hollow waveguides. In practice, it was decided to add a small (20 μm) stub to corner junctions in order to move the corner away from the hollow-solid transition, as shown in Figure 7.6. This was due to concerns that the structure would have high loss at the junction, and that misalignment of the ridge etch mask could result in damage to the hollow waveguide from the RIE etch process. Thus, all of the junctions fabricated to date can be classified as tees. Because small air bubbles have been observed in fabricated junctions used with liquid cores, an improved design eliminating the stub should be investigated.

Another problem observed with fabrication of tee junctions is increased breakage of the upper dielectric layers at the tee. This is likely due to increased pressure during the sacrificial core etch. This pressure, caused by gas evolution from the etch solution, is increased by the higher cross-section of core material encountered by the etchant upon reaching the tee junction. Additionally, the structure of the tee may be mechanically weaker than a straight channel or corner, although this has not been confirmed by mechanical analysis.

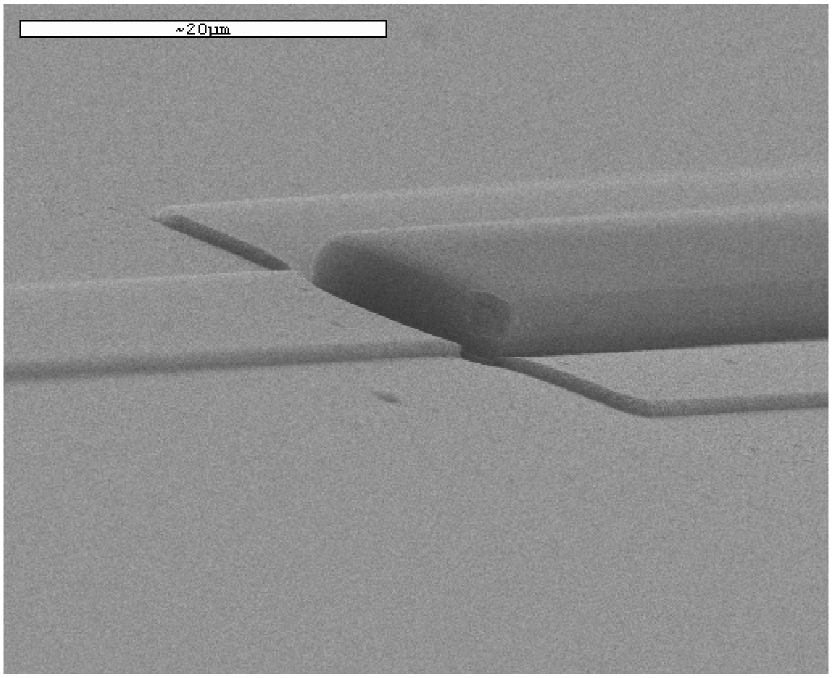

Figure 7.4 - SEM image of a transition from a solid-core waveguide (left) to a hollow core ARROW.

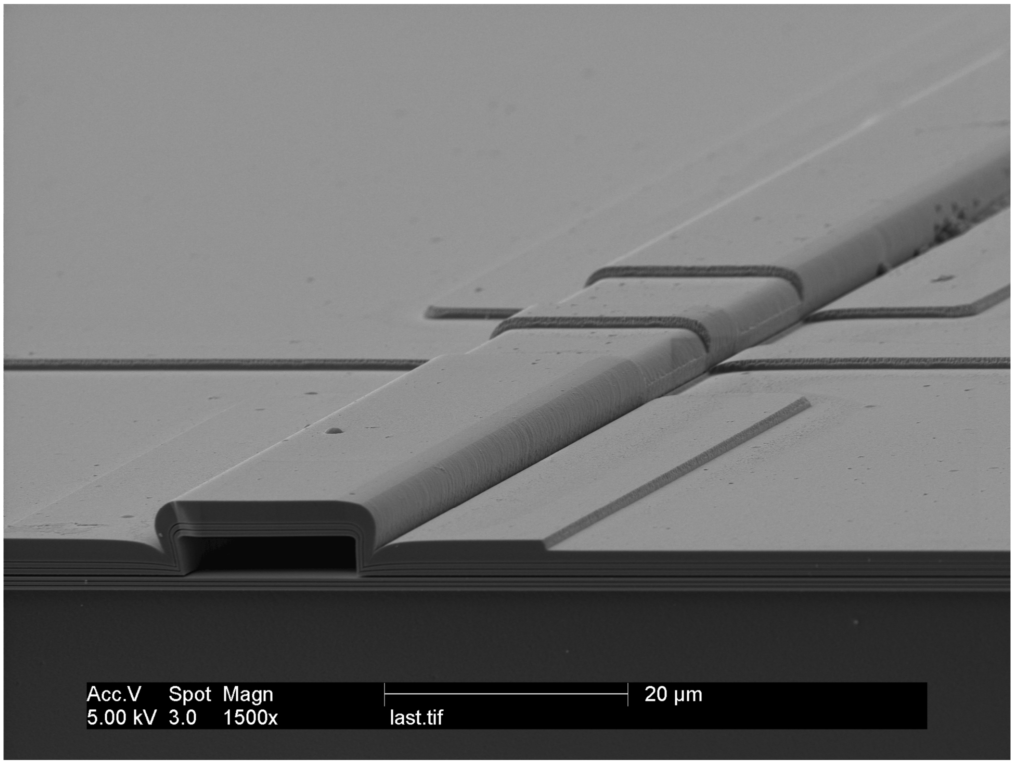

Figure 7.5 - SEM image of an intersection between a solid-core waveguide (running left to right) and a hollow-core ARROW waveguide.

7.4 Pedestal Process

One non-ideal aspect of the hollow ARROW fabrication process results from the final oxide layer. As shown in Figure 5.4, the thick upper oxide layer extends laterally out from the waveguide on both sides of the core. This high-index (relative to the hollow core) terminating layer results in much higher optical loss than if the final layer were air [23]. This effect is more pronounced in air-core devices compared to liquid cores. Consideration was given to etching the sides of the waveguide to create an air termination, but the mask alignment requirements would exceed the typical ± 1 μm alignment tolerance achievable with the equipment used in the IML.

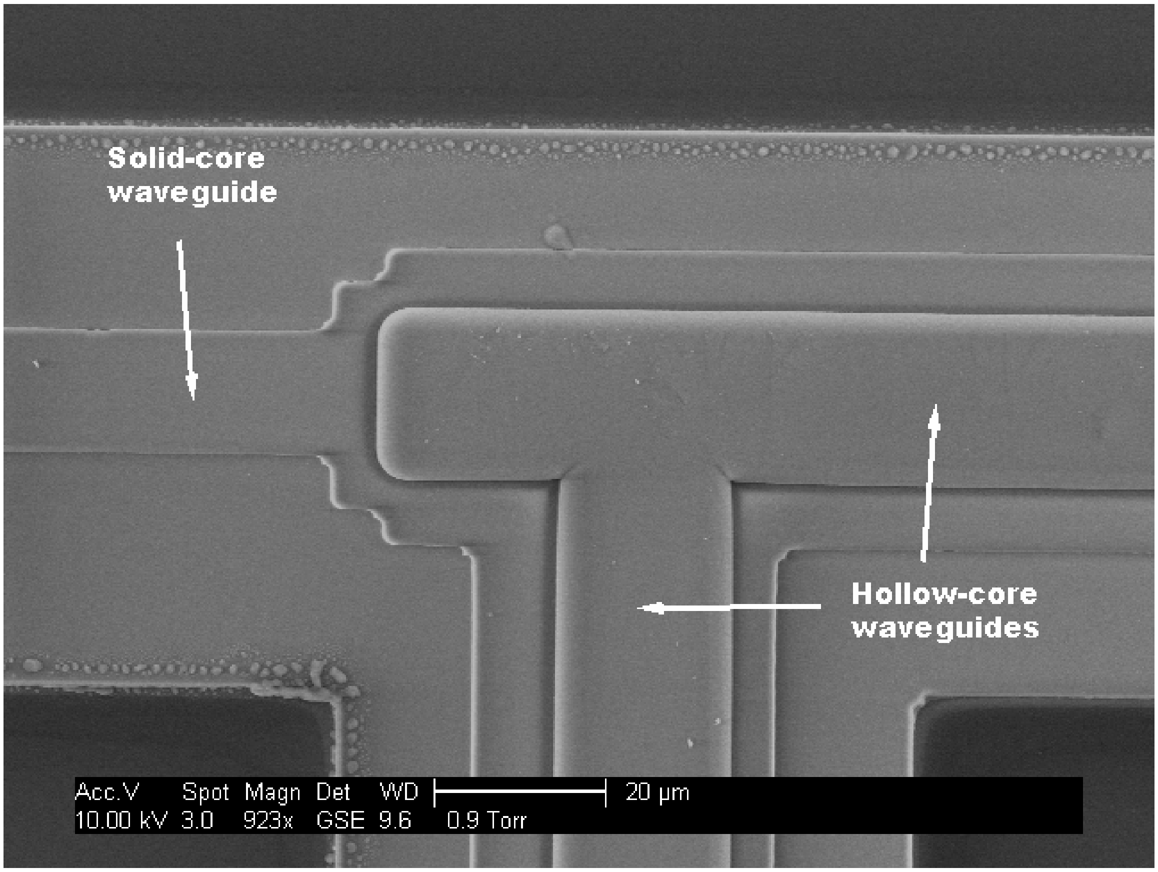

Figure 7.6 – SEM image of a 90° bend in a hollow ARROW waveguide. The bend has been moved back from the end to allow a better transition into the solid-core waveguide (left side).

An effective method to create waveguides with air terminating layers on the sides was developed using reactive ion etching to create a raised silicon pedestal before fabricating the waveguide, as illustrated in Figure 7.7. First, a thick layer of SU-8 is patterned on a bare silicon wafer. The viscosity used is SU-8 25, spun at 1800 rpm for a final thickness of 10 µm. After patterning and an oxygen plasma descum, the wafer is etched in the DEM-451 RIE for 35 minutes at 100 mTorr, 100 W RF power, and gas flows of 10.5 sccm CF_4 and 3.1 sccm O_2. The etch rate of silicon is approximately 130 nm/minute, giving a pedestal height of 4.5 µm. After the pedestal has been etched into the silicon surface, the SU-8 is removed by a 5 minute oxygen plasma descum, a 1 hour Nano-Strip etch, and a 1 minute BOE etch. At this point, the standard fabrication process is used to create hollow ARROW waveguides on top of the raised pedestals.

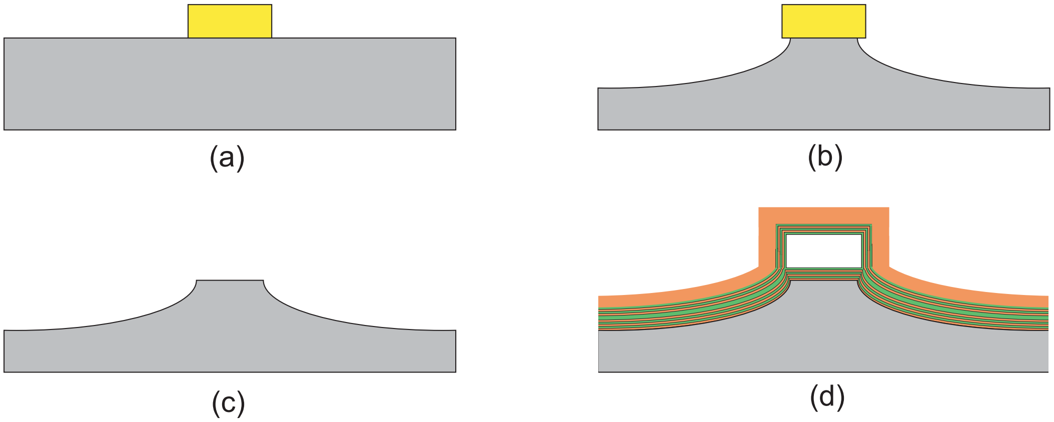

Figure 7.7 - Pedestal ARROW fabrication process. (a) Silicon substrate with photoresist. (b) Pedestal structure after RIE etch. (c) Raised silicon pedestal. (d) Hollow ARROW structure on raised pedestal.

This method has the additional benefit of eliminating the 90° corner where the SU-8 core meets the substrate, which is a major source of weakness in the standard SU-8 based waveguides. A similar technique to fabricate waveguides raised above the substrate is described in [110], although in this method the etch is performed after the bottom dielectric layer deposition.

The final dimensions of the raised silicon pedestal are critical to the pedestal fabrication process. The pedestal width is determined by the mask width, the degree of undercut during the RIE etch, and the thickness of the bottom dielectric layers. If the final pedestal width is too narrow, the sacrificial core will drop down on one or both sides of the pedestal, leading to misshapen waveguides and cracks or leaks in the device. If the pedestal is too wide, the side dielectric layers will exhibit the geometry shown in Figure 7.8. Although this device has air as the terminating layer on the waveguide sides, the final oxide layer thickness is not uniform along the height of the core, leading to increased loss compared to an ideal device. Additionally, the alignment of the core layer to the pedestal must be very precise to avoid problems similar to those caused by a narrow pedestal. The height of the pedestal must be great enough to ensure that the top of the final oxide layer remains below the level of the waveguide core, and it is also desirable to have a curved transition from the planar substrate to the vertical waveguide sidewalls in order to avoid structural weakness caused by sharp angles.

Unfortunately, the Anelva DEM-451 RIE etcher used for pedestal etching has proven to be marginally adequate for this process. The etch rate of silicon has been found to vary by as much as a factor of 2. This variation is likely due to the etch chamber condition, but has not been characterized or controlled to date. Because of the critical geometry requirements of the silicon pedestal, the significant etch rate variation results in very low yields for the pedestal etch process. In practice, the pedestal-based waveguides fabricated to date have used pedestals wider than the nominal thickness. An etch process with a stable etch rate and degree of anisotropy would significantly improve the pedestal fabrication process, but is unlikely to be achieved using the DEM-451 machine.

Optical tests of the pedestal-based ARROWs show significantly improved loss characteristics for air-core devices. As reported in [23], a loss coefficient of 2.6 cm^{-1} was measured in 15 μm wide devices. The loss in 9 μm wide waveguides was 6.8 cm^{-1}, a value comparable to the loss in a much wider 24 μm non-pedestal device reported earlier. Further improvement in the optical loss can be achieved by refining the pedestal etch process as discussed above.

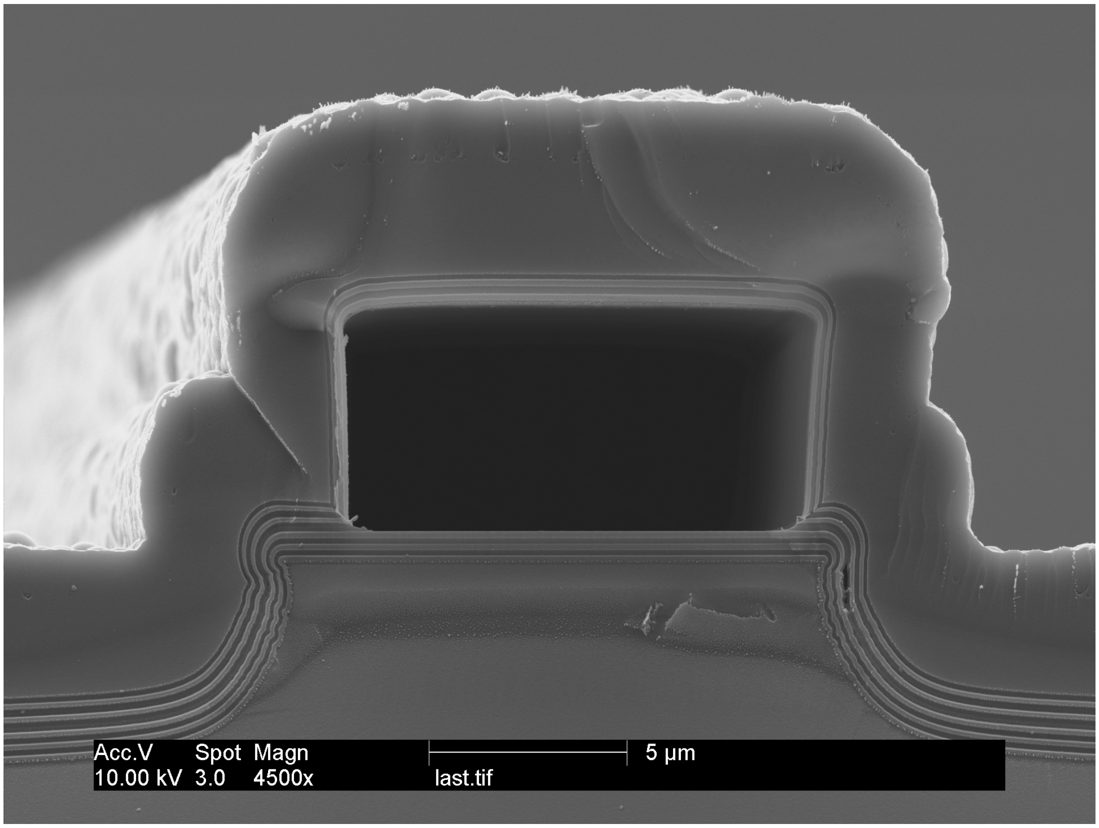

Figure 7.8 - SEM image of a hollow ARROW waveguide fabricated on a raised silicon pedestal. Note the air termination on both sides of the waveguide core. Also note the non-uniform layer widths on the sides due to the pedestal being wider than the core.

8 Applications of Hollow ARROW Waveguides

8.1 Introduction

As discussed in Chapter 1, many applications exist for integrated optical sensors. The ability of hollow ARROW waveguides to achieve light guiding in non-solid materials will enable many new applications of optical sensing as well as improvements to existing methods. The fabrication technique described here successfully integrates hollow ARROW waveguides with solid-core waveguides and enables easy attachment of microfluidic reservoirs. This process takes advantage of the low cost of silicon microfabrication and allows for the production of multiple devices in parallel.

This chapter discusses three applications of the hollow ARROW waveguides described previously. First, fluorescence sensing in liquid-core ARROW waveguides is presented. By combining a low-loss hollow ARROW waveguide with an intersecting solid-core waveguide, we have performed fluorescence measurements with single molecule sensitivity. Second, an optical filter structure was integrated into a hollow ARROW waveguide, and the results are given here. Finally, preliminary results from a capillary electrophoresis device based on a hollow ARROW waveguide are described. In addition to these applications, other uses of hollow ARROW waveguides in applications such as electromagnetically induced transparency (EIT) are currently being pursued [18], but are not described here. The process developed for hollow ARROW fabrication has also successfully been used to fabricate microfluidic devices such as electro-osmotic pumps and capillary electrophoresis systems [27].

8.2 Fluorescence Sensing

One of the most intriguing applications of hollow ARROW waveguides is their use in fluorescence sensing. Due to their small size and ability to guide light in liquid, the waveguides presented here are ideal for fluorescence studies of extremely small sample volumes. Experiments using our devices for fluorescence sensing were performed to demonstrate the suitability of integrated hollow ARROW waveguides for sensing platforms.

The first fluorescence sensing experiments using hollow ARROW waveguides utilized the setup shown in Figure 8.1 [24]. A waveguide was filled with ethylene glycol containing various concentrations of Alexa 647 dye. The waveguide was then illuminated at one end with a laser diode operating at 632 nm wavelength. The optical output at the other end was split and passed to an optical multimeter to detect the pump wavelength, while the second beam passed through bandpass filters selective to the fluorescence spectrum of the dye (650 to 700 nm) and detected by a photomultiplier tube.

Figure 8.2 shows the detected fluorescence power as a function of dye concentration. The waveguide used for this test has a 3.5 µm × 9 µm core with a length of 1.8 mm for a sample volume of 57 pL. The detection limit occurs at a dye concentration of 10^{-11} M, corresponding to approximately 490 dye molecules in the waveguide. This value is limited by detector sensitivity and residual power at the pump wavelength leaking through the bandpass filters. The collection efficiency of the waveguide, defined as the ratio of the fluorescence power detected to the power emitted by the sample, was measured to be approximately 15%.

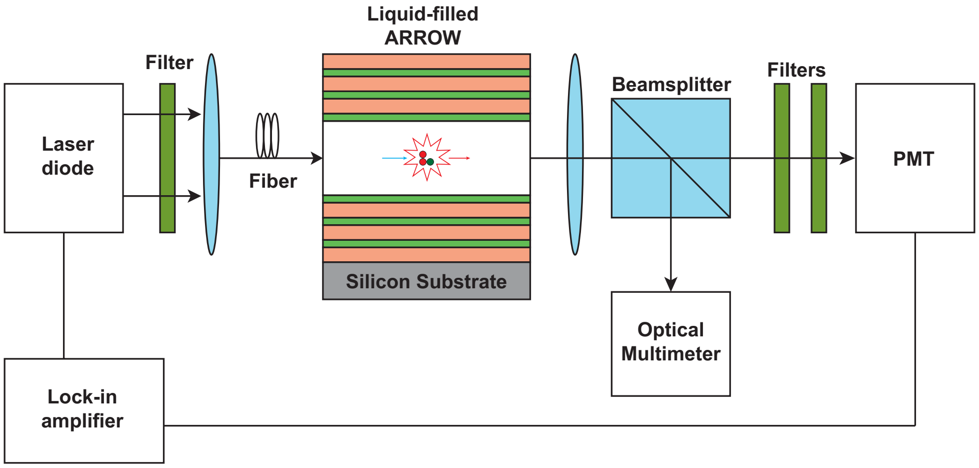

Figure 8.1 – Fluorescence measurement experimental setup. A photomultiplier tube is used to detect the fluorescent signal from the liquid-filled ARROW waveguide.

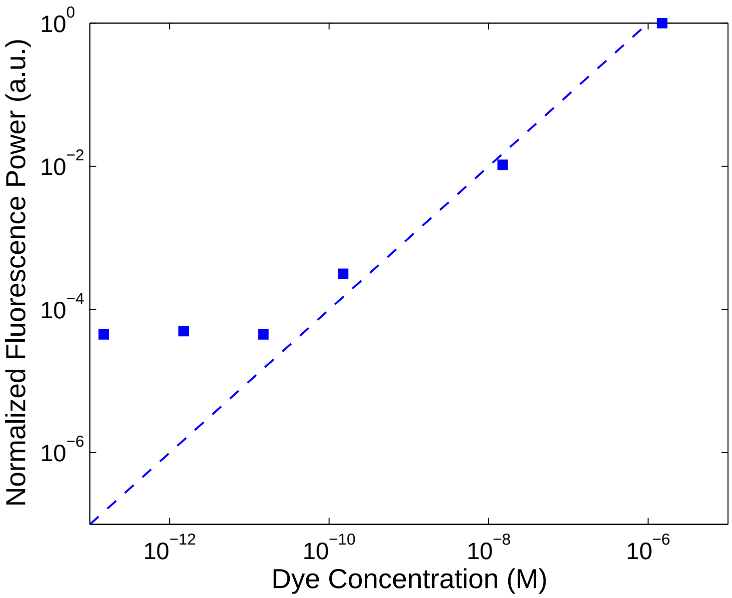

Figure 8.2 - Detected fluorescence power in a hollow ARROW waveguide vs. fluorescent dye concentration. Squares represent individual measurements, the dashed line is a linear fit to the points above the detection limit (10^{-11} M).

The integration of solid-core waveguides with hollow ARROWs represents a significant improvement in fluorescence detection. The pump light is coupled into a solid-core waveguide which intersects the hollow waveguide at a single point. Thus, the excitation volume can be very small, as it is determined by the cross-sectional area of the guided mode in the solid-core waveguide and the width of the liquid-core waveguide. Because the pump and fluorescence signals propagate at right angles, the pump light is suppressed at the detector, leading to improved sensitivity. Additionally, a platform using intersecting waveguides can take advantage of microfluidic connections and reservoirs. Figure 8.3 shows a fluorescence sensing platform utilizing an ‘S’-shaped hollow ARROW waveguide combined with solid-core waveguides and fluid reservoirs.

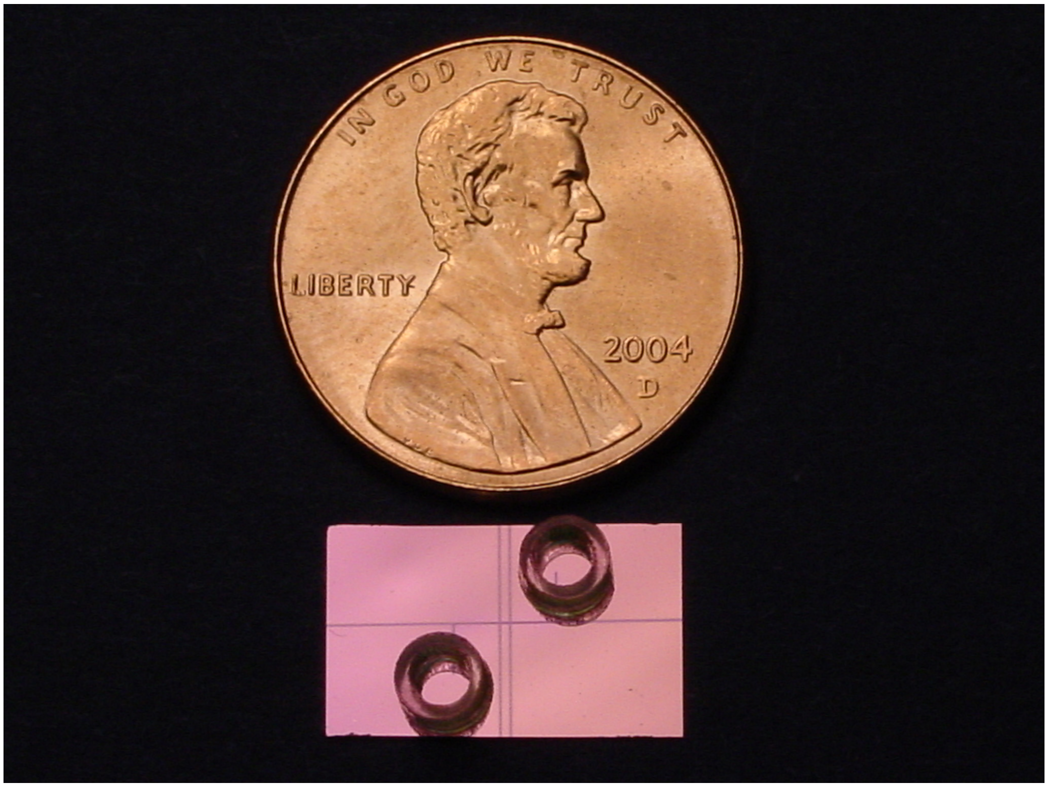

Figure 8.3 - Fluorescence sensing platform consisting of an 'S' shaped hollow ARROW waveguide with intersecting solid-core waveguides for optical pumping. Microfluidic reservoirs are attached to the ends of the hollow waveguide.

Measurements using intersecting waveguides were carried out using a setup similar to that in Figure 8.1, but with an avalanche photodiode (APD) replacing the photomultiplier tube for higher sensitivity. The suppression of the pump light at the output facet due to the perpendicular waveguide geometry was measured to be ~10^4, meaning that optical excitation of molecules outside of the intersection was negligible [20]. This results in an extremely small excitation volume, calculated to be 110 fL. The APD was used in single-photon counting mode, converting detected photons into voltage pulses which were then fed into a counter. Figure 8.4 shows that the photon count depends linearly on the average number of dye molecule in the excitation volume. These results indicate a detection sensitivity of a single dye molecule, demonstrating the suitability of integrated hollow ARROW waveguides for sensing platforms.

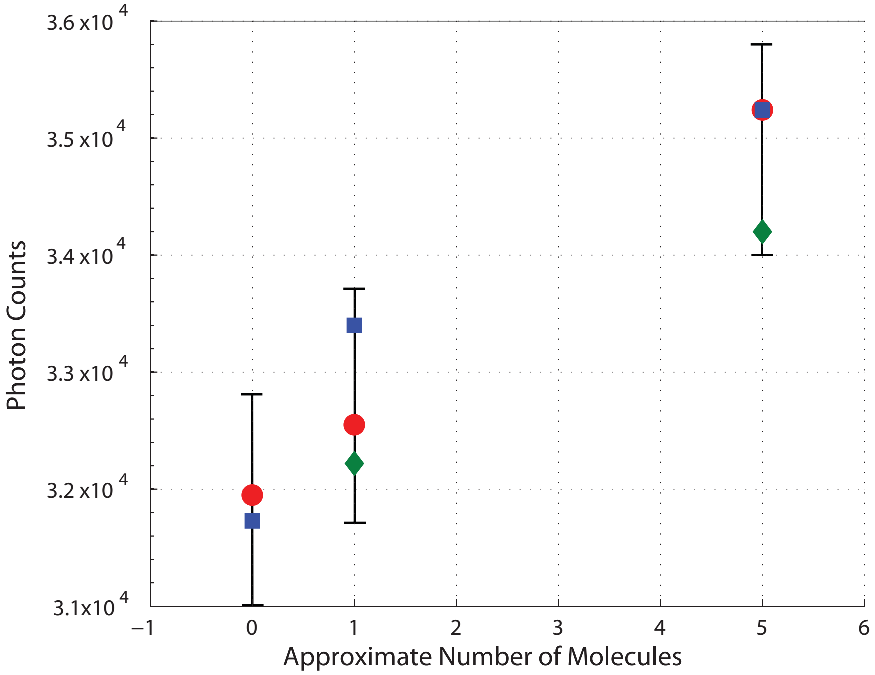

Figure 8.4 - Photon-counting fluorescence signal vs. dye concentration. Symbols are for different experiment runs, error bars show variation due to optical fiber alignment.

8.3 Integrated Optical Filters Based on ARROW Waveguides

As discussed in Chapter 2, the wavelength selectivity of ARROW waveguides can be modified to perform optical filtering. When used in a fluorescence-sensing platform like those described above, an integrated filter can significantly suppress the pump wavelength, preventing it from reaching the detector and eliminating the need for bulk optical filters at the output. The simple integration of optical filters with hollow ARROW waveguides represents another key advantage of the ARROW design paradigm.

To verify the wavelength selectivity of ARROW waveguides, a filter designed to pass light with a wavelength of 580 nm and attenuate 540 nm light was fabricated. The design process followed the steps outlined in Section 2.4.3 for the bottom nitride layers, and resulted in the following layer structure:

Table 8.1 - Layer structure of an integrated ARROW-based optical filter designed for transmission at 580 nm and attenuation at 540 nm.

Specifications		Layer Structure	
		Layer	Thickness (nm)
Wavelength	580 nm	Oxide 6	1956
Core	Liquid	Nitride 6	126
Core Shape	Rectangle	Oxide 5	326
Nitride Index	2.05	Nitride 5	126
		Oxide 4	326
Integrated optical filter design for liquid-core propagation at 580 nm and attenuation at 540 nm.		Nitride 4	126
		Core	4 μm
		Nitride 3	1284
		Oxide 3	479
		Nitride 2	1284
		Oxide 2	479
		Nitride 1	1284
		Oxide 1	479
		Substrate	-

Due to miscommunication with our collaborators at UC Santa Cruz, this design is non-optimal. The upper layer thicknesses are designed for transmission from 633 to 785 nm. This error was not discovered until after fabrication, and it was decided to test the devices in spite of the design error. The test results are shown in Figure 8.5, and indicate good attenuation of the unwanted wavelengths while still exhibiting low loss in the passband. These measurements taken from a non-optimal design show the flexibility of the ARROW waveguide design. Future devices with an optimized layer design should show improved wavelength selectivity.

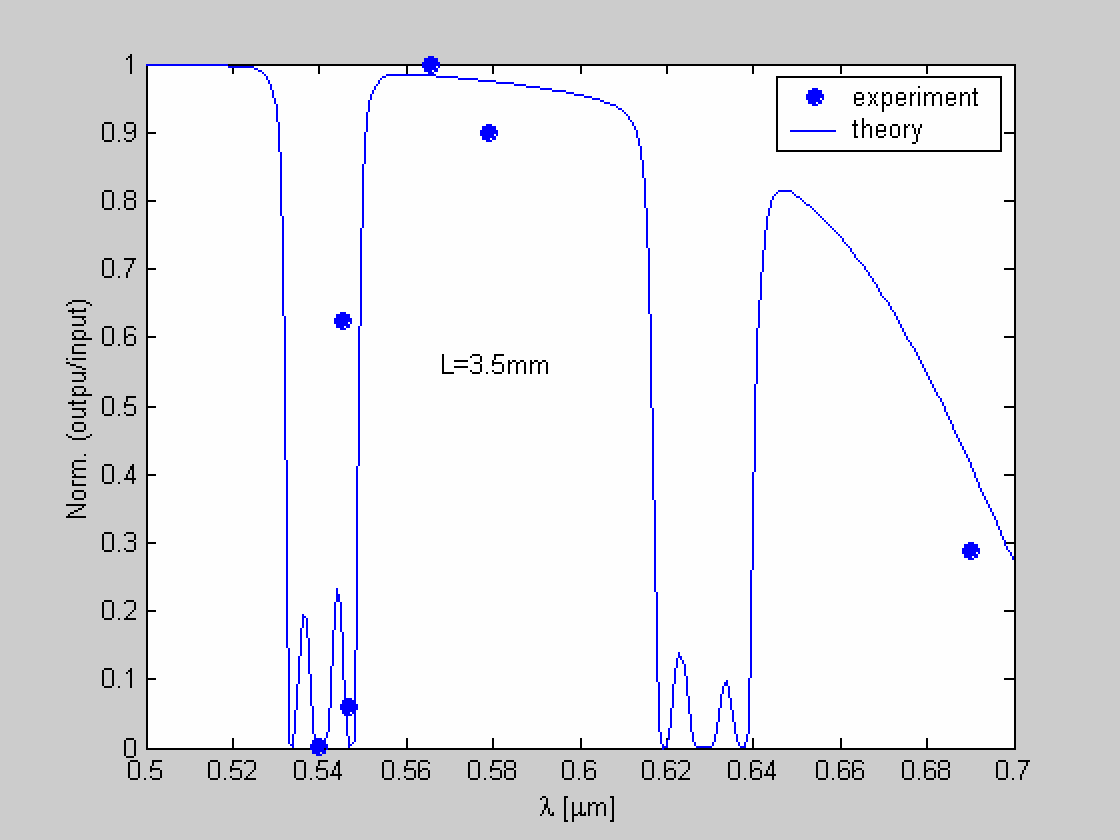

Figure 8.5 - Normalized optical output vs. wavelength for hollow ARROW-based filter. The solid line represents simulated behavior, circles are actual measurements. The filter was designed to pass 580 nm and attenuate 540 nm.

8.4 Capillary Electrophoresis

Capillary electrophoresis (CE) is a widely used technique for separating and analyzing materials such as amino acids and other biomolecules. Electrophoresis is the process of separating charged molecules by movement through a fluid in an electric field. The mechanism for separation is the differential mobility of the molecules in solution. Traditional electrophoresis makes use of a gel or other material as a substrate, while in capillary electrophoresis a thin capillary tube is the medium in which the separation takes place [111].

As mentioned previously, the fabrication process described here for hollow ARROW waveguides has successfully been used to create planar devices suitable for capillary electrophoresis [27]. These devices were fabricated on glass substrates to facilitate optical fluorescence detection of separated molecules using bulk optics. These devices demonstrated the feasibility of CE systems and other microfluidic components fabricated using the hollow ARROW process. The application of the sacrificial core process developed for hollow ARROW waveguides to such integrated microfluidic devices is currently an active area of research.

A number of fully planar CE devices based on a hollow ARROW waveguide were then fabricated on silicon substrates. The CE ARROW structure was designed for use with fluorescine 5-isothiocyanate (FITC), a common fluorescent marker used in amino acid separations. FITC efficiently absorbs at a pump wavelength of 488 nm and emits light with a wavelength of 520 nm. The layer structure of the CE ARROW devices used for this experiment is shown in Table 8.2.

Table 8.2 - Layer structure for CE ARROW device designed for operation at 488-520 nm.

Specifications		Layer Structure	
		Layer	Thickness (nm)
Wavelength	488-520 nm	Oxide 6	3006
Core	Liquid	Nitride 6	123
Core Shape	Rectangle	Oxide 5	317
Nitride Index	2.10	Nitride 5	123
		Oxide 4	317
CE separation device. Oxide 1 is thermally grown for improved electrical isolation from the silicon substrate.		Nitride 4	123
		Core	4.5 μm
		Nitride 3	83
		Oxide 3	214
		Nitride 2	83
		Oxide 2	214
		Nitride 1	83
		Oxide 1	2782
		Substrate	-

Because PECVD oxide has been found to be a poor electrical insulator, the first oxide layer was grown in a thermal oxidation furnace with a thickness of 2782 nm. This provides adequate insulation for the ~1000 V potential used to perform CE separations. A diagram of the CE ARROW device is shown in Figure 8.6, and a photograph of a completed device including fluid reservoirs is shown in Figure 8.7.

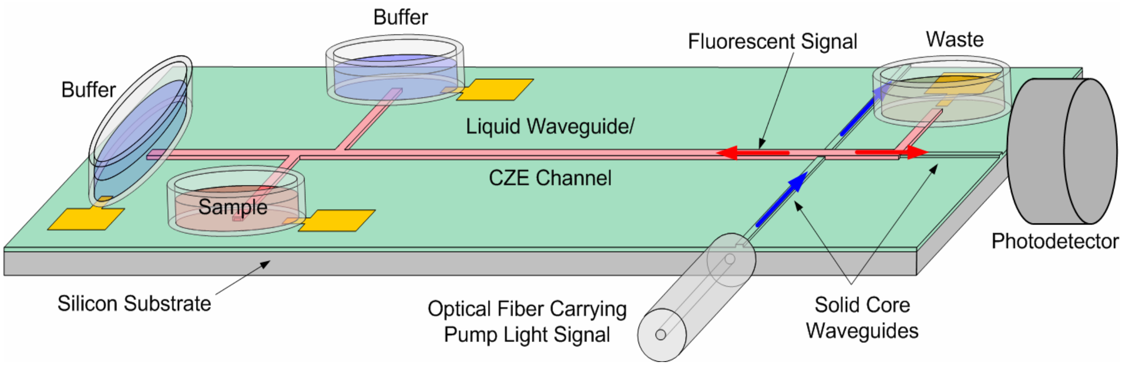

Figure 8.6 - Diagram of a hollow ARROW based capillary electrophoresis device showing optical interfaces and fluid reservoirs.

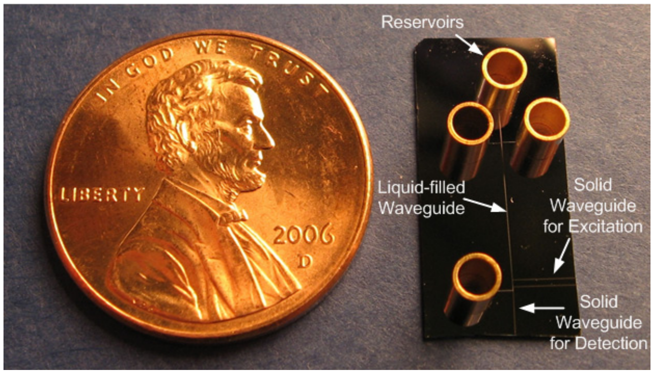

Figure 8.7 - Photograph of a CE separation device based on hollow ARROW waveguides with attached fluid reservoirs. Penny shown for scale.

Preliminary tests using these structures have been promising. A solution of three amino acids, arginine, phenylalanine, and glycine in carbonate buffer (100 mMol, pH 9.3) was used to test the feasibility of CE separation. The applied voltage was 600 V, for a separation field of 430 V/cm. Near the end of the separation channel, an intersecting solid-core waveguide illuminated the solution with 488 nm light, and the resulting fluorescence signal was collected by the hollow ARROW waveguide, coupled into a solid-core waveguide, and measured by a photodetector. The results shown in Figure 8.8 suggest that some separation of the amino acids took place, although the accuracy of the separation is uncertain. It should be noted that the device used for this experiment had cracks in several places, and improved devices should yield better results.

8.5 Conclusions

This chapter has presented the results of three applications of hollow ARROW waveguides. Optical fluorescence measurements with single-molecule sensitivity highlight the ability of hollow waveguides to collect and guide light, and the feasibility of interfacing with solid-core waveguides. The extremely small excitation volume of this setup was critical to the success of these measurements. Optical filters integrated into the hollow ARROW waveguide were also demonstrated, showing the flexibility of the ARROW paradigm. Such filters can greatly enhance the use of hollow ARROW waveguides for fluorescence measurements due to the ability to suppress the pump wavelength at the detector without external filters. Finally, the successful integration of a hollow ARROW waveguide into a capillary electrophoresis device shows that many potential applications exist for the waveguides presented here.

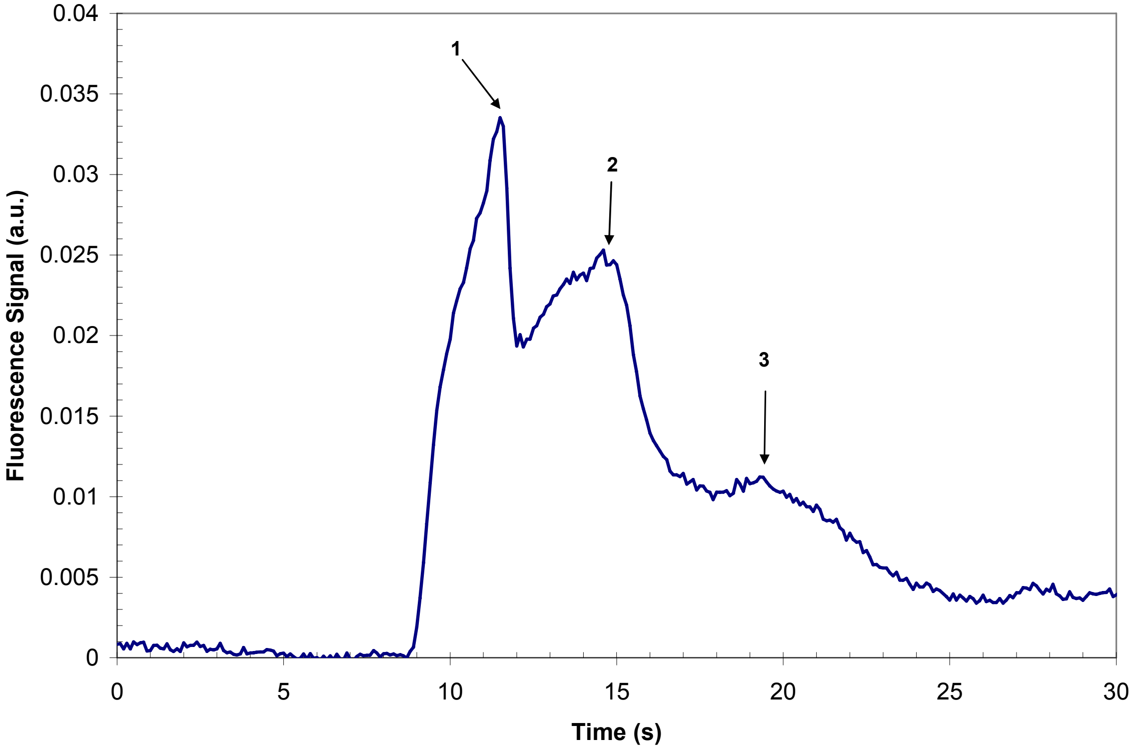

Figure 8.8 - Preliminary CE amino acid separation using a hollow ARROW device. Amino acids are arginine (1), phenylalanine (2), and glycine (3).

9 Conclusions

9.1 Summary

The research described in this dissertation began in 2003 and has resulted in successful fabrication of hollow ARROW waveguides and integrated solid-core waveguides, as well as application of these waveguides to integrated sensing platforms. Initial experiments used aluminum as a sacrificial material for hollow channel formation. This material was dropped in favor of SU-8 and positive photoresist. We have explored the fabrication process in depth, including studies of the mechanical strength of the hollow waveguides and etching characteristics of the sacrificial core materials.

To facilitate the application of hollow ARROW waveguides to integrated optical systems, we have created solid-core waveguides by adding an etch step to the fabrication process. Additional improvements such as the raised pedestal process described in Chapter 7 result in lower waveguide loss. To date, we have achieved a minimum waveguide loss of 2.6 cm^{-1} for air-core devices and 0.26 cm^{-1} for liquid cores.

Hollow ARROW waveguides have been used in fluorescence sensing applications. Preliminary experiments achieved a detection sensitivity of 490 molecules. An improved device making use of intersecting hollow and solid-core waveguides achieved single-molecule detection sensitivity with a sample volume of 110 fL.

Additional results presented here include proof-of–concept optical filters and CE separation devices based on hollow ARROW waveguides.

9.2 Future Work

9.2.1 Process Improvements

The fabrication process described in this dissertation has much potential for improvement. As discussed in Chapter 3, many challenges exist with respect to PECVD dielectric deposition. Future work could include characterization and control of film stress and roughness. The conformality of deposited films could also be improved by careful recipe development. Other issues relating to the PECVD process include particle generation in the chamber and the possibility of annealing the deposited films to reduce optical loss.

The sacrificial core process, which is a key aspect of our fabrication method, also has several unexplored avenues. As discussed in Chapter 6, hybrid aluminum-photoresist cores have reduced etch times. This concept could be extended to SU-8 cores, although adhesion problems have been observed with SU-8 and aluminum. One possibility is to pattern an aluminum line with a narrower width than the SU-8 core, allowing the SU-8 to adhere to the substrate rather than the aluminum. A mask was made for this process, but no experiments have been performed yet.

Another improvement to the sacrificial core process could involve the use of polycarbonate materials which undergo thermal decomposition into gaseous products [112], [113]. Although these materials are not compatible with PECVD deposition at high temperatures, they could be used in a lower temperature process, provided the resulting PECVD films were of sufficient optical and mechanical quality. Another intriguing possibility would be to use polycarbonate as a sacrificial pre-core, around which a larger sacrificial core of SU-8 or photoresist could be formed. The pre-core would then be removed by thermal decomposition, and the upper layer deposition in the PECVD could then take place using standard processing conditions. Although this would add to the complexity of the fabrication process, the sacrificial etch time could be reduced from weeks to hours if successful.

As discussed in Chapter 7, the limitations of the Anelva DEM-451 RIE must be overcome in order to reduce solid-core waveguide loss and difficulties with the pedestal etch process. New etch chemistries and different equipment such as an ICP-RIE could be explored for suitability for these processes. Another interesting possibility for the pedestal process is a self-aligned core. This would entail core deposition before the pedestal etch is performed, ensuring perfect alignment of the core to the pedestal, which is a significant challenge with the current process. However, the core material would need to withstand the pedestal etch process without developing roughness, and undercut of the core must be prevented. Improvements in the RIE etch process could mitigate these concerns.

Breakage of the upper dielectric layers is the significant source of failure of the fabrication process. At present, much of the breakage is not understood. Possible root causes include film stress and particle defects. PECVD process improvements have significant potential to reduce breakage. Additionally, better characterization of the core etch process could reduce breakage seen at waveguide junctions.

9.2.2 Applications

As mentioned throughout the text, myriad applications exist for hollow ARROW waveguides on planar substrates. Current results have achieved high detection sensitivity with fluorescence measurements. These results could be extended by the integration of optical filters in the ARROW waveguide. Additional waveguide components such as bends and tapers have not been fabricated to date, but represent intriguing possibilities for further work.

Preliminary results of CE separation, reported in Chapter 8, serve as a proof of concept, but are very poor compared to established CE separation platforms. Fabrication of more of these devices should yield better results, as the devices tested had significant cracks in the waveguide sidewalls. Improvements in the layout of these devices should increase the detection sensitivity and allow for better performance.

Finally, the potential for massively parallel devices based on hollow ARROW waveguides is virtually limitless. Integration with planar microfluidic systems based on the sacrificial core process we have developed will yield many new devices. Building-block components such as electroosmotic pumps and vias for multiple layers of fluid channels are currently being explored, and will enable many novel applications and systems. One such proposed device for protein analysis is shown in Figure 9.1. In summary, the future holds many exciting possibilities for integrated hollow ARROW waveguides.

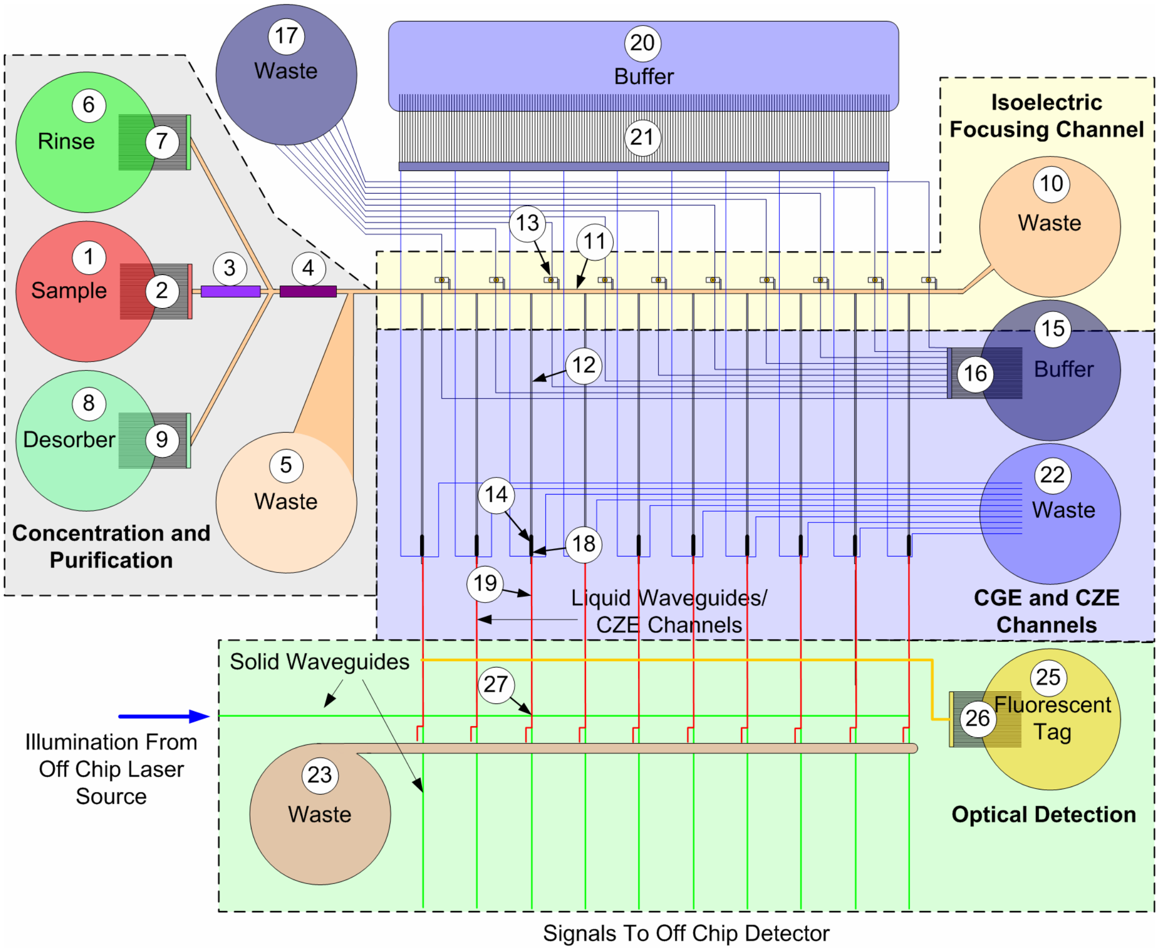

Figure 9.1 - Proposed complex system for protein analysis utilizing hollow ARROW waveguides and microchannels. 1, 5-6, 8, 10, 15, 17, 20, 22-23, 25 are microfluidic reservoirs. 2, 7, 9, 16, 21, 26 are electroosmotic pumps. 11 is an isoeletric focusing channel, and 12 and 19 are electrophoresis channels. Hollow ARROW waveguides (27) are used for fluorescence detection.

APPENDIX

Appendix A Process Recipes

A.1 Introduction

This section lists the process recipes used in the fabrication of the hollow ARROW waveguides described in this dissertation. Due to the dynamic nature of cleanroom equipment and supplies, process recipes are subject to frequent change. Therefore, these recipes should not be regarded as current. The IML web page [114] has current recipes, equipment operating procedures, and important safety information.

A.2 SU-8 Deposition and Patterning

SU-8 is a negative-tone photoresist that is used extensively in the hollow ARROW fabrication process. The general SU-8 recipe uses the following steps:

1) Dehydration bake on a 200°C hotplate for 10 minutes.
2) Place the wafer on the spinner, apply 10 drops of OmniCoat and spin at 3000 rpm for 1 minute.
3) Cure OmniCoat on a 200°C hotplate for 1 minute.
4) Place the wafer on the spinner and apply 10 mL of SU-8.
5) Spin for 2 minutes at the desired speed.
6) Soft bake on a 65°C hotplate for 5 minutes, ramp to 95°C, hold for 3 minutes.

7) Expose to UV light using the appropriate mask and exposure time.
8) Post-expose bake on a 65°C hotplate for 5 minutes, ramp to 95°C, hold for 3 minutes.
9) Develop in SU-8 developer with gentle agitation.
10) Remove the wafer from the developer solution and immediately rinse with isopropanol to remove all traces of SU-8 developer, dry with a nitrogen gun.
11) If white streaks are observed on the wafer, return it to the developer bath for 5 seconds, rinse with isopropanol and dry with a nitrogen gun.
12) Remove OmniCoat from wafer with a 60 second oxygen plasma descum.

OmniCoat is used as an adhesion promoter and a lift-off release layer for SU-8. It is not required for SU-8 processing, but has been observed to enhance adhesion to oxide and nitride films. OmniCoat is not compatible with HF, SC-1, or alkaline developer solutions, and will rapidly dissolve in these solutions. Therefore, wafers with OmniCoat and SU-8 should not be processed in these solutions.

SU-8 is relatively insensitive to variations in bake times and UV exposure. It is likely that most of the recipes listed below over-expose and over-bake the resist. Exposure times listed here assume a UV light intensity of 10 mW/cm^2. Consult the SU-8 data sheet for more information on exposure and bake times [103].

One significant issue with SU-8 processing is the formation of an edge bead, or raised ridge around the edge of the wafer. Ideally, an edge bead removal process involving a solvent spray on the back of the spinning wafer would be used. Lacking this process, spinning the wafer in an enclosed environment and allowing it to rest for 5 minutes in the enclosed spinner has been observed to reduce the edge bead.

Table A.1 – SU-8 process recipes showing target thickness, spin speed, and exposure and develop times.

Target Thickness (µm)	SU-8 Formulation	Spin Speed (RPM)	Exposure (s)	Develop Time (s)
3.5	SU-8 5	3500	18	50
4.0	SU-8 5	2750	19	50
4.5	SU-8 5	2250	20	50
5.8	SU-8 5	1350	21	55
10	SU-8 10	1800	24	65
15	SU-8 25	1500	27	85
5.8 (on pedestal)	SU-8 10	1800	21	55

A.3 PECVD Film Deposition

For detailed operating instructions for the PECVD, consult the IML web page. The recipes given here list actual flow rates for gases in units of sccm. The displayed flow rates on the PECVD, in units of percentage of full scale flow, will vary according to the installed MFC size and calibration. The refractive index of nitride films can be controlled by varying the ammonia (NH_4) flow. Increased ammonia will reduce the refractive index.

Chamber cleaning should be performed before each deposition to reduce particle deposition on the wafer. Long growths (greater than 30 minutes) should be broken into 30 minute increments with a chamber clean between each step. Before depositing nitride films, the empty chamber should be seasoned using the nitride deposition recipe for 2-3 hours.

Table A.2 – PECVD oxide deposition recipe.

Parameter	Value	Units
Gas 2 Flow (SiH_4/He)	104	sccm
Gas 3 Flow (N_2O)	17.8	sccm
RF Power	50	W
Pressure	900	mTorr
Temperature	250	°C
Growth Rate	22	nm/m

Table A.3 – PECVD nitride deposition recipe.

Parameter	Value	Units
Gas 1 Flow (NH_3)	6	sccm
Gas 2 Flow (SiH_4/He)	104	sccm
RF Power	100	W
Pressure	900	mTorr
Temperature	250	°C
Growth Rate	7	nm/m

Table A.4 – PECVD chamber clean recipe.

Parameter	Value	Units
Gas 4 Flow (CF_4/O_2)	100	sccm
RF Power	100	W
Pressure	350	mTorr
Temperature	< 100	°C

A.4 SC-1 Clean

1) Mix ammonium hydroxide (NH_4OH, 30%), hydrogen peroxide (H_2O_2, 30%), and deionized (DI) water in a ratio of 1:1:10 in a beaker or plastic container.
2) Place the wafer in the solution and agitate for 30-60 seconds.
3) Rinse the wafer in DI water and dry with a nitrogen gun.

A.5 SC-2 Clean

1) Mix hydrochloric acid (HCl, 30%), hydrogen peroxide (H_2O_2, 30%), and deionized (DI) water in a ratio of 1:1:10 in a beaker or plastic container.
2) Place the wafer in the solution and agitate for 30-60 seconds.
3) Rinse the wafer in DI water and dry with a nitrogen gun.

A.6 Photoresist Core

1) (Optional) For hybrid core, deposit 200 nm of aluminum via evaporation.
2) Dehydration bake on a 200°C hotplate for 10 minutes.
3) Place the wafer on the spinner and apply 12 mL of AZ 3330 photoresist.
4) Spin at 1000 RPM for 2 minutes.
5) Expose for 16 seconds using the appropriate mask.
6) Develop in AZ 300 MIF developer for 70 seconds, followed by a DI water rinse.
7) (Optional) For hybrid core, immerse in aluminum etch solution until aluminum is cleared from the wafer. Care is necessary to avoid over-etching and undercut of the photoresist. Rinse in DI water.
8) Photoresist reflow, 250°C hotplate for 10 minutes. The resist height after reflow should be 5.5 μm.
9) Perform an oxygen plasma descum for 60 seconds.

A.7 RIE Silicon Pedestal Etch

Consult the IML web page for current Anelva DEM-451 operating instructions. The recipe shown below will etch silicon, nitride and oxide at varying rates depending on the chamber condition and substance being etched. The observed repeatability of this process is very poor, so careful monitoring of the etch results is necessary.

Table A.5 – RIE silicon pedestal etch recipe.

Parameter	Value	Units
Gas 1 Flow (O_2)	3	sccm
Gas 3 Flow (CF_4)	12.5	sccm
RF Power	100	W
Pressure	100	mTorr
Etch Rate	100-200	nm/m

A.8 RIE Oxide Etch

Consult the IML web page for current Anelva DEM-451 operating instructions. The recipe shown below will etch silicon, nitride and oxide at varying rates depending on the chamber condition and substance being etched. The oxide etch rate is higher than for the silicon etch recipe shown above.

Table A.6 – RIE oxide etch recipe.

Parameter	Value	Units
Gas 1 Flow (O_2)	Not used	-
Gas 3 Flow (CF_4)	12.5	sccm
RF Power	300	W
Pressure	100	mTorr
Etch Rate	110	nm/m

A.9 RIE Oxygen Plasma Descum

Consult the IML web page for current Anelva DEM-451 operating instructions. Although several pieces of equipment can be used to perform oxygen descum processing, it is often convenient to use the Anelva DEM-451 for this purpose. The following recipe can be used immediately following an RIE etch step without venting the chamber.

Table A.7 – RIE oxygen plasma descum recipe.

Parameter	Value	Units
Gas 1 Flow (O_2)	30	sccm
Gas 3 Flow (CF_4)	Not used	-
RF Power	150	W
Pressure	100	mTorr

Appendix B ARROW Process Flow

This appendix describes the general process for fabrication of hollow ARROW waveguides. Optional steps include a raised silicon pedestal etch before waveguide formation, fabrication of integrated solid-core waveguides by etching a ridge into the top oxide layer of the hollow ARROW waveguides, and a core-expose etch to open the ends of the sacrificial cores in preparation for the core removal etch.

1) Scribe an identification mark on the back of a <100> silicon wafer.
2) (Optional) Pedestal process:
    a. Pattern SU-8 using the appropriate pedestal etch mask with a target thickness of 10 μm.
    b. Perform an oxygen plasma descum for 90 seconds.
    c. Perform an RIE silicon etch in the Anelva DEM-451 machine for 30 minutes.
    d. Perform a 5 minute oxygen plasma descum.
    e. Remove SU-8 residue in Nano-Strip at 90°C for 60 minutes, followed by a DI water rinse.
    f. Measure pedestal height and width using the profilometer. If incorrect, scrap the wafer and start over, adjusting the etch time as needed.

3) Remove native oxide in HF or buffered oxide etch (BOE), 1 minute or until the wafer dewets, followed by a DI water rinse.
4) Bottom dielectric layer deposition:
    a. Clean and season the PECVD chamber for the proper film type.
    b. Place a bare silicon test wafer in the PECVD chamber and deposit a test film (6 minute deposition for oxide, 10 minute deposition for nitride).
    c. Measure the test wafer using the ellipsometer and calculate the film growth rate.
    d. For nitride, adjust the refractive index of the film by changing the ammonia (NH_3) flow rate. An increased ammonia flow lowers the refractive index. Run more test wafers as necessary to achieve the desired refractive index.
    e. Place the wafer in the PECVD chamber and deposit the desired film using the measured growth rate from above to calculate the correct deposition time.
    f. Blow particles off of the wafer with a nitrogen gun and perform an SC-1 clean to remove remaining particles.
    g. Repeat steps a through f for each required dielectric layer.
5) Deposit and pattern the sacrificial core using the appropriate process for aluminum, SU-8, or photoresist.
6) Perform a 1 minute oxygen plasma descum, followed by a 3 second SC-2 clean.
7) Deposit the upper dielectric layers using the process in step 4 above, but omit the SC-1 clean between layers.

8) (Optional) Solid-core waveguide formation:
    a. Pattern SU-8 with a target thickness of 5 μm using the appropriate mask.
    b. Perform a 1 minute oxygen plasma descum.
    c. Perform an RIE oxide etch in the Anelva DEM-451 for 9 minutes, 20 seconds.
9) (Optional) Core expose etch:
    a. (Optional) If step 8 was performed, do a 2 minute oxygen plasma descum followed by a Nano-Strip etch at 90°C for 30 minutes and a DI water rinse.
    b. Pattern SU-8 with a target thickness of 10 μm using the appropriate mask.
    c. Perform a 1 minute oxygen plasma descum.
    d. Perform an RIE oxide etch in the Anelva DEM-451 for 40 minutes.
    e. Perform a 5 minute oxygen plasma descum.
10) Cleave the wafer and thin pieces to approximately 300 μm.
11) Place wafer pieces in the appropriate etchant for the sacrificial core material (*aqua regia* for aluminum and hybrid core, Nano-Strip for SU-8 core).
    a. Hotplate temperature should be 90°C for Nano-Strip and 120°C for *aqua regia*.
    b. Nano-Strip should be replaced every 24-48 hours with fresh solution. Care must be taken during the core removal etch to avoid breaking the waveguides. Slowly siphon off the old acid without disturbing the wafer pieces, and avoid contact between pieces in the same beaker due to rapid motion or pouring fresh acid too quickly.

12) (Optional) For hybrid cores, after the *aqua regia* etch, rinse thoroughly in DI water and place in Nano-Strip to remove the photoresist.

13) Carefully remove the etchant from the beaker and rinse the waveguides with DI water 6 times by slowly adding water, gently agitating the wafer pieces, and draining the water. After rinsing, soak the pieces in DI water for 24 hours, followed by 2 more DI water rinses. Dry the waveguides by placing the beaker on a hotplate at 90°C for 30 minutes or until the remaining water has evaporated.

14) Inspect the waveguides using a microscope and cleave as desired.

Appendix C ARROW Waveguide Designs

The layer structures for the ARROW waveguides discussed previously are given here. In general, the layer thicknesses were calculated using (2-6), although some of the values used were based on 3-d simulations of optimized waveguide structures. These simulations were performed at UCSC, and are not described here.

Table C.1 – Layer structure for air-core ARROW waveguide.

Specifications		**Layer Structure**	
		Layer	**Thickness (nm)**
Wavelength	785 nm	Oxide 6	2944
Core	Air	Nitride 6	109
Core Shape	Rectangle	Oxide 5	184
Nitride Index	2.05	Nitride 5	109
		Oxide 4	184
First-generation air-core design.		Nitride 4	109
		Core	3.5 μm
		Nitride 3	109
		Oxide 3	184
		Nitride 2	109
		Oxide 2	184
		Nitride 1	109
		Oxide 1	184
		Substrate	-

Table C.2 – Layer structure for liquid-core ARROW waveguide.

Specifications		Layer Structure	
		Layer	Thickness (nm)
Wavelength	685 nm	Oxide 6	3000
Core	Liquid	Nitride 6	110
Core Shape	Rectangle	Oxide 5	281
Nitride Index	2.05	Nitride 5	110
		Oxide 4	281
First liquid-core design.		Nitride 4	110
		Core	3.5 µm
		Nitride 3	110
		Oxide 3	281
		Nitride 2	110
		Oxide 2	281
		Nitride 1	110
		Oxide 1	281
		Substrate	-

Table C.3 – Layer structure for broadband liquid-core ARROW waveguide.

Specifications		Layer Structure	
		Layer	Thickness (nm)
Wavelength	633-785 nm	Oxide 6	1956
Core	Liquid	Nitride 6	126
Core Shape	Rectangle	Oxide 5	326
Nitride Index	2.05	Nitride 5	126
		Oxide 4	326
Liquid-core design for broadband operation.		Nitride 4	126
		Core	3.5 µm
		Nitride 3	126
		Oxide 3	326
		Nitride 2	126
		Oxide 2	326
		Nitride 1	126
		Oxide 1	326
		Substrate	-

Table C.4 – Layer structure for improved liquid-core ARROW waveguide with upper layer thickness compensation.

Specifications		Layer Structure	
		Layer	Thickness (nm)
Wavelength	633-785 nm	Oxide 6	1956
Core	Liquid	Nitride 6	159
Core Shape	Rectangle	Oxide 5	411
Nitride Index	2.05	Nitride 5	159
		Oxide 4	411
Second-generation liquid-core design with upper layer thickness compensation.		Nitride 4	159
		Core	3.5 µm
		Nitride 3	126
		Oxide 3	326
		Nitride 2	126
		Oxide 2	326
		Nitride 1	126
		Oxide 1	326
		Substrate	-

Table C.5 – Layer structure for improved liquid-core ARROW waveguide with upper layer thickness compensation and increased core height.

Specifications		Layer Structure	
		Layer	Thickness (nm)
Wavelength	633-785 nm	Oxide 6	3184
Core	Liquid	Nitride 6	159
Core Shape	Rectangle	Oxide 5	411
Nitride Index	2.05	Nitride 5	159
		Oxide 4	411
Third-generation liquid-core design with upper layer thickness compensation and increased core height.		Nitride 4	159
		Core	5.8 µm
		Nitride 3	126
		Oxide 3	326
		Nitride 2	126
		Oxide 2	326
		Nitride 1	126
		Oxide 1	326
		Substrate	-

Table C.6 – Layer structure for second-generation air-core ARROW waveguide.

Specifications		Layer Structure	
		Layer	Thickness (nm)
Wavelength	785 nm	Oxide 6	2576
Core	air	Nitride 6	134
Core Shape	Rectangle	Oxide 5	232
Nitride Index	2.10	Nitride 5	134
		Oxide 4	232
Second-generation air-core design with upper layer thickness compensation.		Nitride 4	134
		Core	3.5 μm
		Nitride 3	106
		Oxide 3	184
		Nitride 2	106
		Oxide 2	184
		Nitride 1	106
		Oxide 1	184
		Substrate	-

Table C.7 – Layer structure for air-core ARROW waveguide on raised silicon pedestal.

Specifications		Layer Structure	
		Layer	Thickness (nm)
Wavelength	785 nm	Oxide 6	3947
Core	Air	Nitride 6	106
Core Shape	Rectangle	Oxide 5	184
Nitride Index	2.05	Nitride 5	158
		Oxide 4	184
Air-core design on raised silicon pedestal.		Nitride 4	106
		Core	5 μm
		Nitride 3	106
		Oxide 3	184
		Nitride 2	106
		Oxide 2	184
		Nitride 1	106
		Oxide 1	184
		Substrate	Pedestal

Table C.8 – Layer structure for liquid-core ARROW waveguide with arched core.

Specifications		Layer Structure	
		Layer	Thickness (nm)
Wavelength	633-785 nm	Oxide 6	1920
Core	Liquid	Nitride 6	120
Core Shape	Arch	Oxide 5	320
Nitride Index	2.10	Nitride 5	120
		Oxide 4	320
Liquid-core design with arched core (reflowed photoresist).		Nitride 4	120
		Core	4 μm
		Nitride 3	120
		Oxide 3	320
		Nitride 2	120
		Oxide 2	320
		Nitride 1	120
		Oxide 1	320
		Substrate	-

Table C.9 – Layer structure for integrated optical filter based on an ARROW waveguide. The filter was designed for propagation at 580 nm and attenuation at 540 nm.

Specifications		Layer Structure	
		Layer	Thickness (nm)
Wavelength	580 nm	Oxide 6	1956
Core	Liquid	Nitride 6	126
Core Shape	Rectangle	Oxide 5	326
Nitride Index	2.05	Nitride 5	126
		Oxide 4	326
Integrated optical filter design for liquid-core propagation at 580 nm and attenuation at 540 nm.		Nitride 4	126
		Core	4 μm
		Nitride 3	1284
		Oxide 3	479
		Nitride 2	1284
		Oxide 2	479
		Nitride 1	1284
		Oxide 1	479
		Substrate	-

Table C.10 – Layer structure for capillary electrophoresis device based on an ARROW waveguide.

Specifications		Layer Structure	
		Layer	Thickness (nm)
Wavelength	488-520 nm	Oxide 6	3006
Core	Liquid	Nitride 6	123
Core Shape	Rectangle	Oxide 5	317
Nitride Index	2.10	Nitride 5	123
		Oxide 4	317
CE separation device. Oxide 1 is thermally grown for improved electrical isolation from the silicon substrate.		Nitride 4	123
		Core	4.5 μm
		Nitride 3	83
		Oxide 3	214
		Nitride 2	83
		Oxide 2	214
		Nitride 1	83
		Oxide 1	2782
		Substrate	-

References

[1] G. Lifante, *Integrated Photonics: Fundamentals*, New York: Wiley, 2003.

[2] E. J. Murphy, *Integrated Optical Circuits and Components: Design and Applications*, New York: Marcel Dekker, 1999.

[3] J. P. Wicksted, R. J. Erckens, M. Motamedi, and W. F. March, "Raman Spectroscopy Studies of Metabolic Concentrations in Aqueous Solutions and Aqueous Humor Specimens," *Applied Spectroscopy*, vol. 49, no. 7, Jul. 1995, pp. 987-993.

[4] C. Zander, J. Enderlein, and R. A. Keller (Eds.), *Single Molecule Detection in Solution*. Wiley: New York, 2002.

[5] J. R. Grunwell, J. L. Glass, T. D. Lacoste, A. A. Deniz, D. S. Chemla, and P. G. Schultz, "Monitoring the conformational fluctuations of DNA hairpins using single-pair fluorescence resonance energy transfer," *Journal of the American Chemical Society*, vol. 123, no. 18, May 2001, pp. 4295-4303.

[6] S. A. McKinney, A.-C. Déclais, D. M. J. Lilley, and T. Ha, "Structural dynamics of individual Holliday junctions," *Nature Structural Biology*, vol. 10, no. 2, Feb. 2003, pp. 93-97.

[7] T. Ha, A. Y. Ting, J. Liang, W. B. Caldwell, A. A. Deniz, D. S. Chemla, P. G. Schultz, and S. Weiss, "Single-molecule fluorescence spectroscopy of enzyme conformational dynamics and cleavage mechanism," *Proceedings of the National Academy of Science of the United States of America*, vol. 96, no. 3, Feb. 1999, pp. 893-898.

[8] D. S. Talaga, W. L. Lau, H. Roder, J. Tang, Y. Jia, W. F. DeGrado, and R. M. Hochstrasser, "Dynamics and folding of single two-stranded coiled-coil peptides studied by fluorescent energy transfer confocal microscopy," *Proceedings of the National Academy of Science of the United States of America,* vol. 97, no. 24, Nov. 2000, pp. 13021-13026.

[9] E. Rhoades, E. Gussakovsky, and G. Haran, “Watching proteins fold one molecule at a time,” *Proceedings of the National Academy of Science of the United States of America,* vol. 100, no. 6, Mar. 2003, pp. 3197-3202.

[10] X. Zhuang, L. E. Bartley, H. P. Babcock, R. Russell, T. Ha, D. Herschlag, and S. Chu, “A single-molecule study of RNA catalysis and folding,” *Science*, vol. 288, Jun. 2000, pp. 2048-2051.

[11] W. E. Moerner and D. P. Fromm, “Methods of single-molecule fluorescence spectroscopy and microscopy,” *Review of Scientific Instruments*, vol. 74, no. 8, Aug. 2003, pp. 3597-3619.

[12] M. J. Levene, J. Korlach, S. W. Turner, M. Foquet, H. G. Craighead, and W. W. Webb, “Zero-mode waveguides for single-molecule analysis at high concentrations,” *Science*, vol. 299, Jan. 2003, pp. 682-686.

[13] N.-T. Nguyen and S. Werely, *Fundamentals and Applications of Microfluidics*, Boston: Artech House, 2002.

[14] V. P. Maltsev, “Scanning flow cytometry for individual particle analysis,” *Review of Scientific Instruments*, vol. 71, no. 1, Jan. 2000, pp. 243-255.

[15] O. Leistiko and P. F. Jensen, “Integrated bio/chemical microsystems employing optical detection: the clip-on,” *Journal of Micromechanics and Microengineering*, vol. 8, no. 2, Jun. 1998, pp. 148-151.

[16] L. Cui, T. Zhang, and H. Morgan, “Optical particle detection integrated in a dielectrophoretic lab-on-a-chip,” *Journal of Micromechanics and Microengineering*, vol. 12, no. 1, Jan. 2002, pp. 7-13.

[17] B. Helbo, A. Kristensen, and A. Menon, “A micro-cavity fluidic dye laser,” *Journal of Micromechanics and Microengineering*, vol. 13, no. 2, Mar. 2003, pp. 307–311.

[18] H. Schmidt and A. R. Hawkins, “Electromagnetically induced transparency in alkali atoms integrated on a semiconductor chip,” *Applied Physics Letters*, vol. 86, no. 3, Jan 2005, 032106.

[19] J. R. Lee, J. P. Barber, Z. A. George, M. L. Lee, H. Schmidt, and A. R. Hawkins, “Micro-channels with rectangular and arched core shapes fabricated using sacrificial etching,” *Journal of Microlithography, Microfabrication, and Microsystems*, to be published.

[20] D. Yin, D. W. Deamer, H. Schmidt, J. P. Barber, and A. R. Hawkins, “Single-molecule detection sensitivity using planar integrated optics on a chip,” *Optics Letters*, vol. 31, no. 14, Jul. 2006, pp. 2136-2138.

[21] J. P. Barber, E. J. Lunt, Z. A. George, D. Yin, H. Schmidt, and A. R. Hawkins, "Integrated Hollow Waveguides with Arch-shaped Cores", *Photonics Technology Letters*, vol. 18, no. 1, Jan. 2006, pp. 28-30.

[22] D. Yin, H. Schmidt, J. P. Barber, E. J. Lunt, and A. R. Hawkins, "Optical Characterization of arch-shaped ARROW waveguides with liquid cores," *Optics Express*, vol. 13, no. 26, Dec. 2005, pp. 10564-10570.

[23] D. Yin, J. P. Barber, A. R. Hawkins, and H. Schmidt, "Waveguide loss optimization in hollow-core ARROW waveguides," *Optics Express*, vol. 13, no. 23, Nov. 2005, pp. 9331-9336.

[24] D. Yin, J. P. Barber, A. R. Hawkins, and H. Schmidt, "Highly efficient fluorescence detection in picoliter volume liquid-core waveguides," *Applied Physics Letters*, vol. 87, Nov. 2005, 211111.

[25] H. Schmidt, D. Yin, J. P. Barber, and A. R. Hawkins, "Hollow-core waveguides and 2-D waveguide arrays for integrated optics of gases and liquids," *IEEE Journal of Selected Topics in Quantum Electronics*, vol. 11, no. 2, Apr. 2005, pp. 519-527.

[26] N. B. Hubbard, L. L. Howell, J. P. Barber, D. B. Conkey, A. R. Hawkins, and H. Schmidt, "Structural models and design rules for on-chip micro-channels with sacrificial cores," *Journal of Micromechanics and Microengineering*, vol. 15, no. 4, Apr. 2005, pp.720-727.

[27] B. A. Peeni, D. B. Conkey, J. P. Barber, R. T. Kelly, M. L. Lee, A. T. Wooley, and A. R. Hawkins, "Planar thin film device for capillary electrophoresis," *Lab on a Chip*, vol. 5, Mar. 2005, pp. 501-505.

[28] J. P. Barber, D. B. Conkey, J. R. Lee, N. B. Hubbard, L. L. Howell, H. Schmidt, and A. R. Hawkins, "Fabrication of Hollow Waveguides with Sacrificial Aluminum Cores", *Photonics Technology Letters,* vol. 17, no. 2, Feb. 2005, pp. 363-365.

[29] D. Yin, D. W. Deamer, J. P. Barber, A. R. Hawkins, and H. Schmidt, "Integrated optical waveguides with liquid cores," *Applied Physics Letters*, vol. 85, no. 16, Oct. 2004, pp. 3477-3479.

[30] D. Yin, J. P. Barber, A. R. Hawkins, and H. Schmidt, "Integrated ARROW waveguides with hollow cores," *Optics Express*, vol. 12, no. 12, Jun. 2004, pp. 2710-2715.

[31] H. Schmidt, D. Yin, P. S. Measor, J. P. Barber, E. J. Lunt, and A. R. Hawkins, "Single-molecule optofluidics using liquid-core ARROW waveguides", Invited Talk, presented at the IEEE LEOS Summer Topical Meeting on Optofluidics: Emerging technologies and applications, Quebec City, Canada, Jul. 17-19, 2006.

[32] D. Yin, J. P. Barber, A. R. Hawkins, and H. Schmidt, "Single molecule sensitivity and electrically controlled fluorescence detection in integrated planar ARROW waveguides", presented at Conference on Lasers and Electro-Optics, Long Beach, CA, May 21-26, 2006.

[33] P. S. Measor, D. Yin, J. P. Barber, L. Seballos, J. Zhang, A. R. Hawkins, and H. Schmidt, "Integrated liquid-core ARROW waveguides for surface-enhanced Raman scattering", presented at the Conference on Lasers and Electro-Optics, Long Beach, CA, May 21-26, 2006.

[34] D. Yin, J. P. Barber, E. J. Lunt, D. Ermolenko, H. Noller, A. R. Hawkins, and H. Schmidt, "Planar single-molecule sensors based on hollow-core ARROW waveguides", *Proceedings of the SPIE*, vol. 6125, Feb. 2006, 61250Q.

[35] H. Schmidt, D. Yin, W. Yang, D. B. Conkey, J. P. Barber, A. R. Hawkins, and B. Wu, "Towards integration of quantum interference in alkali atoms on a chip," *Proceedings of the SPIE*, vol. 6130, Feb. 2006, 613006.

[36] J. P. Barber, E. J. Lunt, D. Yin, H. Schmidt, and A. R. Hawkins, "Monolithic fabrication of hollow ARROW-based sensors," *Proceedings of the SPIE*, vol. 6110, Jan. 2006, 61100H.

[37] M. M. Smith, J. P. Barber, B. A. Peeni, D. Yin, H. Schmidt, and A. R. Hawkins, "Planar fabrication of liquid core optical waveguides and microfluidic devices", presented at the 8th Joint Conference on Information Sciences, Salt Lake City, UT, Jul. 21-26, 2005.

[38] D. Yin, J. P. Barber, A. R. Hawkins, and H. Schmidt, "Fluorescence detection of few molecules with high collection efficiency in ARROWs", presented at the Conference on Lasers and Electro-Optics, Baltimore, MD, May 22-27 2005.

[39] J. P. Barber, D. B. Conkey, M. M. Smith, J. R. Lee, B. A. Peeni, Z. A. George, A. R. Hawkins, D. Yin and H. Schmidt, "Hollow waveguides on planar substrates with selectable geometry cores", presented at the Conference on Lasers and Electro-Optics, Baltimore, MD, May 22-27 2005.

[40] D. Yin, J. P. Barber, A. R. Hawkins, and H. Schmidt, "Fluorescence detection in integrated intersecting ARROW waveguides with liquid and solid cores", presented at the Integrated Photonics Research Conference, San Diego, CA, Apr. 11-14 2005.

[41] J. P. Barber, M. M. Smith, A. R. Hawkins, D. Yin and H. Schmidt, "Integrated hollow and solid-core waveguides for sensor platforms", presented at the Integrated Photonics Research Conference, San Diego, CA, Apr. 11-14 2005.

[42] D. Yin, J. P. Barber, A. R. Hawkins, and H. Schmidt, "Low loss integrated optical sensors based on hollow core ARROW waveguide", *Proceedings of the SPIE*, vol. 5730, Mar. 2005, pp. 218-225.

[43] H. Schmidt, D. Yin, D. W. Deamer, J. P. Barber, and A. R. Hawkins, "Integrated ARROW waveguides for gas/liquid sensing", *Proceedings of the SPIE*, vol. 5515, Oct 2004, pp. 67-80.

[44] D. Yin, D. W. Deamer, J. P. Barber, A. R. Hawkins, and H. Schmidt, "Integrated biophotonic sensor with single-molecule resolution", presented at the Conference on Lasers and Electro Optics, San Francisco, CA, May 16-21, 2004.

[45] H. Schmidt, D. Yin, J. P. Barber, G. Sanber, E. Despain, and A. R. Hawkins, "Integration of Electromagnetically Induced Transparency in Alkali Atoms on a Semiconductor Chip", presented at the International Quantum Electronics Conference, San Francisco, CA, May 16-21, 2004.

[46] D. Yin, J. P. Barber, A. R. Hawkins, and H. Schmidt, "Low-loss propagation in hollow ARROW waveguides for optical sensing", presented at the Conference on Lasers and Electro Optics, San Francisco, CA, May 16-21, 2004.

[47] J. Lowry, J. Mendlowitz, and N. Subramanian, "Optical characteristics of Teflon AF® fluoroplastic materials," *Optical Engineering*, vol. 31, no. 9, Sep. 1992, pp.1982–1985.

[48] P. D. Dasgupta, Z. Genfa, J. Li, C. B. Boring, S. Jambunathan, and R. Al-Horr, "Luminescence Detection with a Liquid Core Waveguide," *Analytical Chemistry*, vol. 71, no. 7, Apr. 1999, pp. 1400-1407.

[49] R. Altkorn, I. Koev, R. P. Van Duyne, and M. Litorja, "Low-loss liquid-core optical fiber for low-refractive-index liquids: Fabrication, characterization, and application in Raman spectroscopy," *Applied Optics*, vol. 36, no. 34, Dec. 1997, pp. 8992–8998.

[50] R. Altkorn, I. Koev, and A. Gottlieb, "Waveguide capillary cell for low-refractive-index liquids," *Applied Spectroscopy*, vol. 51, no. 10, Oct. 1997, pp. 1554–1558.

[51] J. Li and P. K. Dasgupta, "Chemiluminescence detection with a liquid-core waveguide. Determination of ammonium with electrogenerated hypochlorite based on the luminol-hypochlorite reaction," *Analytica Chimica Acta*, vol. 398, Oct. 1999, pp. 33–39.

[52] A. Datta, I.-Y. Eom, A. Dhar, P. Kuban, R. Manor, I. Ahmad, S. Gangopadhyay, T. Dallas, M. Holtz, H. Temkin, and P. K. Dasgupta, "Microfabrication and characterization of Teflon AF-coated liquid core waveguide channels in silicon," *IEEE Sensors Journal*, vol. 3 no. 6, Dec. 2003, pp. 788-795.

[53] W. P. Risk, H.-C. Kim, R. D. Miller, H. Temkin, and S. Gangopadhyay, "Optical waveguides with an aqueous core and a low-index nanoporous cladding," *Optics Express*, vol 12, no. 26, Dec. 2004, pp. 6446-6455.

[54] J. D. Joannopoulos, R. D. Meade, and J. N. Winn, *Photonic Crystals: Molding the Flow of Light*, New Jersey: Princeton University Press, 1995, pp. 3-5.

[55] P. Yeh and A. Yariv, "Bragg reflection waveguides," *Optics Communications*, vol. 19, no. 3, Dec. 1976, pp. 427-430.

[56] P. Yeh, A. Yariv, and E. Marom, "Theory of Bragg fiber," *Journal of the Optical Society of America*, vol. 68, no. 9, Sep. 1978, pp. 1196-1201.

[57] A. Y. Cho, A. Yariv, and P. Yeh, "Observation of confined propagation in Bragg waveguides," *Applied Physics Letters*, vol. 30, no. 9, May 1977, pp. 471-472.

[58] B. Nistad, M. W. Haakestad, and J. Skaar, "Dispersion properties of planar Bragg waveguides," *Optics Communications*, vol. 256, 2006, pp. 153-160.

[59] J. N. Winn, Y. Fink, S. Fan, and J. D. Joannopoulos, "Omnidirectional reflection from a one-dimensional photonic crystal," *Optics Letters*, vol. 23, no. 20, Oct. 1998, pp. 1573-1575.

[60] Y. Fink, J. N. Winn, S. Fan, C. Chen, J. Michel, J. D. Joannopoulos, and E. L. Thomas, "A dielectric omnidirectional reflector," *Science*, vol. 282, Nov. 1998, pp. 1679-1682.

[61] J. C. Knight, T. A. Birks, P. St. J. Russell, and D. M Atkin, "All-silica single-mode optical fiber with photonic crystal cladding," *Optics Letters*, vol. 21, no. 19, Oct. 1996, pp. 1547-1549.

[62] J. N. Winn, R. D. Meade, and J. D. Joannopoulos, "Two-dimensional photonic bandgap materials," *Journal of Modern Optics*, vol. 41, no. 2, Feb. 1994, pp. 257-273.

[63] M. Loncara, D. Nedeljkovic, T. Doll, J. Vuckovic, A. Scherer, and T. P. Pearsall, "Waveguiding in planar photonic crystals," *Applied Physics Letters*, vol. 77, no. 13, Sep. 2000, pp. 1937-1939.

[64] S. Ghosh, J. E. Sharping, D. G. Ouzonov, and A. L. Gaeta, "Coherent resonant interactions and slow light with molecules confined in photonic band-gap fibers," *Physical Review Letters*, vol. 94, no. 9, Mar. 2005, 093902.

[65] M. A. Duguay, Y. Kokubun, and T. L. Koch, "Antiresonant reflecting optical waveguides in SiO2-Si multilayer structures," *Applied Physics Letters*, vol. 49, no. 1, Jul. 1986, pp. 13-15.

[66] J.-L. Archambault, R. J. Black, S. Lacroix, and J. Bures, "Loss calculations for antiresonant waveguides," *Journal of Lightwave Technology*, vol. 11, no. 3, Mar. 1993, pp. 416-423.

[67] L. J. Mawst, D. Botez, C. Zmudzinski, and C. Tu, "Design optimization of ARROW-type diode lasers," *Photonics Technology Letters*, vol. 4, no. 11, Nov. 1992, pp. 1204-1206.

[68] S. G. Pattersion, G. S. Petrich, R. J. Ram, and L. A. Kolodiejski, "Continuous-wave room temperature operation of bipolar cascade laser," *Electronics Letters*, vol. 35, no. 5, Mar. 1999, pp. 395-396.

[69] M. Mann, U. Trutschel, C. Wachter, L. Leine, and F. Lederer, "Directional coupler based on an antiresonant reflecting optical waveguide," *Optics Letters*, vol. 16, no. 11, Jun. 1991, pp. 805-807.

[70] F. Preito, A. Llobera, D. Jimenez, C. Domenguez, A.Calle, and L. M. Lechuga, "Design and analysis of silicon antiresonant reflecting optical waveguides for evanescent field sensor," *Journal of Lightwave Technology*, vol. 18, no. 7, Jul. 2000, pp. 966-972.

[71] R. Bernini, S. Campopiano, and L. Zeni, "Silicon micromachined hollow optical waveguides for sensing applications," *IEEE Journal of Selected Topics in Quantum Electronics*, vol. 8, no. 1, Jan. 2002, pp. 106-110.

[72] S. Campopiano, R. Bernini, L. Zeni, and P. Sarro, "Microfluidic sensor based on integrated optical hollow waveguides," *Optics Letters*, vol. 29, no. 16, Aug. 2004, pp. 1894-1896.

[73] N. M. Litchinitser, A. K. Abeeluck, C. Headley, and B. J. Eggleton, "Antiresonant reflecting photonic crystal optical waveguides," *Optics Letters*, vol. 27, no. 18, Sep. 2002, pp. 1592-1594.

[74] J. Chilwell and I. Hodgkinson, "Thin-films field-transfer matrix theory of planar multilayer waveguides and reflection from prism-loaded waveguides," *Journal of the Optical Society of America A*, vol. 1, no. 7, Jul. 1984, pp. 742-753.

[75] R. G. Hunsperger, *Integrated Optics: Theory and Technology (Second Edition)*, Berlin: Springer-Verlag, 1984, pg. 70.

[76] P. Yeh, *Optical Waves in Layered Media*, New York: Wiley Interscience, 1988, pp. 118-134.

[77] J. Gehler, A. Brauer, W. Karthe, U. Trutschel, and M. A. Duguay, "ARROW-based optical wavelength filter in silica," *Electronics Letters*, vol. 31, no. 7, Mar. 1995, pp. 547-548.

[78] Z. M. Mao and W. P Huang, "An ARROW optical wavelength filter: design and analysis," *Journal of Lightwave Technology*, vol. 11, no. 7, Jul. 1993, pp. 1183-1188.

[79] M. A. Schmidt, “Wafer-to-wafer bonding for microstructure formation,” *Proceedings of the IEEE*, vol. 86, no. 8, Aug. 1998, pp. 1575-1585.

[80] S. Lo, M. Wang, and C. Chen, “Semiconductor hollow optical waveguides formed by omni-directional reflectors,” *Optics Express*, vol. 12, no. 26, Dec. 2004, pp. 6589-6593.

[81] G. R. Hadley, J. G. Fleming, and S.-Y. Lin, “Bragg fiber design for linear polarization,” *Optics Letters*, vol. 29, no. 8, 2004, pp. 809-811.

[82] D. Bhusari, H. A. Reed, M. Wedlake, A. M. Padovani, S. A. B. Allen, and P. A. Kohl, “Fabrication of air-channel structures for microfluidic, microelectromechanical, and microelectronic applications,” *Journal of Microelectromechanical Systems*, vol. 10, no. 3, Sep. 2001, pp. 400-408.

[83] J. M. Bustillo, R. T. Howe, and R. S. Muller, “Surface micromachining for microelectromechanical systems,” *Proceedings of the IEEE*, vol. 86, no. 8, Aug. 1998, pp. 1552-1574.

[84] A. Sherman, *Chemical Vapor Deposition for Microelectronics: Principles, Technology and Applications*. New Jersey: Noyes Publications, 1987, pg. 35.

[85] A. Sherman, *Chemical Vapor Deposition for Microelectronics: Principles, Technology and Applications*. New Jersey: Noyes Publications, 1987, pp. 119-135.

[86] W. A. P. Classen, W. G. J. N. Valkenburg, F. H. P. M. Habraken and Y. Taminga, “Characterization of plasma silicon nitride layers,” *Journal of the Electrochemical Society*, vol. 130, no. 12, Dec. 1983, pp. 2419-2423.

[87] S. Sivaram, *Chemical Vapor Deposition: Thermal and Plasma Deposition of Electronic Materials*. New York: Van Nostrand Reinhold, 1995, pg. 214.

[88] W. A. P. Classen, W. G. J. N. Valkenburg, M. F. C. Willemsen and W. M. Wijgert, “Influence of deposition temperature, gas pressure, gas phase composition and RF frequency on composition and mechanical stress of plasma silicon nitride layer,” *Journal of the Electrochemical Society*, vol. 132, no. 4, Apr. 1985, pg. 893-898.

[89] T. J. Cotler and J. Chapple-Sokol, “High quality plasma-enhanced chemical vapor deposited silicon nitride films,” *Journal of the Electrochemical Society*, vol. 140 no.7, Jul. 1993, pp. 2071-2075.

[90] W. A. P. Classen, “Ion bombardment-induced mechanical stress in plasma-enhanced deposited silicon nitride and silicon oxynitride films,” *Plasma Chemistry and Plasma Processing*, vol. 7, no. 1, Mar. 1987, pp. 109-124.

[91] E. van de Ven, I. Connick and A. S. Harrus, "Advantages of dual frequency PECVD for deposition of ILD and passivation films," in *Proceedings of the IEEE VLSI Multilevel Interconnection Conference*, 1990, pp. 194-201.

[92] S. Sivaram, *Chemical Vapor Deposition: Thermal and Plasma Deposition of Electronic Materials*. New York: Van Nostrand Reinhold, 1995, pp. 21-28.

[93] M. Konuma, *Plasma Techniques for Film Deposition*. Harrow, U.K.: Alpha Science International, Ltd., 2005, pp.222-223.

[94] K. Allaert, A. van Calster, H. Loos and A. Lequesne, "A comparison between silicon nitride films made by PECVD of N2-SiH4/Ar and N2-SiH4/He," *Journal of the Electrochemical Society*, vol. 132, no. 7, Jul. 1985, pp.1763.

[95] W. Kern, "The evolution of silicon wafer cleaning technology," *Journal of the Electrochemical Society*, vol. 137, no. 6, Jun. 1990, pp. 1887-1892.

[96] M. Itano, F. W. Kern, M. Miyashita and T. Ohmi, "Particle removal from silicon wafer surface in wet cleaning process," *IEEE Transactions on Semiconductor Manufacturing*, vol. 6, no. 3, Aug. 1993, pp. 258-267.

[97] W. Kern, *Handbook of Semiconductor Wafer Cleaning Technology: Science, Technology and Applications*, New Jersey: Noyes Publications, 1993, pg. 49.

[98] S. M. Sze, *Semiconductor Devices: Physics and Technology, 2nd Edition*. New York: Wiley, 2002, pp. 392-395.

[99] *CRC Handbook of Metal Etchants*, P. Walker and W. H. Tarn, eds., Boca Raton, FL: CRC Press, 1991, pp. 596-597.

[100] D. Westberg, O. Paulz, G. I. Andersson and H. Baltes, "Surface micromachining by sacrificial aluminum etching," *Journal of Micromechanics and Microengineering*, vol. 6, no. 4, Dec. 1996, pp. 376-384.

[101] N. Maluf, *An Introduction to Microelectromechanical Systems Engineering*. Norwood, MA: Artech House, 2000, pg. 17.

[102] T. Tsuchiya, A. Inoue, and J. Sakata, "Tensile testing of insulating thin films: humidity effect on tensile strength of SiO2 films," *Sensors and Actuators A*, vol. 82, May 2000, pp. 286-290.

[103] "SU-8 2-25 Product Information Sheet," MicroChem Corporation, Newton, MA, Feb. 2002, [Online]. Available: http://www.microchem.com/products/pdf/SU8_2-25.pdf

[104] S.-K. Kim, J.-Y. Yoo, and H.-K. Oh, "Resist distribution effect of spin coating," *Journal of Vacuum Science & Technology B: Microelectronics and Nanometer Structures*, vol. 20, no. 6, Nov. 2002, pp. 2206-2209.

[105] P. M. Dentinger, "Removal of SU-8 photoresist for thick film applications I: wet techniques," Sandia National Laborotories, Livermore, CA, [Online]. Available: http://www.microchem.com/resources/SU-8_Removal_by_Molten_Salts.pdf

[106] S. Clark, "The removal of organics using sulfuric peroxide," Bold Technologies, West Jordan, Utah, 2000, [Online]. Available: http://www.bold-tech.com/noframes/technical/piranha_etch.html

[107] "Nano-Strip Product Datasheet," Cyantek Corporation, Fremont, CA, [Online]. Available: http://www.rockemat.com/upc/product%20list.pdf

[108] M. C. Wu, "Micromachining for optical and optoelectronic systems," *Proceedings of the IEEE*, vol. 85, no. 7, Jul. 1997, pp. 1833-1856.

[109] F. T. O'Neill and J. T. Sheridan, "Photoresist reflow method of microlens production Part I: Background and experiments," *Optik*, vol. 113, no. 9, Nov. 2002, pp. 391-404.

[110] Y. Yi, S. Akiyama, P. Bermel, X. Duan, and L. C. Kimerling, "On-chip Si-based Bragg cladding waveguide with high index contrast bilayers," *Optics Express*, vol. 12, no. 20, Oct. 2004, pp. 4775-4780.

[111] R. Weinberger, *Practical Capillary Electrophoresis*, San Diego, CA: Academic Press, 1993, pp. 1-23.

[112] H. A. Reed, C. E. White, V. Rao, S. A. B. Allen, C.L. Henderson, and P. A. Kohl, "Fabrication of microchannels using polycarbonates as sacrificial materials," *Journal of Micromechanics and Microengineering*, vol. 11, no. 6, Nov. 2001, pp. 733-738.

[113] J. P. Jayachandran, H. A. Reed, H. Zhen, L. F. Rhodes, C. L. Henderson, S. A. B. Allen, and P. A. Kohl, "Air-channel fabrication for microelectromechanical systems via sacrificial photosensitive polycarbonates," *Journal of Microelectromechanical Systems*, vol. 12, no. 2, Apr. 2003, pp. 147-159.

[114] "Integrated Microfabrication Lab Web Page," Brigham Young University, Department of Electrical and Computer Engineering, Provo, UT, [Online]. Available: http://www.ece.byu.edu/cleanroom